GENERALIZED SPATIAL HOMOGENIZATION METHOD IN TRANSPORT THEORY AND HIGH ORDER DIFFUSION THEORY ENERGY RECONDENSATION METHODS

A Dissertation
Presented to
The Academic Faculty

by

Saam Yasseri

In Partial Fulfillment
of the Requirements for the Degree
Doctor of Philosophy in Nuclear and Radiological Engineering

George W. Woodruff School of Mechanical Engineering
Georgia Institute of Technology
May 2013

GENERALIZED SPATIAL HOMOGENIZATION METHOD IN TRANSPORT THEORY AND HIGH ORDER DIFFUSION THEORY ENERGY RECONDENSATION METHODS

Approved by:

Dr. Farzad Rahnema, Advisor
George W. Woodruff School
Georgia Institute of Technology

Dr. Alireza Haghighat
Department of Mechanical Engineering
Virginia Polytechnic Institute and State University

Dr. Bojan Petrovic
George W. Woodruff School
Georgia Institute of Technology

Dr. Glenn E. Sjoden
George W. Woodruff School
Georgia Institute of Technology

Dr. Dingkang Zhang
George W. Woodruff School
Georgia Institute of Technology

Dr. Tom Morley
School of Mathematics
Georgia Institute of Technology

Date Approved: March 25, 2013

ACKNOWLEDGEMENTS

This work was supported under a Rickover Graduate Fellowship Program sponsored initially by the Naval Reactors Divisions of the US Department of Energy for one year, and a NEUP Award Number DE-AC07-O5ID14517 for the rest of the time. Any opinions, findings, conclusions, or recommendations expressed in this publication are those of the author and do not necessarily reflect the views of the Department of Energy Office of Nuclear Energy.

I would like to extend my sincere gratitude to my advisor, Dr. Farzad Rahnema, for his guidance, patience and support throughout my education at Georgia Tech. I have learned volumes from his expertise in reactor physics and transport theory. His meticulousness and passion enhanced my desire to work enthusiastically.

I would like to thank Dr. Bojan Petrovic from whom I learned so much in various fields of Nuclear Engineering and his willingness to serve on my committee, Dr. Glenn E. Sjoden and Dr. Tom Morley for agreeing to read and critique my work, Dr. Dingkang Zhang for his invaluable help in computational transport theory, and Dr. Alireza Haghighat whom I had the pleasure of meeting a couple of times and willingness to serve on my committee.

I am unable to adequately express my appreciation to my parents, Farnoosh and Cyrus Yasseri, whose support and encouragement have been limitless and their continuous blessing and approval motivated me to work harder.

Lastly, my special thanks to Kevin Connolly and Steven Douglass for their help and advice, Andrew Holcomb, Daniel Lago, Ryan Hon and Alex Huning for unforgettable memories in the Computational Reactor and Medical Physics Laboratory and conference-related trips.

TABLE OF CONTENTS

LIST OF TABLES

LIST OF FIGURES

LIST OF SYMBOLS AND ABBREVIATIONS

BWR	Boiling Water Reactor
GCR	Gas Cooled Reactor
HTTR	High Temperature Test Reactor
CGEC	Consistent Generalized Energy Condensation
SGD	Subgroup Decomposition
ARO	All-Rods-Out
SRI	Some-Rods-In
ARI	All-Rods-In
CS	Core Sweeping
AFC	Assembly level Fixed-source Calculations
TSGD	Transport theory Subgroup Decomposition
MLOQD	Multi-group Low Order Quasi Diffusion
GLOQD	Grey Low Order Quasi Diffusion
NDA	Nodal Diffusion Acceleration
HSGD	Hybrid Subgroup Decomposition
NCT	Normalized Computation Time
CSH	Consistent Spatial Homogenization
RMS	Root Mean Square
FMTHIM	Fine-Mesh Transport Homogenization using Infinite Medium Approx.
ANOD	Accurate Nodal Diffusion homogenization
GET	Generalized Equivalence Theory

SUMMARY

In this dissertation, three different methods for solving the linear Boltzmann neutron transport equation (and its low-order approximations) are developed in general geometry and implemented in 1D slab geometry.

The first method is for solving the fine-group diffusion equation by estimating the in-scattering and fission source terms with consistent coarse-group diffusion solutions iteratively. This is achieved by extending the subgroup decomposition method initially developed in neutron transport theory to diffusion theory. Additionally, a new stabilizing scheme for on-the-fly cross-section re-condensation based on local fixed-source calculations is developed in the subgroup decomposition framework. The method is derived in general geometry and tested in 1D benchmark problems characteristic of Boiling Water Reactors (BWR) and Gas Cooled Reactor (GCR). It is shown that the method reproduces the standard fine-group results with 3-4 times faster computational speed in the BWR test problem and 1.5 to 6 times faster computational speed in the GCR core.

The second method is a hybrid diffusion-transport method for accelerating multi-group eigenvalue transport problems. This method extends the subgroup decomposition method to efficiently couple a coarse-group high-order diffusion method with a set of fixed-source transport decomposition sweeps to obtain the fine-group transport solution. The advantages of this new high-order diffusion theory are its consistent transport closure, straight forward implementation and numerical stability. The method is analyzed for 1D

BWR and High Temperature Test Reactor (HTTR) benchmark problems. It is shown that the method reproduces the fine-group transport solution with high accuracy while increasing the computationally efficiency up to 16 times in the BWR core and up to 3.3 times in the HTTR core compared to direct fine-group transport calculations.

The third method is a new spatial homogenization method in transport theory that reproduces the heterogeneous solution by using conventional flux weighted homogenized cross sections. By introducing an additional source term via an "auxiliary cross-section" the resulting homogeneous transport equation becomes consistent with the heterogeneous equation, enabling easy implementation into existing solution methods/codes. This new method utilizes on-the-fly re-homogenization, performed at the assembly level, to correct for core environment effects on the homogenized cross sections. The method is derived in general geometry and continuous energy, and implemented and tested in fine-group 1D slab geometries typical of BWR and GCR cores. The test problems include two single assembly and 4 core configurations.

It is believed that the coupling of the two new methods, namely the hybrid method for treating the energy variable and the new spatial homogenization method in transport theory set the stage, as future work, for the development of a robust and practical method for highly efficient and accurate whole core transport calculations.

INTRODUCTION

Neutron behavior in a nuclear system is governed by the linear Boltzmann equation. The steady state distribution of neutrons is a function of six variable phase space (space, energy and angle). For reactor core design and analysis, the accurate solution of the neutron distribution is required, and is typically determined using numerical methods. The complexity of the problem can be intractable even with modern computers and hence various approximations are applied to simplify the phase space. These approximations are utilized for each of the phase space elements independently. For the space variable, homogenization of the heterogeneous lattice cell is commonly used to reduce the complexity of the problem. For the energy treatment, the multi-group approximation is most commonly applied in which the energy variable is discretized leading to cross sections within an energy group. Widely used angular approximations are S_N, P_N, SP_N and diffusion theory.

Recent developments in nuclear core design have led to highly heterogeneous systems in which standard methods are incapable of predicting neutron behavior accurately. Standard energy condensation and spatial homogenization methods have been shown to introduce large errors for such systems requiring further improvements. The main source of error in both of these methods is due to the core environment effect. Spatial homogenization and energy condensation at the lattice cell (assembly level) are performed using approximate boundary conditions which do not represent the core environment accurately. Hence, the flux spectrum used for energy condensation and

spatial homogenization collapsing does not account for the effect of the adjacent lattices (assemblies). In this dissertation, a consistent spatial homogenization method that corrects for the core environment effect is developed. Additionally, a previously developed energy condensation method that consistently includes the core environment effect is accelerated using a new high-order diffusion theory.

This dissertation is divided into 3 chapters. Chapters 2 and 3 extend the subgroup decomposition method to efficiently solve eigenvalue diffusion problems (Chapter 2) and eigenvalue transport problems (Chapter 3). Chapter 4 introduces a new method for spatial homogenization in transport theory which, unlike most homogenization methods, can reproduce the heterogeneous solution using standard flux weighted cross sections.

SUBGROUP DECOMPOSITION IN DIFFUSION THEORY

2.1 Introduction

Energy treatment of the Boltzmann equation is an ongoing area of research in computational reactor physics. The goal of this research is to develop methods capable of condensing cross sections (from continuous energy to ultra-fine groups, ultra-fine groups to fine-group and more importantly fine-group to coarse-group) without sacrificing accuracy in solution (flux and eigenvalue). The conventional cross-section condensation method preserves the reaction rates and the new cross-section library is generated by flux weighting the original cross-section library (with or without an additional weighting function). This condensation method suffers from two major errors; lack of correction for core environment and energy-angle coupling effects. The former error is caused by condensing the cross sections with an approximate spectrum. This flux spectrum is generally obtained by assembly calculations with approximate (e.g., specular reflective) boundary conditions. The latter error is a result of assuming the angular flux is separable in energy and angle.

Recent developments such as the consistent generalized energy condensation (CGEC) method addressed the environmental and energy-angle coupling issues within the transport theory framework (Douglass and Rahnema, 2012a). In this method, fine-group flux at the core level is generated during the coarse-group calculation by preserving the detailed flux shape in the condensation process with a series of orthogonal expansion

moments. The resulting fine-group flux is a good approximation of the fine-group flux in the core, and has been shown to be valid with both continuous and discrete energy expansion functions (Douglass and Rahnema, 2011; Zhu and Forget, 2011). In order to improve issues associated with orthogonal expansion functions such as truncation error and computation time for generating expansion moments, the subgroup decomposition (SGD) method was subsequently introduced (Douglass and Rahnema, 2012b). The SGD method is comprised of iteratively solving a coarse-group transport equation and performing a set of fine-group transport decomposition sweeps to converge on the fine-group flux in the core.

In this chapter, the subgroup decomposition method which has been developed and tested in pure transport theory is extended to diffusion theory. The goal of this study is to develop a fast iterative method based on coarse-group diffusion with comparable accuracy to fine-group diffusion and highlight differences with traditional group collapsing in diffusion theory. Additionally, a different stabilizing scheme in the SGD framework is introduced in which embedded assembly level fixed-source diffusion calculations are carried out. The method is derived in its general form in section 2.2. In section 2.3, numerical results for a 1D Boiling Water Reactor (BWR) and a 1D High Temperature Test Reactor (HTTR) core are presented. Concluding remarks and future work are discussed in section 2.4.

2.2 Method

Consider an eigenvalue fine-group diffusion equation with G number of energy bins $\{g \mid g=1, 2, 3,..., G\}$ as shown in Eq. (2.1):

$$\begin{aligned} &\nabla.J^g(\vec{r}) + \sigma_{re}^g(\vec{r})\phi^g(\vec{r}) \\ &= \sum_{g'=1}^{G} \sigma_{s,re}^{g'\to g}(\vec{r})\phi^{g'}(\vec{r}) + \frac{\chi^g}{k}\sum_{g'=1}^{G} \nu\sigma_f^{g'}(\vec{r})\phi^{g'}(\vec{r}) \\ &J^g(\vec{r}) = -D^g(\vec{r})\nabla\phi^g(\vec{r}) = -\frac{1}{3\sigma_{tr}^g(\vec{r})}\nabla\phi^g(\vec{r}) \end{aligned} \tag{2.1}$$

where the fission term is assumed isotropic with removal and transport cross sections defined as:

$$\sigma_{re}^g = \sigma^g - \sigma_s^{g\to g} \tag{2.2}$$

$$\sigma_{s,re}^{g'\to g} = \begin{cases} \sigma_s^{g'\to g} & if\ g' \neq g \\ 0 & if\ g' = g \end{cases} \tag{2.3}$$

and

$$\sigma_{tr}^g = \sigma^g - \sigma_{s1}^g = \sigma_a^g + (1-\bar{\mu}^g)\sigma_s^g \tag{2.4}$$

where $\bar{\mu}^g$ is defined as the ratio of σ_{s1}^g to σ_s^g, *i.e.*, $\bar{\mu}^g = \sigma_{s1}^g/\sigma_s^g$.

It should be noted the principle of detailed balance, i.e., Eq. (2.5), has been implicitly applied to Eq. (2.1) which is a common approximation for multi-group diffusion equation.

$$\sum_{g'=1}^{G} \sigma_{s1}^{g' \to g} J^{g'} \cong \sum_{g'=1}^{G} \sigma_{s1}^{g \to g'} J^{g} = \sigma_{s1}^{g} J^{g} \tag{2.5}$$

Let C be the number of coarse groups where any fine-group *h* is fully contained in coarse-group *c.* In accordance with the reference work (Douglass and Rahnema, 2012b), the fine-group *h* is referred to as a "subgroup" of a coarse-group in which it is contained. The coarse-group diffusion/P_1 equation is defined by starting from the fine-group transport equation, integrating/summing over the energy range contained in coarse-group *c* and taking the 0^{th} and 1^{st} angular moment of the coarse-group transport equation assuming coarse-group flux is linearly anisotropic.

To be consistent with the fine-group diffusion equation in Eq. (2.1), the cross sections (total and scattering) in fine-group transport equation are transport corrected and fission term is assumed isotropic. The resulting transport equation is shown in Eq. (2.6).

$$\begin{aligned}
&\hat{\Omega}.\nabla\psi^h(\vec{r},\hat{\Omega}) + \sigma_{tr}^h(\vec{r})\psi^h(\vec{r},\hat{\Omega}) \\
&= \sum_{h'=1}^{G} \int_{4\pi} d\hat{\Omega}' \frac{\tilde{\sigma}_s^{h'\to h}(\vec{r})}{4\pi}\psi^{h'}(\vec{r},\hat{\Omega}') \\
&+ \frac{\chi^h}{4\pi k}\sum_{h'=1}^{G} \nu\sigma_f^{h'}(\vec{r})\phi^{h'}(\vec{r})
\end{aligned} \tag{2.6}$$

where transport corrected cross sections are defined in Eqs. (2.7) and (2.8).

$$\sigma_{tr}^h = \sigma^h - \sigma_{s1}^h = \sigma_a^h + (1-\bar{\mu}^h)\sigma_s^h \tag{2.7}$$

$$\tilde{\sigma}_s^{h'\to h} = \begin{cases} \sigma_s^{h'\to h} & if\ h' \neq h \\ \sigma_s^{h'\to h} - \sigma_{s1}^h = \sigma_s^{h'\to h} - \bar{\mu}^h\sigma_s^h & if\ h' = h \end{cases} \tag{2.8}$$

The coarse-group transport equation is obtained by summing over the fine groups within group *c* as shown below.

$$\begin{aligned}
&\hat{\Omega}.\nabla\psi^c(\vec{r},\hat{\Omega}) + \sigma_{tr}^c(\vec{r})\psi^c(\vec{r},\hat{\Omega}) \\
&= \sum_{c'=1}^{C} \int_{4\pi} d\hat{\Omega}' \frac{\tilde{\sigma}_s^{c'\to c}(\vec{r})}{4\pi}\psi^{c'}(\vec{r},\hat{\Omega}') \\
&+ \frac{\chi^c}{4\pi k^c}\sum_{c'=1}^{C} \nu\sigma_f^{c'}(\vec{r})\phi^{c'}(\vec{r}) + \delta^c(\vec{r},\hat{\Omega})\phi^c(\vec{r})
\end{aligned} \tag{2.9}$$

where the coarse-group coefficients are defined in the following equations.

$$\psi^c(\vec{r},\hat{\Omega}) = \sum_{h\in c} \psi^h(\vec{r},\hat{\Omega}) \tag{2.10}$$

$$\sigma_{tr}^c(\vec{r}) = \frac{\sum_{h\in c} \sigma_{tr}^h(\vec{r})\phi^h(\vec{r})}{\sum_{h\in c} \phi^h(\vec{r})} \tag{2.11}$$

$$\tilde{\sigma}_s^{c'\to c}(\vec{r}) = \frac{\sum_{h\in c}\sum_{h'\in c'} \tilde{\sigma}_s^{h'\to h}(\vec{r})\phi^{h'}(\vec{r})}{\sum_{h'\in c'} \phi^{h'}(\vec{r})} \tag{2.12}$$

$$\chi^c = \sum_{h\in c} \chi^h \tag{2.13}$$

$$\nu\sigma_f^{c'}(\vec{r}) = \frac{\sum_{h'\in c'} \nu\sigma_f{}^{h'}(\vec{r})\phi^{h'}(\vec{r})}{\sum_{h'\in c'} \phi^{h'}(\vec{r})} \tag{2.14}$$

and

$$\delta^c(\vec{r},\hat{\Omega}) = \frac{\sum_{h\in c}[\sigma_{tr}^c(\vec{r}) - \sigma_{tr}^h(\vec{r})]\psi^h(\vec{r},\hat{\Omega})}{\sum_{h\in c} \phi^h(\vec{r})} \tag{2.15}$$

The 0th and 1st angular moments of Eq. (2.9) are derived by assuming linearly anisotropic coarse-group flux as shown in Eq. (2.16).

$$\begin{aligned} &\nabla . J^c(\vec{r}) + \sigma_{tr}^c(\vec{r})\phi^c(\vec{r}) \\ &= \sum_{c'=1}^{C} \tilde{\sigma}_s^{c'\to c}(\vec{r})\phi^{c'}(\vec{r}) + \frac{\chi^c}{k^c}\sum_{c'=1}^{C} \nu\sigma_f^{c'}(\vec{r})\phi^{c'}(\vec{r}) \\ &+ \int_{4\pi} d\hat{\Omega}\, \delta^c\left(\vec{r},\hat{\Omega}\right)\phi^c(\vec{r}) \\ &\frac{1}{3}\nabla\phi^c(\vec{r}) + \sigma_{tr}^c(\vec{r})J^c(\vec{r}) = \int_{4\pi} d\hat{\Omega}\,\hat{\Omega}\delta^c\left(\vec{r},\hat{\Omega}\right)\phi^c(\vec{r}) \end{aligned} \tag{2.16}$$

Using Eq. (2.15), the coarse group P_1 equation is simplified to:

$$\begin{aligned} &\nabla . J^c(\vec{r}) + \sigma_{tr}^c(\vec{r})\phi^c(\vec{r}) \\ &= \sum_{c'=1}^{C} \tilde{\sigma}_s^{c'\to c}(\vec{r})\phi^{c'}(\vec{r}) + \frac{\chi^c}{k^c}\sum_{c'=1}^{C} \nu\sigma_f^{c'}(\vec{r})\phi^{c'}(\vec{r}) \\ &\frac{1}{3}\nabla\phi^c(\vec{r}) + \sigma_{tr}^c(\vec{r})J^c(\vec{r}) = \delta_1^c(\vec{r})\phi^c(\vec{r}) \end{aligned} \tag{2.17}$$

where δ_1^c is defined as:

$$\delta_1^c(\vec{r}) = \frac{\sum_{h\in c}[\sigma_{tr}^c(\vec{r}) - \sigma_{tr}^h(\vec{r})]J^h(\vec{r})}{\sum_{h\in c}\phi^h(\vec{r})} \tag{2.18}$$

δ_1^c is a "perturbation cross-section" that is required to maintain the consistency of the coarse-group P_1 equations with fine-group diffusion and it is commonly omitted from coarse-group diffusion calculation. It is worth noting that one might consider further simplifying Eq. (2.17) to remove the in-group scattering cross-section from the total cross-section. However, for coarse-group calculations using standard power iteration scheme this might result in numerical instabilities and/or longer convergence time. Thus for this chapter, Eq. (2.17) is used for coarse-group P_1 calculations in which transport corrected cross sections are used instead of the conventional cross sections.

In order to unfold the fine-group flux from the coarse-group solution, a "decomposition sweep" is required. In this process, fine-group diffusion is solved where the source term for any subgroup *h* is modified to take into account the newly calculated coarse-group flux. To this extent, the reaction rates (scattering and fission) in any subgroup *h* are represented through "subgroup decomposition cross sections" multiplied by respective coarse-group fluxes. The subgroup decomposition cross sections are calculated in the same manner as those found in Eqs. (2.10)- (2.15). Hence, the fine-group diffusion decomposition sweep is defined as:

$$-\nabla . D^h(\vec{r})\nabla\phi^h(\vec{r}) + \sigma_{re}^h(\vec{r})\phi^h(\vec{r}) = \sum_{c'=1}^{C} \sigma_{s,re}^{c'\to h}(\vec{r})\phi^{c'}(\vec{r}) + \frac{1}{k^c}\sum_{c'=1}^{C} \chi^h \nu\sigma_f^{c'}(\vec{r})\phi^{c'}(\vec{r}) \tag{2.19}$$

where the subgroup decomposition cross sections are:

$$\sigma_{s,re}^{c'\to h}(\vec{r}) = \frac{\sum_{h'\in c'} \sigma_{s,re}^{h'\to h}(\vec{r})\phi^{h'}(\vec{r})}{\sum_{h'\in c'} \phi^{h'}(\vec{r})} \tag{2.20}$$

$$\chi^{h}\nu\sigma_{f}^{c'}(\vec{r}) = \frac{\chi^{h}\sum_{h'\in c'} \nu\sigma_{f}{}^{h'}(\vec{r})\phi^{h'}(\vec{r})}{\sum_{h'\in c'} \phi^{h'}(\vec{r})} \tag{2.21}$$

The decomposition sweep is computationally cheap since its cross sections are already computed from the flux guess and the coarse-group flux and eigenvalue are calculated by solving Eq. (2.17). Therefore, no source iteration is involved and all terms on the RHS of Eq. (2.19) are known quantities.

As explained, the cross sections in Eqs. (2.17) are dependent on the initial fine-group flux. If the fine-group flux guess is the solution to the fine-group diffusion equation, the coarse-group flux is consistent with the fine-group solution and only one decomposition sweep is required to unfold the detailed flux spectrum. However, this is not the case in practice and a re-condensation procedure is necessary to incorporate the correct core environment in the initial spectrum obtained by assembly calculations with approximate boundary conditions. The re-condensation procedure is comprised of solving Eqs. (2.17) and (2.19) iteratively and using the solution of Eq. (2.19) as a new subgroup flux guess. Nonetheless, this scheme would be unstable for most problems and would not lead to a converged solution. Therefore, an additional step is added to stabilize the re-condensation procedure. Two "stabilizing schemes" are presented in this chapter and their performance and accuracy are demonstrated in section 2.3.

The first stabilizing scheme, core sweeping, is similar to that developed in Douglass and Rahnema, 2012b. During core sweeping, a single diffusion sweep for each subgroup is carried out where the multi-group flux with subscript "*p*" is the solution to Eq. (2.19) and k^c is the coarse-group eigenvalue from Eq. (2.17). The updated flux is denoted with subscript "*p+1/2*". The subscript refers to the number of times the coarse-group diffusion is solved and the flux update is performed to correct for the core environment. Therefore, subscript *p+1/2* refers to an intermediate step between *p* and *p+1* where the stabilization is performed to ensure convergence.

$$\begin{aligned} &-\nabla . D^h(\vec{r})\nabla\phi^h_{p+1/2}(\vec{r}) + \sigma^h_{re}(\vec{r})\phi^h_{p+1/2}(\vec{r}) \\ &= \sum_{h'=1}^{G} \sigma^{h'\to h}_{s,re}(\vec{r})\phi^{h'}_p(\vec{r}) + \frac{\chi^h}{k^c}\sum_{h'=1}^{G} \nu\sigma^{h'}_f(\vec{r})\phi^{h'}_p(\vec{r}) \end{aligned} \tag{2.22}$$

The second stabilizing scheme is an embedded assembly level fixe- source diffusion calculation. During this scheme, a fixed-source problem at the assembly level is solved using the coarse-group eigenvalue from Eq. (2.17) and incoming currents calculated from the solution of Eq. (2.19) at the interface of the assemblies.

$$\begin{aligned} &-\nabla . D^h(\vec{r})\nabla\phi^h_{p+1/2}(\vec{r}) + \sigma^h_{re}(\vec{r})\phi^h_{p+1/2}(\vec{r}) \\ &= \sum_{h'=1}^{G} \sigma^{h'\to h}_{s,re}(\vec{r})\phi^{h'}_{p+1/2}(\vec{r}) \\ &+ \frac{\chi^h}{k^c}\sum_{h'=1}^{G} \nu\sigma^{h'}_f(\vec{r})\phi^{h'}_{p+1/2}(\vec{r}) \end{aligned} \tag{2.23}$$

The boundary condition for the fixed-source diffusion problem is defined in Eq. (2.24).

$$\begin{aligned}\vec{J}(\vec{r}_s)^h_{inc,p} &= \hat{n}_s . \int_{2\pi^-} d\hat{\Omega}\, \hat{\Omega} \psi^h_{p+1/2}(\vec{r}_s, \hat{\Omega}) \\ &= \hat{n}_s . \int_{2\pi^-} d\hat{\Omega}\, \hat{\Omega} \left\{ \frac{1}{4\pi} \phi(\vec{r}_s)^h_{p+\frac{1}{2}} + \frac{3}{4\pi} \hat{\Omega} . \vec{J}(\vec{r}_s)^h_{p+\frac{1}{2}} \right\} \\ &= \frac{1}{4} \phi(\vec{r}_s)^h_{p+\frac{1}{2}} + \frac{D^h(\vec{r})}{2} \hat{n}_s . \nabla \phi(\vec{r}_s)^h_{p+\frac{1}{2}}\end{aligned} \tag{2.24}$$

Regardless of the stabilizing scheme performed, the updated flux is used as a fine-group flux guess for the next iteration. In summary, the re-condensation scheme is described as below.

1. Perform fine-group assembly calculations with approximate boundary conditions to generate the initial flux spectrum and apply this spectrum to Eqs. (2.11)-(2.14), (2.18), (2.20) and (2.21) to generate coarse-group and decomposition cross sections.
2. Solve the coarse-group whole-core diffusion equation using the cross sections generated in step (1).
3. Perform a diffusion decomposition sweep for each subgroup using the decomposition cross sections generated in step (1) with the coarse-group eigenvalue and scalar flux in step (2).
4. Perform the stabilizing scheme (i.e., core sweeping or assembly level fixed-source calculations) using the subgroup flux obtained from step (3). The updated fine-

group flux spectrum is used to update the coarse-group and decomposition cross sections.

5. Repeat steps (2) - (4) until the user defined successive iteration criteria for coarse-group flux and eigenvalue of Eqs. (2.25) and (2.26) are met where the subscript "p" is the iteration number.

$$\left|\frac{\phi_{p+1}^{c}(\vec{r})-\phi_{p}^{c}(\vec{r})}{\phi_{p+1}^{c}(\vec{r})}\right|_{max}<(\varepsilon_{\phi})_{re-cond} \tag{2.25}$$

and

$$\left|\frac{k_{p+1}^{c}-k_{p}^{c}}{k_{p+1}^{c}}\right|_{max}<(\varepsilon_{k})_{re-cond} \tag{2.26}$$

A flowchart of the SGD method in diffusion theory is presented in Figure 2.1 to demonstrate the re-condensation procedure.

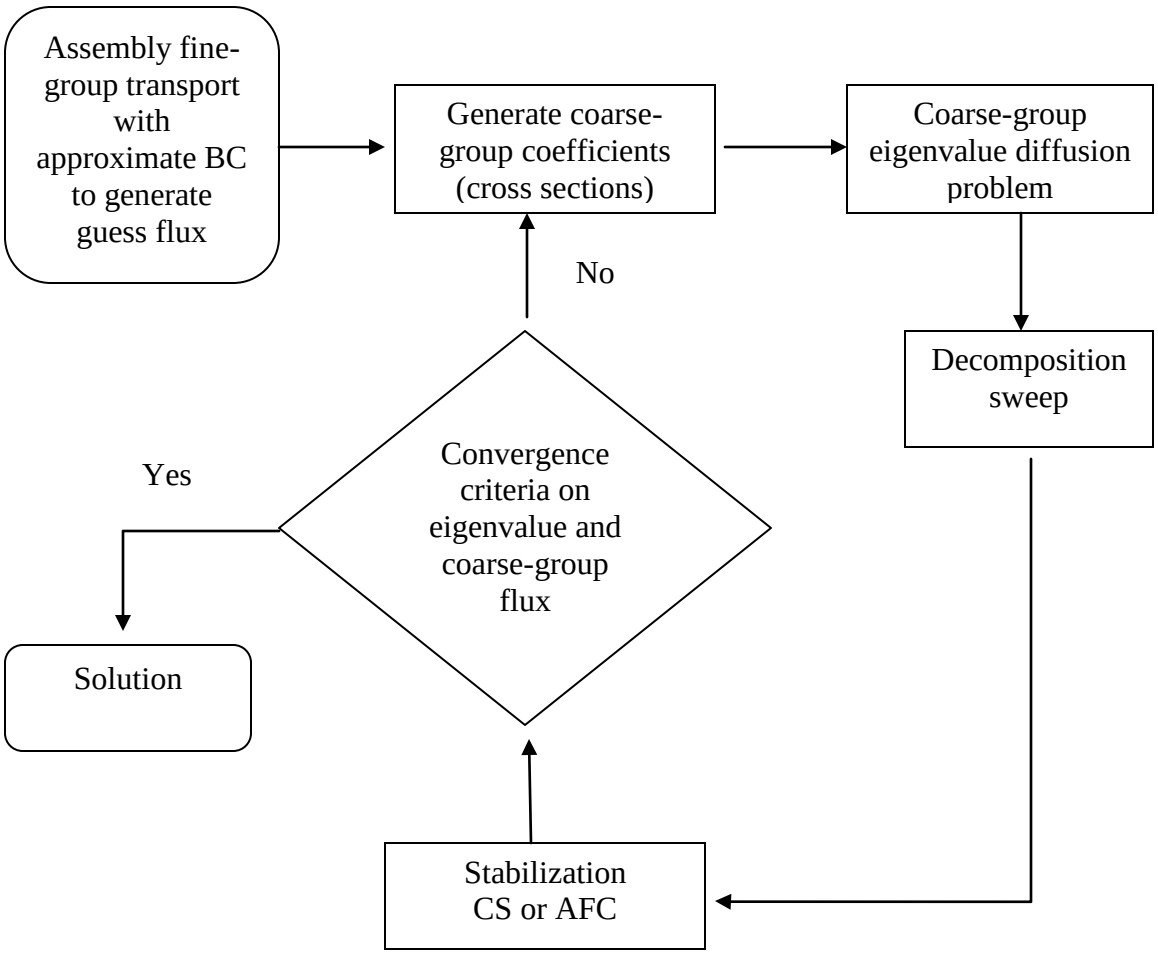

Figure 2.1. Flowchart of SGD re-condensation in diffusion theory

2.3 Numerical Results

In this section, the method is benchmarked for a 1D BWR core (Douglass and Rahnema, 2010a) and a 1D HTTR core (Douglass and Rahnema, 2010c). The reference solution is obtained by solving a 47-group diffusion problem with the flux and eigenvalue convergence criteria of 10^{-5} and 10^{-8} , respectively. In the re-condensation method, a 2-group diffusion problem is solved iteratively with the coarse-group flux and eigenvalue convergence criteria set to 10^{-6} and 10^{-9} while the successive iteration criteria were

chosen as $(\varepsilon_{\phi})_{re-cond} = 10^{-3}$ and $(\varepsilon_{k})_{re-cond} = 10^{-4}$. As discussed previously in section 2.2, the re-condensation method is demonstrated for two different stabilizing schemes, i.e., core sweeping and assembly level fixed-source calculations. Furthermore, a standard 2-group/6-group diffusion solution with cross sections obtained from 47-group single assembly calculations with specular reflection is also included for comparison. The flux spectrum for blocks with non-fissionable material is assumed to be the same as the boundary flux spectrum of the adjacent block with fissionable material. The spatial discretization is kept same for all problems with a resolution of half mean free path in every mesh.

For the numerical results, the average, mean relative and maximum errors are defined as:

$$AVG^{c} = \frac{\int dx|e^{c}(x)|}{\int dx} \tag{2.27}$$

$$MRE^{c} = \frac{\int dx|e^{c}(x)|\phi^{c}_{re-cond}(x)}{\int dx\phi^{c}_{ref}(x)} \tag{2.28}$$

$$MAX^{c} = \max(|e^{c}(x)|) \tag{2.29}$$

where

$$e^c(x) = 100\% \frac{\phi^c_{ref}(x) - \phi^c_{re-cond}(x)}{\phi^c_{ref}(x)} \tag{2.30}$$

and

$$\phi^c_{ref} = \sum_{g \in c} \phi^g_{ref} \tag{2.31}$$

2.3.1 1D BWR Core

A GE9 BWR lattice (Kelly, 1995) was chosen as representative of BWR assemblies, which consists of 12 fuel types, including four pins that possess 5.84 at% Gd. It was modeled in half symmetry with full heterogeneity and a 47-group calculation was performed to deplete the assembly to 17 GWD/THM for three void parameters (0%, 40% and 70%). The lattice depletion code HELIOS (Simeonov, 2003) was used to perform transport calculations for 2D fuel assembly problem and generate 1D region-wise cross-section by performing a flux-weighted transverse integration of the cross sections over slab regions of the 2D model. The 1D core is composed of 20 assemblies of width 15.24 cm, modeled with half symmetry for two control configurations: All-Rods-out (ARO) and Some-Rods-in (SRI). Assemblies labeled "A" are fresh and the ones labeled "B" are depleted to 17 GWD/THM and the "+" refers to controlled assemblies. The benchmark is specified at operating temperature, wherein all non-fuel materials are evaluated at a temperature of 600 K, and fuel materials are evaluated at a temperature of 833 K. Each

assembly is composed of 11 macroscopic cross-section regions, laid out as in Figure 2.2(a).

Wide gap	Bundle Casing	Fuel 1	Fuel 2	Fuel 3	Fuel 4	Fuel 5	Fuel 6	Fuel 7	Bundle Casing	Narrow gap
0.9525	0.40386	1.6256	1.6256	1.6256	3.2512	1.6256	1.6256	1.6256	0.40386	0.47498

(a)

70% A	70% B	40% A	40% B	0% A	0% B	0% A	0% B	0% A	0% MOD

(b)

70% A+	70% B	40% A	40% B+	0% A+	0% B+	0% A+	0% B	0% A	0% MOD

(c)

Figure 2.2. 1D Assembly layout (a), 1D BWR core layout for: ARO configuration (b), SRI configuration (c)

The cores were modeled with specular and vacuum boundary conditions on the left and right sides, respectively. The outer assembly labeled “MOD” is a uniform moderator comprised of un-voided moderator with cross sections from the fresh assembly. The commonly used 2-group structure for BWRs (Douglass and Rahnema, 2010b) with thermal ($E<0.625\ eV$) and fast range ($E>0.625\ eV$) is used for condensation and presentation.

Fast and thermal flux errors in addition to eigenvalue errors for ARO configuration are presented in Table 2.1. The eigenvalue of standard 2-group diffusion has an error of 600 pcm. The flux error is a result of the approximate flux spectrum obtained from assembly calculations and neglecting the coarse-group perturbation cross-section. However, the SGD re-condensation is capable of accounting for both core environment and energy-angle coupling effects. Both stabilizing schemes in the SGD method show negligible error compared to standard coarse-group diffusion and their relative flux errors are plotted in Figure 2.3. Small discontinuities are seen at the interface of the assemblies for AFC stabilizing scheme. This is due to the nature of the scheme that assembly calculations are performed independently based on the incoming currents evaluated from the decomposition sweep and flux continuity is not forced at the interfaces.

Table 2.1. Eigenvalue and flux error in ARO configuration for standard 2-group and 2-group SGD re-condensation

	$k_{47g-ref}$=1.065746		AVG(%)		MAX(%)		MRE(%)	
	k_{2g}	Δk^a (pcm)	Fast	Thermal	Fast	Thermal	Fast	Thermal
2g Std	1.071794	-604.8	6.77	7.61	30.88	25.67	5.98	6.67
2g SGD- CS[b]	1.065745	0.1	0.09	0.10	0.25	0.21	0.07	0.08
2g SGD- AFC[c]	1.065749	-0.3	0.09	0.11	0.19	0.27	0.07	0.09

[a] $\Delta k = (k_{47g-ref} - k_{2g}) \times 10^5$
[b] Core Sweeping
[c] Assembly level Fixed-source Calculations

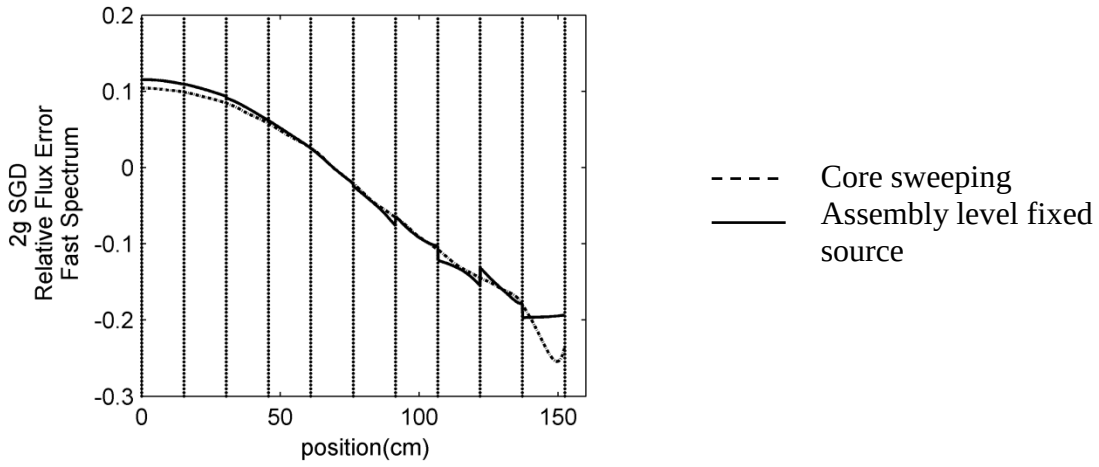

(a) Relative flux error in fast spectrum for CS and AFC

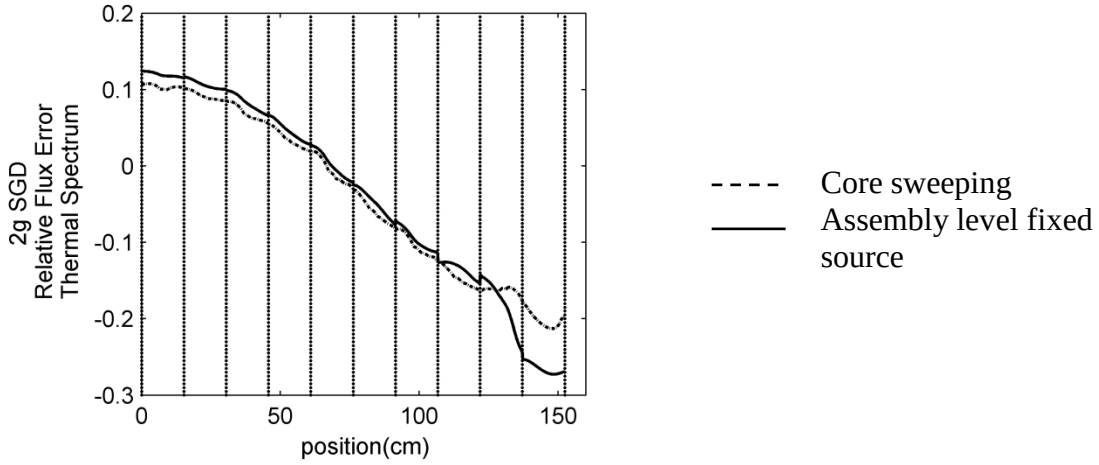

(b) Relative flux error in thermal spectrum for CS and AFC

Figure 2.3. Relative flux error 2- group spectrum (in percent) in ARO configuration of 1D BWR core

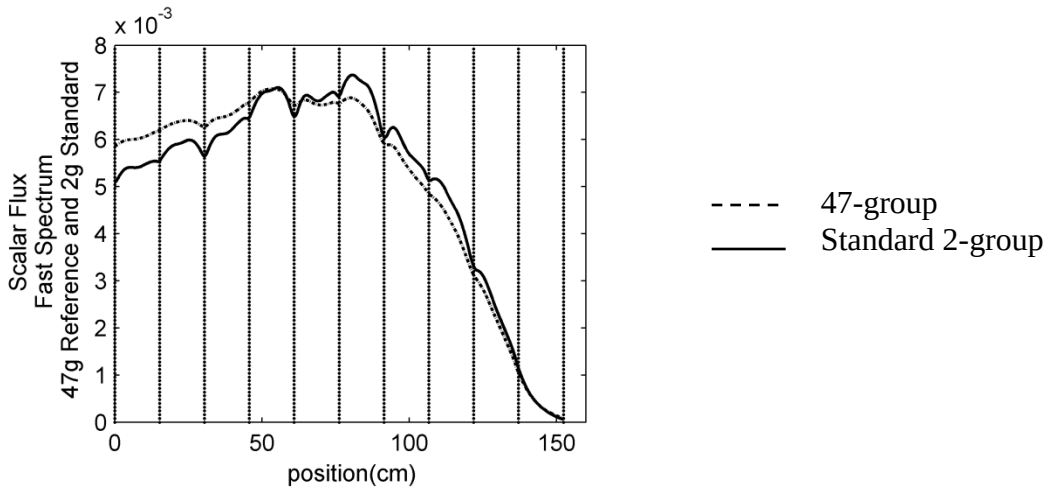

(a) Fast spectrum

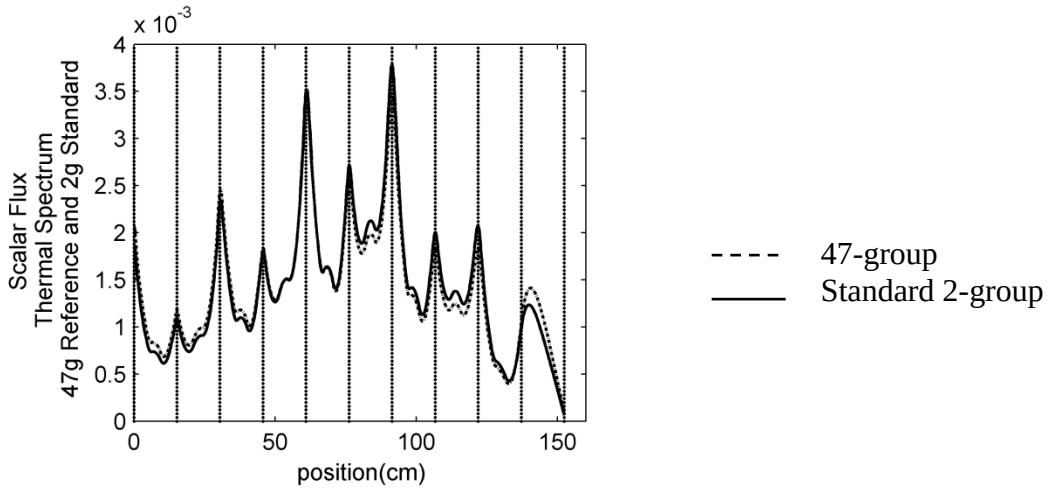

(b) Thermal spectrum

Figure 2.4. Flux spectrum for 47-group (reference) and standard 2-group solution in ARO configuration

Figure 2.4 demonstrates the 47-group reference solution and the standard 2-group solution. The maximum error is seen close to the vacuum boundary where the initial flux spectrum based on approximate boundary conditions is less accurate and the energy-angle coupling effect is dominant.

Table 2.2. Eigenvalue and flux error in SRI configuration for standard 2-group and 2-group SGD re-condensation

	$k_{47g-ref}$=1.001783		AVG(%)		MAX(%)		MRE(%)	
	k_{2g}	$\Delta k\ (pcm)$	Fast	Thermal	Fast	Thermal	Fast	Thermal
2g Std	1.007194	-541.1	15.43	14.61	37.05	34.25	14.62	16.23
2g SGD- CS	1.001785	-0.2	0.19	0.20	0.39	0.39	0.16	0.19
2g SGD- AFC	1.001791	-0.8	0.17	0.19	0.33	0.41	0.15	0.18

It is noted from Tables 2.1 and 2.2 that the standard 2-group exhibits higher flux error for the SRI configuration compared to ARO. The core environment effect is more prominent in the controlled case and the cross sections condensed from approximate assembly boundary conditions result in higher flux error. Similar to ARO configuration, both stabilizing schemes in SGD re-condensation method improve the accuracy significantly by two orders of magnitude. Figure 2.5 demonstrates the relative flux errors for fast and thermal spectra while the reference and standard 2-group flux are compared in Figure 2.6. The maximum error for standard 2-group condensation is seen close to the vacuum boundary where the flux behaves anisotropically (i.e., linearly anisotropic in the diffusion limit) and therefore the perturbation cross-section in the coarse group P_1 equations has a significant impact.

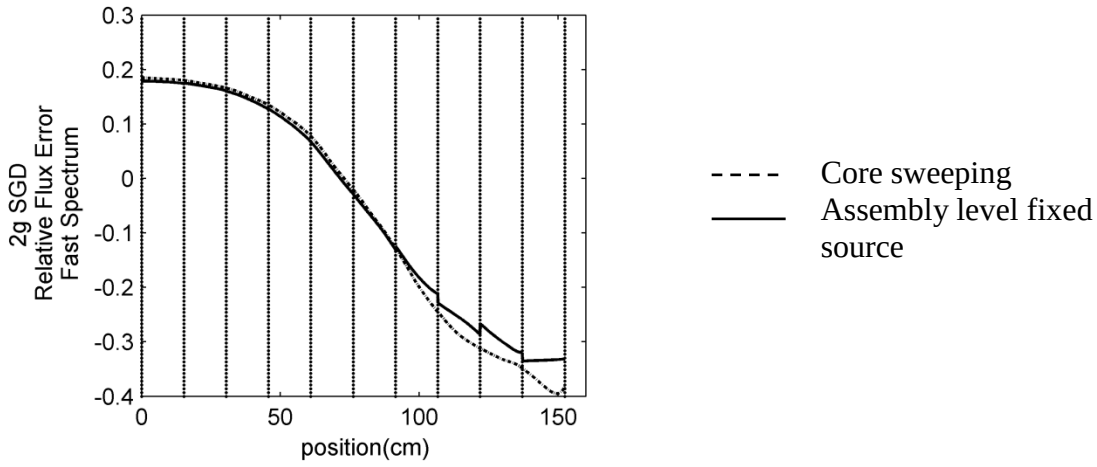

(a) Relative flux error in fast spectrum for CS and AFC

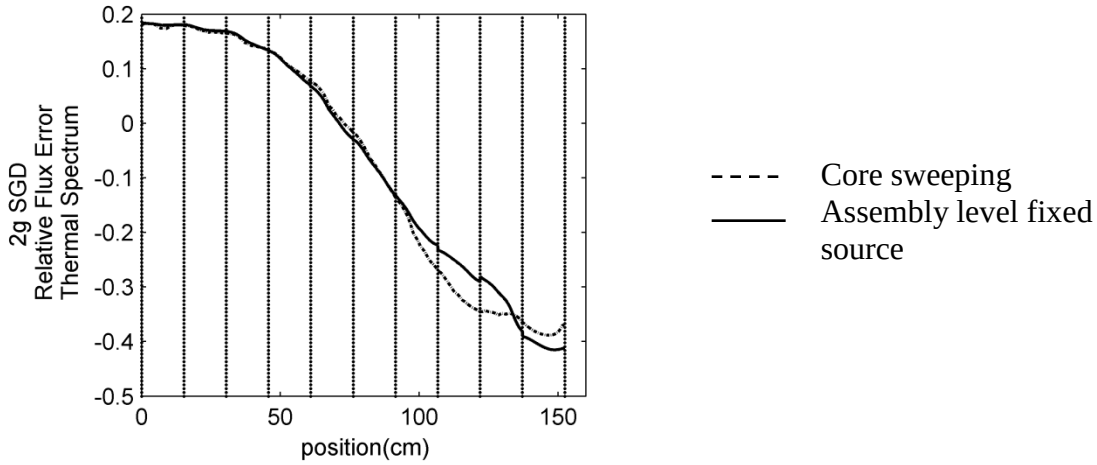

(b) Relative flux error in thermal spectrum for CS and AFC

Figure 2.5. Relative flux error 2- group spectrum (in percent) in SRI configuration of 1D BWR core

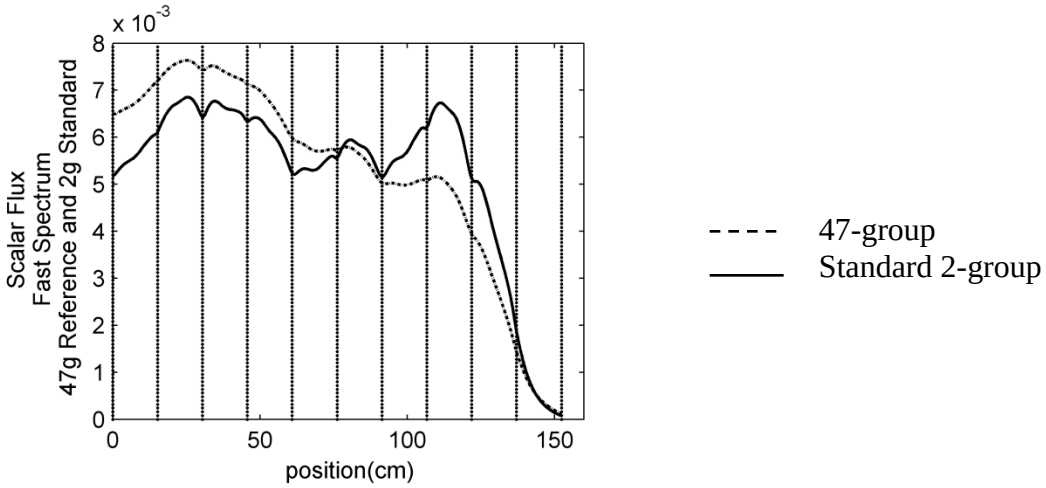

(a) Fast spectrum

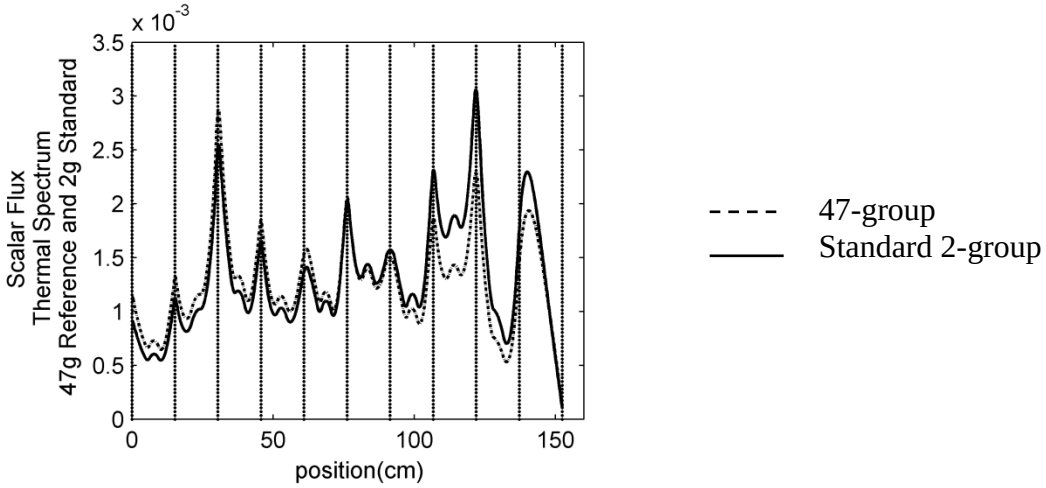

(b) Thermal spectrum

Figure 2.6. Flux spectrum for 47-group (reference) and standard 2-group solution in SRI configuration

Table 2.3. Computation time comparison of 1D BWR core for 47-group and 2-group SGD re-condensation

1D BWR		*NCT*[a]	*c-iteration*	*s-iteration*	*l-iteration*
ARO	*47g- Reference*	1	1214	-	-
	2g SGD- CS	0.260	16	16	-
	2g SGD- AFC	0.261	7	-	533
SRI	*47g- Reference*	1	1751	-	-
	2g SGD- CS	0.306	16	16	-
	2g SGD- AFC	0.269	8	-	707

[a] Normalized Computation Time

Table 2.3 compares the computation times for two configurations of the BWR core utilizing two stabilizing schemes in SGD re-condensation. All computation times are normalized to the reference 47-group computation time to emphasize the method and demonstrate the efficiency of the proposed re-condensation method. The *c*-iteration in SGD method refers to the number of iterations the coarse-group cross sections is updated. The *s*-iteration for CS is the same as *c*-iteration because after every decomposition sweep, a core sweeping is carried out to update the flux. However, different mechanics are involved in AFC. During each *c*-iteration, different assemblies require different number of iterations in order to converge on the fixed-source problem. The *l*-iteration shown in Table 2.3 for the AFC stabilizing scheme is the maximum cumulative local iterations per assembly to ensure convergence of the fixed-source problem during the re-condensation. For the uncontrolled case, stabilizing schemes have similar performance with the computation time being 1/4 of the reference time. On the other hand, the AFC stabilizing scheme has a slightly superior performance over CS for the controlled case. The majority of the computation time in SGD re-condensation is consumed by coarse-group

calculations and flux update (decomposition sweep and stabilizing scheme) is relatively quick.

2.3.2 1D HTTR Core

The selected 1D benchmark problem is characteristic of gas cooled prismatic block reactor systems. The 2D 47- group cross sections were generated by performing three different calculations in HELIOS (Simeonov, 2003) for 1/6 fuel block, 1/6 control block with half fuel block and 1/6 reflector block with half fuel block (Zhang et al., 2011). The 1D geometry was obtained by preserving the volume of different materials and the number densities were generated by performing volume-weighted homogenization over the hexagonal rings of the 2D HTTR core. The detailed parameters and the method of development of the benchmark problem are found in (Douglass and Rahnema, 2010c), The core consists of eight blocks of 4 types: Fuel 1, Fuel 2, Fuel 3, Control Rod Block (CRB), and Reflectors, laid out as in Figure 2.7, with specular reflective boundary conditions on the left, vacuum boundary conditions on the right. Two configurations are considered for this dissertation: All-Rods-Out (ARO) and All-Rods-In (ARI). The center control rods are only used for core loading and are disassembled after the startup. Hence, the ARI configuration includes presence of control rods in Fuel Block 2 and in the Outer Control assembly. Note the heterogeneity in the fuel and control block are not shown in Figure 2.7. Each fuel block consists of 6 fuel pins, a center graphite region, and outer graphite regions. Each control-rod block consists of 2 control rods, surrounded by tube regions, with center and outer graphite slabs. In the ARO configuration, the tube material

(graphite + helium gas) fills the control regions. For the ARI configuration, the number densities of the control blocks have been smeared into the graphite of fuel 2.

The 2-group boundaries used for SGD method correspond to appropriate boundaries in the 6-group structure commonly used in VHTR analysis (Zhang et al., 2011).

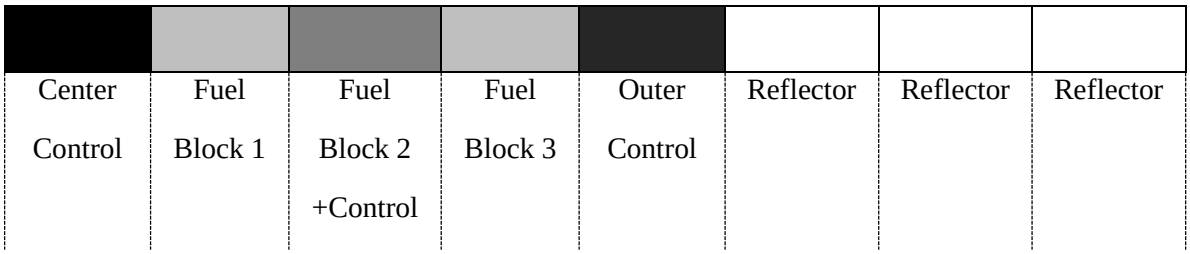

Figure 2.7. 1D HTTR core layout – The cross sections are different for fuel block 2 and outer control in ARO and ARI configurations.

The results from the 2-group methods and the 6-group standard methods are compared to the reference 47-group results in Table 2.4. The 2-group SGD methods differ only in the stabilizing scheme and aside from the fast spectrum maximum error, their results are very similar. The error in the standard 6-group increases within the reflector region due to the large error in the initial flux spectrum utilized for cross-section condensation. In addition, the effect of energy-angle coupling captured by the perturbation cross-section in the SGD method is ignored in the standard coarse-group calculations and it is more pronounced in the fast spectrum.

Table 2.4. Eigenvalue and flux error in ARO configuration for standard 6-group and 2-group SGD re-condensation

	$k_{47g-ref}$=1.101010		AVG(%)		MAX(%)		MRE(%)	
	$k_{6g/2g}$	Δk^a (pcm)	Fast	Thermal	Fast	Thermal	Fast	Thermal
6g Std	1.116887	-1587.7	450.54	4.44	3308.6	13.25	2.30	3.16
2g SGD- CS	1.100947	6.3	0.01	0.02	1.63	0.07	0.01	0.01
2g SGD- AFC	1.100994	1.6	0.01	0.02	0.03	0.08	0.01	0.01

[a] $\Delta k = (k_{47g-ref} - k_{6g/2g}) \times 10^5$

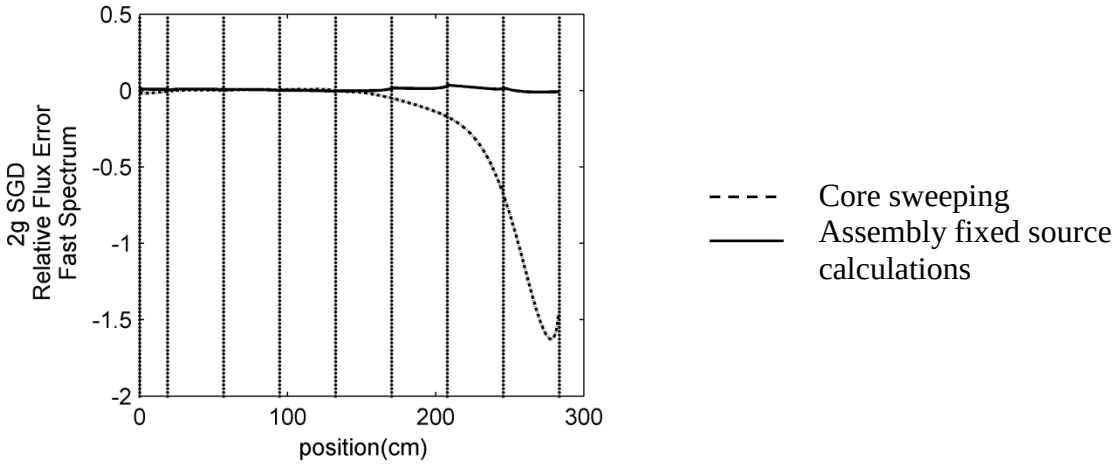

(a) Relative flux error in fast spectrum for CS and AFC

Figure 2.8. Relative flux error 2- group spectrum (in percent) in ARO configuration of 1D HTTR core

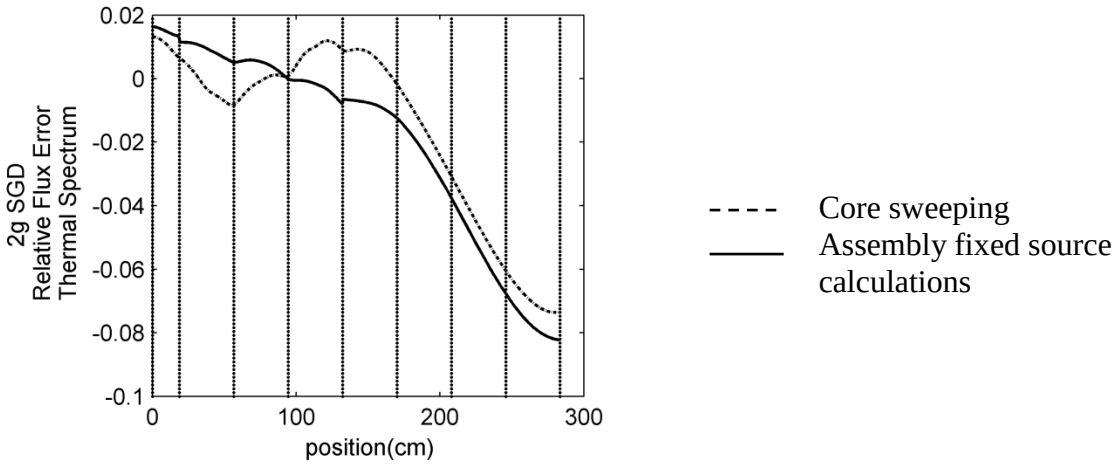

(b) Relative flux error in thermal spectrum for CS and AFC

Figure 2.8 continued

Figure 2.8 demonstrates the relative flux error for the SGD method using two stabilizing schemes; CS and AFC. The AFC scheme shows a slightly better performance in the fast spectrum in which independent assembly calculations are carried out based on fixed incoming currents. Hence, the continuity of the flux at the assembly interface is not forced and as a result small discontinuities can be observed.

In Figure 2.9, the fast and thermal fluxes for the reference solution along with the standard 6-group is plotted. As predicted, the fast spectrum flux peaks in the fuel blocks in the ARO configuration where the control rods are not present and local flux depressions are noticeable in the thermal spectrum at points where the fuel pins are located.

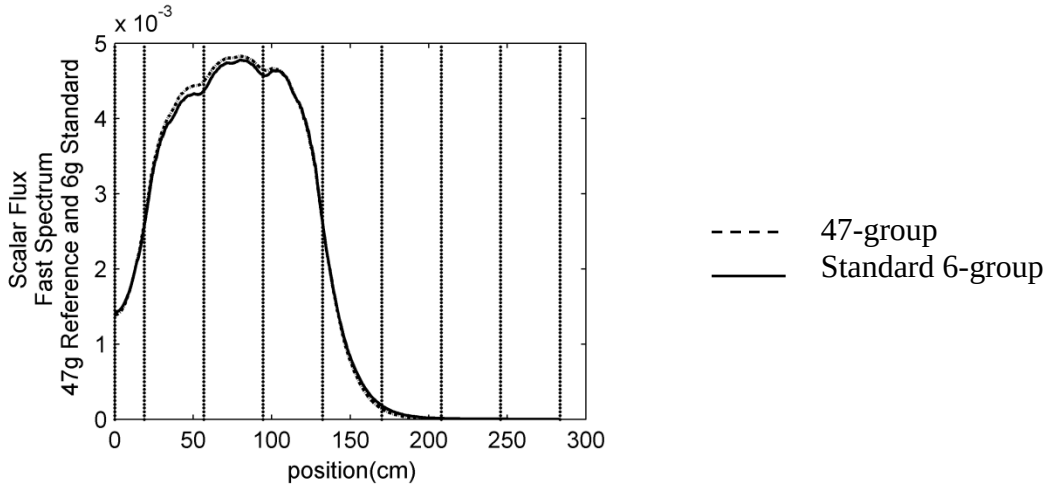

(a) Fast spectrum

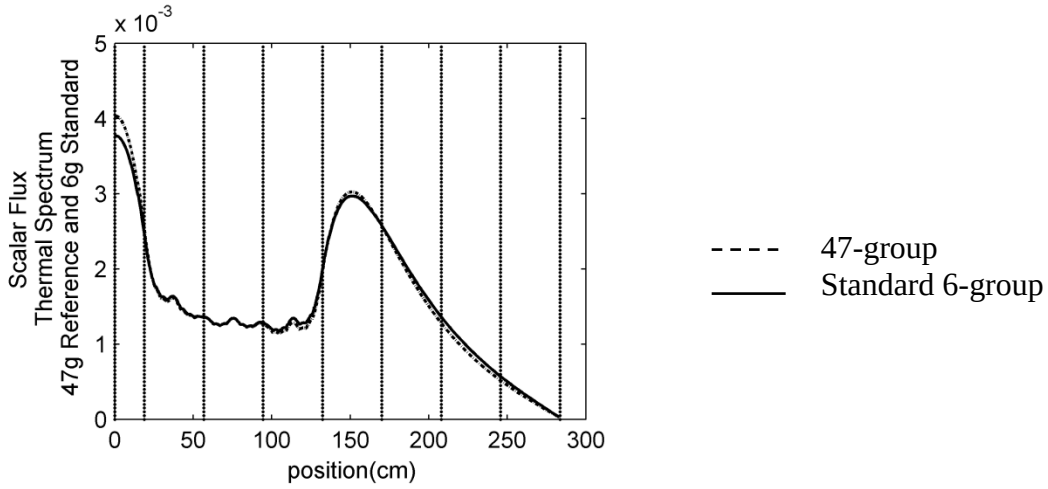

(b) Thermal spectrum

Figure 2.9. Flux spectrum for 47-group (reference) and standard 6-group solution in ARO configuration

Similarly, the relative flux errors and eigenvalue errors for ARI configuration are presented in Table 2.5. Due to presence of control rods in this configuration, higher errors are noticed for the standard 6-group in thermal flux and hence the eigenvalue of the standard coarse-group is off by 1700 pcm. On the other hand, lower error is seen in the fast flux which is a result of smaller energy-angle coupling effect in ARI configuration.

Table 2.5. Eigenvalue and flux error in ARI configuration for standard 6-group and 2-group SGD re-condensation

	$k_{47g-ref}$=0.828501		AVG(%)		MAX(%)		MRE(%)	
	$k_{6g/2g}$	Δk (pcm)	Fast	Thermal	Fast	Thermal	Fast	Thermal
6g Std	0.845540	-1703.9	31.48	8.74	178.30	21.83	1.76	3.67
2g SGD- CS	0.828371	13	0.10	0.09	0.46	0.31	0.01	0.05
2g SGD- AFC	0.828495	0.6	0.01	0.06	0.03	0.26	0.01	0.01

Figure 2.10 demonstrates the relative flux errors for both SGD methods and the standard coarse-group. Both SGD methods decrease the flux error by at least two orders of magnitude through consistent correction of the core environment effect. The reference fast and thermal fluxes are plotted in Figure 2.11.

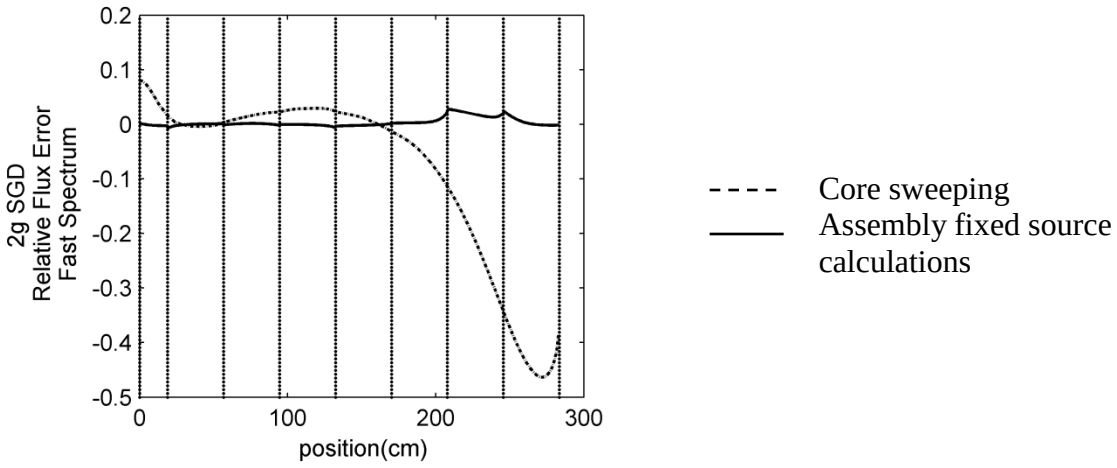

(a) Relative flux error in fast spectrum for CS and AFC

Figure 2.10. Relative flux error 2- group spectrum (in percent) in ARI configuration of 1D HTTR core

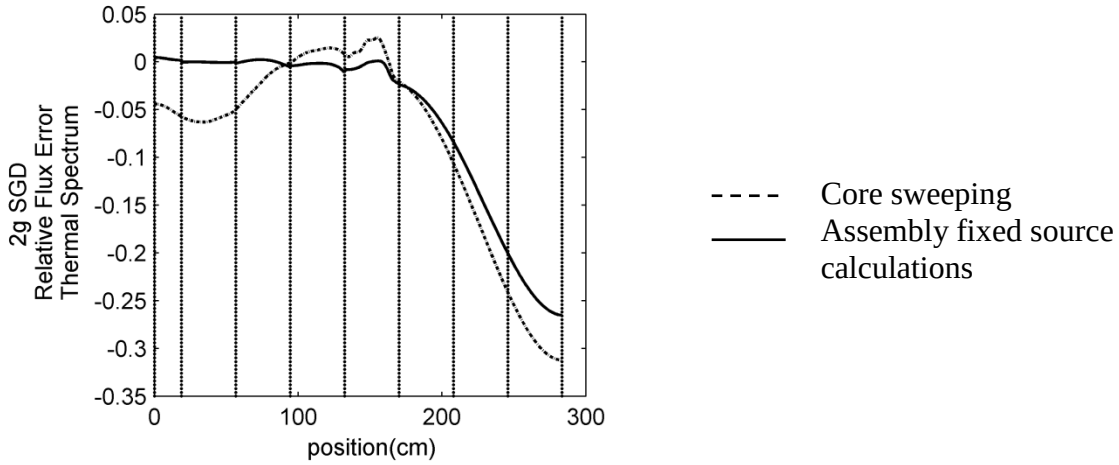

(b) Relative flux error in thermal spectrum for CS and AFC

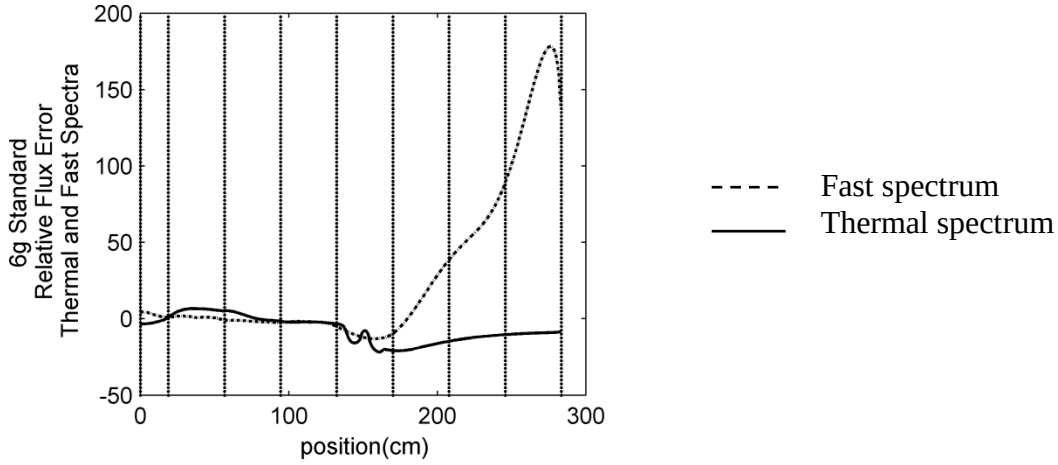

(c) Relative flux error in fast and thermal spectra for standard 6g

Figure 2.10 continued

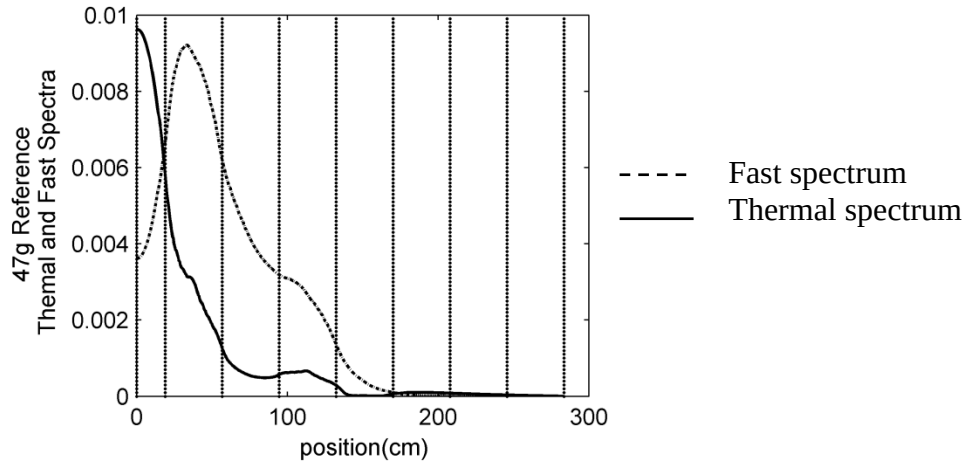

Figure 2.11. 47-group (reference) fast and thermal flux spectra

Table 2.6 compares the computation times for SGD method using CS and AFC stabilizing schemes. The computation times are normalized to the reference (47-group) computation time. The *c*-iteration refers to the number of iterations the coarse-group cross sections is updated. The *s*-iteration for CS scheme is the same as *c*-iteration since after every decomposition sweep an additional core sweeping is performed. However, the *l*-iteration for AFC scheme refers to maximum cumulative local iterations per assembly to ensure convergence of the fixed-source problem during the re-condensation. It is seen that the AFC scheme has a superior performance compared to CS while achieving improved accuracy. Hence, AFC is chosen to be a preferred stabilizing scheme in SGD framework for reactors with harder spectra.

Table 2.6. Computation time comparison of 1D HTTR core for 47-group and 2-group SGD re-condensation

1D HTTR		*NCT*	*c-iteration*	*s-iteration*	*l-iteration*
ARO	*47g- Reference*	1	3787	-	-
	2g SGD- CS	0.618	77	77	-
	2g SGD- AFC	0.151	14	-	907
ARI	*47g- Reference*	1	3294	-	-
	2g SGD- CS	0.524	73	73	-
	2g SGD- AFC	0.124	14	-	948

2.4 Concluding Remarks

In this chapter, the subgroup decomposition transport method has been extended to diffusion theory. This method improves the computational efficiency of fine-group whole-core diffusion solution by estimating the in-scattering and fission source terms with consistent coarse-group diffusion solutions iteratively. The coarse-group to fine-group iteration is stabilized by two different methods, one of which is new and the other is similar to that introduced initially in the transport theory framework.

This method can be also viewed as a significant improvement in accuracy of the coarse-group methods used by the industry to perform routine whole-core analyses. The gain in accuracy is achieved by removing the effect of core environment on the energy collapsed cross sections at the expense of computational efficiency, nevertheless, more efficient (by a factor of 4 for BWR and a factor of 6 for the HTTR) than fine-group whole-core calculation as seen in the benchmark problems.

In the 1D GCR core, it is noted that the standard 6-group calculation has significant errors in both the core eigenvalue and the local solution (e.g., flux and fission density) because the standard method, which uses single lattice cross sections without energy angle correction, does not account for the effect of core environment. It is therefore concluded that the subgroup decomposition method is an excellent candidate as an efficient and highly accurate tool for neutronic analysis of gas cooled reactors (e.g., VHTR) in which non-fuel block are dominant.

In this chapter the method's accuracy and numerical stability has been verified for a BWR and HTTR benchmark problems in 1D slab geometry. The results show that the assembly level fixed-source calculation is computationally more efficient than the core sweeping stabilizing scheme for the HTTR problem. This is mainly due to neutron's longer mean free path in GCRs which decreases the convergence time for fixed-source calculations and localizes the error to individual assemblies. However, the core sweeping stabilizing scheme was the preferred scheme for the BWR core.

The original subgroup decomposition method was developed in transport theory framework in which even coarse group transport calculations can be quite expensive in 3D configurations. It would be interesting to consider accelerating the fine-group whole-core transport calculations using coarse-group high-order diffusion theory. This is discussed in the following chapter.

2.5 References

Douglass, S., Rahnema, F., 2010a. Development of a 1-D boiling water reactor benchmark specification. Transactions of the American Nuclear Society, San Diego, CA, June 13-17, Vol. 102, 543–545.

Douglass, S., Rahnema, F., 2010b. Analysis of cross section condensation in PWR simulations. Transactions of the American Nuclear Society, Pittsburgh, PA, May 9–14.

Douglass, S., Rahnema, F., 2010c. Specification for a 1-dimensional gas-cooled reactor benchmark problem for neutron transport. Transactions of the American Nuclear Society, Hollywood, FL, May 9–14, Vol. 102, 74-78.

Douglass, S., Rahnema, F., 2011. Cross section recondensation method via generalized energy condensation theory. Annals of Nuclear Energy 38 (9), 2105–2110.

Douglass, S., Rahnema, F., 2012a. Consistent generalized energy condensation theory. Annals of Nuclear Energy 40 (1), 200–214.

Douglass, S., Rahnema, F., 2012b. Subgroup decomposition method. Annals of Nuclear Energy 48, 84–101.

Kelly, D. J., 1995. Depletion of a BWR lattice using the RACER continuous energy Monte Carlo code. In: Proceedings of the International Conference on Mathematics and Computations, Reactor Physics and Environmental Analyses, Portland, Oregon, April 30–May 4, Vol. 2, 1011.

Simeonov, T., 2003. Release Notes – Helios System Version 1.8. Studsvik Scandpower Report, SSP-03/221, November 26.

Yasseri, S., Rahnema, F., 2013. Subgroup Decomposition Method in Diffusion Theory. Annals of Nuclear Energy, Submitted (January).

Zhang, Z., Rahnema, F., Zhang, D., Pounders, J. M., Ougouag, A. M., 2011. Simplified two and three dimensional HTTR benchmark problems. Annals of Nuclear Energy 38, 1172-1185.

Zhu, L., Forget, B., 2011. An energy recondensation method using the discrete generalized multigroup energy expansion theory. Annals of Nuclear Energy 38 (8), 1718–1727.

A High-order Diffusion Theory Subgroup Decomposition Method for Accelerating Eigenvalue Transport Solutions

3.1 Introduction

Recently, Douglass and Rahnema (2012) developed a new Subgroup Decomposition method (SGD) for treating the energy variable in the linear Boltzmann equation. This method can be viewed as a consistent re-condensation scheme that efficiently solves the fine-group flux by iterating on the coarse-group calculation. The SGD method has been developed and implemented within transport theory (Douglass and Rahnema, 2012) and diffusion theory (Chapter 2), separately. The Transport theory SGD (TSGD) method utilizes coarse-group transport calculations and a set of transport decomposition sweeps to unfold the fine-group transport flux spectrum. The key feature of the SGD method is its ability to correct for spectral core environment effects which is an eminent source of error in re-condensation methods. Consistent multi-group formulations (*i.e.*, energy-angle coupling) and on-the-fly cross-section re-condensation at the core level are the reason for high accuracy of the SGD method independent of the coarse-group structure.

Anistratov and Gol'din (2011) have developed a multi-level method in 1D slab geometries for solving multi-group eigenvalue transport problems. In this work a combination of effective one-group low order quasi-diffusion equation and multi-group low order equation are utilized to accelerate the multi-group *k*-eigenvalue transport problems. In the multi-level approach, the Multi-group Low Order Quasi-Diffusion

(MLOQD) is used to accelerate the multi-group transport in the first layer and an effective Grey (one-group) Low Order Quasi-Diffusion (GLOQD) is utilized to accelerate the multi-group low order equation in the second layer by evaluating the eigenvalue and one-group flux. In a different work by Anistratov (2011), Nonlinear Diffusion Acceleration (NDA) method is presented as a fast iterative algorithm for solving multi-group eigenvalue transport problems. This work demonstrates that an effective one-group low order NDA consistent with eigenvalue transport problems accelerates the multi-group low order NDA equations.

The TSGD method can be viewed as an acceleration scheme for solving multi-group eigenvalue transport problems by using coarse-group transport calculation iteratively. Since decomposition sweep (a step in the SGD method that unfolds the flux spectrum from the coarse-group flux) depends on coarse-group flux and eigenvalue, coarse-group diffusion is an efficient candidate for replacing the coarse-group transport calculation. However, this would require development of a high-order diffusion theory which incorporates the angular details for the coarse-group calculation. In this chapter, the TSGD method is combined with a new high-order diffusion theory resulting in a Hybrid SGD (HSGD) method to increase computational efficiency while maintaining transport accuracy for the fine-group flux. We believe this method is simpler to implement than other hybrid high-order diffusion transport methods. This is because, as can be seen later, the high-order diffusion theory developed in section 2 can be easily implemented in existing diffusion codes by introducing only one additional term while retaining the standard (P_1) definition of diffusion coefficient.

The new HSGD method is derived in its general form in section 3.2. Its accuracy in a 1D BWR benchmark problem is investigated in section 3.3. Concluding remarks and future work are found in section 3.4.

3.2 Method

For an eigenvalue problem, the fine-group transport angular flux is governed by Eq. (3.1) in which G is the total number of fine groups $\{g \mid g=1, 2, 3, \ldots, G\}$.

$$\begin{aligned} &\hat{\Omega}.\nabla\psi^{g}\left(\vec{r},\hat{\Omega}\right)+\sigma^{g}(\vec{r})\psi^{g}\left(\vec{r},\hat{\Omega}\right) \\ &=\sum_{g'=1}^{G}\int_{4\pi}d\hat{\Omega}'\frac{1}{4\pi}\Big\{\sigma_{s0}^{g'\to g}(\vec{r}) \\ &+3\sigma_{s1}^{g'\to g}(\vec{r})\hat{\Omega}.\hat{\Omega}'\Big\}\psi^{g'}\left(\vec{r},\hat{\Omega}'\right) \\ &+\frac{\chi^{g}}{4\pi k}\sum_{g'=1}^{G}\nu\sigma_{f}^{g'}(\vec{r})\phi^{g'}(\vec{r}) \end{aligned} \tag{3.1}$$

Standard notation (Douglass and Rahnema, 2012) is used in Eq. (3.1). The fission and scattering kernels are assumed isotropic and linearly anisotropic, respectively. These assumptions are common in lattice depletion methods used in thermal reactor systems. It is noted that inclusion of higher scattering anisotropy will not be captured by the high-order diffusion method to be derived below.

Let C be the number of coarse groups where any fine-group *h* is fully contained in coarse-group *c*. By integrating/summing over the energy range contained in coarse-group *c*, the coarse-group transport equation is obtained as shown in Eq. (3.2).

$$\begin{aligned}
&\hat{\Omega}.\nabla\psi^c(\vec{r},\hat{\Omega}) + \sigma^c(\vec{r})\psi^c(\vec{r},\hat{\Omega}) \\
&= \sum_{c'=1}^{C} \frac{\sigma_{s0}^{c'\to c}(\vec{r})}{4\pi} \int_{4\pi} d\hat{\Omega}'\, \psi^{c'}(\vec{r},\hat{\Omega}') \\
&+ \hat{\Omega}.\left\{\sum_{c'=1}^{C} \frac{3}{4\pi}\sigma_{s1}^{c'\to c}(\vec{r}) \int_{4\pi} d\hat{\Omega}'\, \hat{\Omega}'\psi^{c'}(\vec{r},\hat{\Omega}')\right\} \\
&+ \frac{\chi^c}{4\pi k^c}\sum_{c'=1}^{C} \nu\sigma_f^{c'}(\vec{r})\phi^{c'}(\vec{r}) \\
&+ \left\{\delta_1^c(\vec{r},\hat{\Omega}) + \delta_2^c(\vec{r},\hat{\Omega})\right\}\phi^c(\vec{r})
\end{aligned} \tag{3.2}$$

where the coarse-group coefficients are defined in the following equations.

$$\psi^c(\vec{r},\hat{\Omega}) = \sum_{h\in c}\psi^h(\vec{r},\hat{\Omega}) \tag{3.3}$$

$$\sigma^c(\vec{r}) = \frac{\sum_{h\in c}\sigma^h(\vec{r})\phi^h(\vec{r})}{\sum_{h\in c}\phi^h(\vec{r})} \tag{3.4}$$

$$\sigma_{s0}^{c'\to c}(\vec{r}) = \frac{\sum_{h\in c}\sum_{h'\in c'}\sigma_{s0}^{h'\to h}\phi^{h'}(\vec{r})}{\sum_{h'\in c'}\phi^{h'}(\vec{r})} \tag{3.5}$$

$$\sigma_{s1}^{c'\to c}(\vec{r}) = \frac{\sum_{h\in c}\sum_{h'\in c'}\sigma_{s1}^{h'\to h}(\vec{r})\phi^{h'}(\vec{r})}{\sum_{h'\in c'}\phi^{h'}(\vec{r})} \tag{3.6}$$

$$\chi^{c} = \sum_{h\in c}\chi^{h} \tag{3.7}$$

$$\nu\sigma_{f}^{c'}(\vec{r}) = \frac{\sum_{h'\in c'}\nu\sigma_{f}{}^{h'}(\vec{r})\phi^{h'}(\vec{r})}{\sum_{h'\in c'}\phi^{h'}(\vec{r})} \tag{3.8}$$

$$\delta_{1}^{c}(\vec{r},\hat{\Omega}) = \frac{\sum_{h\in c}[\sigma^{c}(\vec{r}) - \sigma^{h}(\vec{r})]\psi^{h}(\vec{r},\hat{\Omega})}{\sum_{h\in c}\phi^{h}(\vec{r})} \tag{3.9}$$

and

$$\delta_{2}^{c}(\vec{r},\hat{\Omega}) = \frac{3}{4\pi}\hat{\Omega}.\frac{\sum_{c'=1}^{C}\sum_{h'\in c'}[\sum_{h\in c}\sigma_{s1}^{h'\to h}(\vec{r}) - \sigma_{s1}^{c'\to c}(\vec{r})]J^{h'}(\vec{r})}{\sum_{h\in c}\phi^{h}(\vec{r})} \tag{3.10}$$

Taking the 0th and 1st angular moment of Eq. (3.2) will result in Eqs. (3.11) and (3.12).

$$\begin{aligned}&\nabla.J^{c}(\vec{r}) + \sigma^{c}(\vec{r})\phi^{c}(\vec{r})\\ &= \sum_{c'=1}^{C}\sigma_{s0}^{c'\to c}(\vec{r})\phi^{c'}(\vec{r}) + \frac{\chi^{c}}{k^{c}}\sum_{c'=1}^{C}\nu\sigma_{f}^{c'}(\vec{r})\phi^{c'}(\vec{r})\end{aligned} \tag{3.11}$$

$$\nabla.\overleftrightarrow{\Pi}^{c}(\vec{r})+\sigma_{tr}^{c}(\vec{r})J^{c}(\vec{r})=\left\{\vartheta_{2}^{c}(\vec{r})+\int_{4\pi}d\hat{\Omega}\,\hat{\Omega}\vartheta_{1}^{c}(\vec{r},\hat{\Omega})\right\}\phi^{c}(\vec{r}) \tag{3.12}$$

where

$$\overleftrightarrow{\Pi}^{c}(\vec{r})=\int_{4\pi}d\hat{\Omega}\,\hat{\Omega}\hat{\Omega}\psi^{c}(\vec{r},\hat{\Omega}) \tag{3.13}$$

$$\vartheta_{1}^{c}(\vec{r},\hat{\Omega})=\frac{\sum_{h\in c}[\sigma_{tr}^{c}(\vec{r})-\sigma_{tr}^{h}(\vec{r})]\psi^{h}(\vec{r},\hat{\Omega})}{\sum_{h\in c}\phi^{h}(\vec{r})} \tag{3.14}$$

and

$$\vartheta_{2}^{c}(\vec{r})=\frac{\sum_{c'=1}^{C}\sum_{h'\in c'}\sum_{h\in c}[\sigma_{s1}^{h'\to h}(\vec{r})J^{h'}(\vec{r})-\sigma_{s1}^{h\to h'}(\vec{r})J^{h}(\vec{r})]}{\sum_{h\in c}\phi^{h}(\vec{r})} \tag{3.15}$$

In the above equations, the vector symbol for current, gradient and current weighted cross sections has been omitted for simplicity. The double sided arrow (↔) is used as a symbol for tensor. For the ease of implementation, Eq. (3.12) is modified as below to resemble the standard coarse-group diffusion equation while maintaining higher order transport effects (beyond 1st order in angle).

$$\frac{1}{3}\nabla\phi^c(\vec{r}) + \sigma_{tr}^c(\vec{r})J^c(\vec{r})$$
$$= \left\{\vartheta_2^c(\vec{r}) + \int_{4\pi} d\hat{\Omega}\,\hat{\Omega}\vartheta_1^c(\vec{r},\hat{\Omega})\right\}\phi^c(\vec{r}) + \vartheta_3^c(\vec{r})\phi^c(\vec{r}) \tag{3.16}$$

where the new term is defined as:

$$\vartheta_3^c(\vec{r}) = \frac{\sum_{h\in c}[\frac{1}{3}\nabla\phi^h(\vec{r}) - \nabla.\vec{\vec{\Pi}}^h(\vec{r})]}{\sum_{h\in c}\phi^h(\vec{r})} \tag{3.17}$$

Combining Eqs. (3.11)- (3.17) yields the following coarse-group high-order diffusion equations.

$$\nabla.J^c(\vec{r}) + \sigma^c(\vec{r})\phi^c(\vec{r})$$
$$= \sum_{c'=1}^{C}\sigma_{s0}^{c'\to c}(\vec{r})\phi^{c'}(\vec{r}) + \frac{\chi^c}{k^c}\sum_{c'=1}^{C}\nu\sigma_f^{c'}(\vec{r})\phi^{c'}(\vec{r}) \tag{3.18}$$
$$\frac{1}{3}\nabla\phi^c(\vec{r}) + \sigma_{tr}^c(\vec{r})J^c(\vec{r}) = \Delta^c(\vec{r})\phi^c(\vec{r})$$

where

$$\Delta^c(\vec{r}) = \frac{\sum_{h\in c}[\sigma_{tr}^{c}(\vec{r}) - \sigma_{tr}^{h}(\vec{r})]J^h(\vec{r})}{\sum_{h\in c}\phi^h(\vec{r})}$$

$$+\frac{\sum_{c'=1}^{C}\sum_{h'\in c'}\sum_{h\in c}[\sigma_{s1}^{h'\to h}(\vec{r})J^{h'}(\vec{r}) - \sigma_{s1}^{h\to h'}(\vec{r})J^h(\vec{r})]}{\sum_{h\in c}\phi^h(\vec{r})} \tag{3.19}$$

$$+\frac{\sum_{h\in c}[\frac{1}{3}\nabla\phi^h(\vec{r}) - \nabla.\overleftrightarrow{\Pi}^h(\vec{r})]}{\sum_{h\in c}\phi^h(\vec{r})}$$

It is noted that the first term in the definition of Δ^c accounts for the effect of energy-angle coupling due the energy collapsing of the total/transport cross-section. The second term is a result of linearly anisotropic scattering kernel and the third term ensures that the coarse-group high-order diffusion equations capture the transport effects while maintaining numerical stability. The Δ^c term is indeed a coarse-group coefficient and depends on the flux spectrum used in the energy collapsing process.

For boundary condition, since the degree of anisotropy of the angular flux is not limited by any approximation, the generalized boundary condition originally developed in quasi-diffusion (Anistratov, 2005) is used.

$$J^c(\vec{r}_s).\hat{n}_s = \frac{1-\alpha_1^c}{1+\alpha_0^c} C_{r_s}^c \phi^c(\vec{r}_s)$$

$$\alpha_n^c = \frac{\sum_{h\in c}\int_{2\pi^-} |\hat{n}_s.\hat{\Omega}|^n \psi^h(\vec{r},\hat{\Omega}) d\hat{\Omega}}{\sum_{h\in c}\int_{2\pi^+} (\hat{n}_s.\hat{\Omega})^n \psi^h(\vec{r},\hat{\Omega}) d\hat{\Omega}} \tag{3.20}$$

$$C_{r_s}^c = \frac{\sum_{h\in c}\int_{2\pi^+} (\hat{n}_s.\hat{\Omega}) \psi^h(\vec{r},\hat{\Omega}) d\hat{\Omega}}{\sum_{h\in c}\int_{2\pi^+} \psi^h(\vec{r},\hat{\Omega}) d\hat{\Omega}}$$

In the SGD method, the fine-group flux spectrum corresponding to the newly calculated coarse-group flux is attained through "decomposition sweep". During a decomposition sweep, the fine-group transport equation is solved at the core level with a pre-defined source term (fission and scattering) using decomposition cross sections, coarse-group eigenvalue and scalar flux, as given below.

$$\begin{aligned} &\hat{\Omega}.\nabla\psi_{decomp\_swp}^h(\vec{r},\hat{\Omega}) + \sigma^h(\vec{r})\psi_{decom\_swp}^h(\vec{r},\hat{\Omega}) \\ &= \sum_{c'=1}^{C} \frac{1}{4\pi}\left\{R_{s0}^{c'\to h}(\vec{r}) + 3R_{s1}^{c'\to h}(\vec{r}).\hat{\Omega}\right\}\phi^{c'}(\vec{r}) \\ &+ \frac{1}{4\pi k^c}\sum_{c'=1}^{C} \chi^h \nu\sigma_f^{c'}(\vec{r})\phi^{c'}(\vec{r}) \end{aligned} \tag{3.21}$$

The decomposition cross sections in the above equation are defined as:

$$R_{s0}^{c'\to h}(\vec{r}) = \frac{\sum_{h'\in c'} \sigma_{s0}^{h'\to h}(\vec{r})\phi^{h'}(\vec{r})}{\sum_{h'\in c'} \phi^{h'}(\vec{r})} \tag{3.22}$$

$$R_{s1}^{c'\to h}(\vec{r}) = \frac{\sum_{h'\in c'} \sigma_{s1}^{h'\to h}(\vec{r}) J^{h'}(\vec{r})}{\sum_{h'\in c'} \phi^{h'}(\vec{r})} \tag{3.23}$$

and

$$\chi^{h} \nu\sigma_{f}^{c'}(\vec{r}) = \frac{\chi^{h} \sum_{h'\in c'} \nu\sigma_{f}{}^{h'}(\vec{r}) \phi^{h'}(\vec{r})}{\sum_{h'\in c'} \phi^{h'}(\vec{r})} \tag{3.24}$$

The SGD method iterates on the fine-group flux spectrum until convergence is obtained. As explained in Douglass and Rahnema (2012), to guarantee convergence, the method requires an additional step, hereon referred to as "a stabilizing scheme." Two stabilizing schemes, similar to those introduced in Chapter 2, are described below and evaluated for computational efficiency and accuracy in section 3.3.

The first scheme, referred to as core sweeping (CS), is a single transport sweep at the core level using the fine-group flux obtained from the decomposition sweep. This is shown in Eq. (3.25).

$$
\begin{aligned}
&\hat{\Omega}.\nabla\psi^{h}_{core\_swp}(\vec{r},\hat{\Omega})+\sigma^{h}(\vec{r})\psi^{h}_{core\_swp}(\vec{r},\hat{\Omega})\\
&=\sum_{h'=1}^{G}\int_{4\pi}d\hat{\Omega}'\frac{1}{4\pi}\{\sigma_{s0}^{h'\to h}(\vec{r})\\
&+3\sigma_{s1}^{h'\to h}(\vec{r})\hat{\Omega}.\hat{\Omega}'\}\psi^{h'}_{decom\_swp}(\vec{r},\hat{\Omega}')\\
&+\frac{\chi^{h}}{4\pi k^{c}}\sum_{h'=1}^{G}\nu\sigma_{f}^{h'}(\vec{r})\phi^{h'}_{decom\_swp}(\vec{r})
\end{aligned}
\tag{3.25}
$$

The second scheme, named "Assembly level Fixed-source Calculations" (AFC), as the name implies, are fixed-source transport calculations performed at the assembly level with the eigenvalue determined by the coarse-group high-order diffusion and incoming angular fluxes determined from the decomposition sweep, *i.e.*, Eq. (3.21). This is shown in Eq. (3.26).

$$
\begin{aligned}
&\hat{\Omega}.\nabla\psi^{h}_{assem\_fix}(\vec{r},\hat{\Omega})+\sigma^{h}(\vec{r})\psi^{h}_{assem\_fix}(\vec{r},\hat{\Omega})\\
&=\sum_{h'=1}^{G}\int_{4\pi}d\hat{\Omega}'\frac{1}{4\pi}\{\sigma_{s0}^{h'\to h}(\vec{r})\\
&+3\sigma_{s1}^{h'\to h}(\vec{r})\hat{\Omega}.\hat{\Omega}'\}\psi^{h'}_{assem\_fix}(\vec{r},\hat{\Omega}')\\
&+\frac{\chi^{h}}{4\pi k^{c}}\sum_{h'=1}^{G}\nu\sigma_{f}^{h'}(\vec{r})\phi^{h'}_{assem\_fix}(\vec{r})\\
&\text{BC:}\psi^{h}_{assem\_fix}(\vec{r}_s,\hat{\Omega})=\psi^{h}_{decom\_swp}(\vec{r}_s,\hat{\Omega});\hat{\Omega}.\hat{n}_s<0
\end{aligned}
\tag{3.26}
$$

To summarize, the following steps are followed in the new HSGD method.

1. Perform fine-group assembly calculations with approximate boundary conditions (e.g., specular reflective) to generate coarse-group and decomposition cross sections in Eqs. (3.4)- (3.8), (3.19), (3.22) and (3.23) using the approximate flux spectrum.
2. Solve the coarse-group whole-core high-order diffusion equations, Eq. (3.18), using the cross sections generated in step (1).
3. Perform a transport decomposition sweep for each subgroup by solving Eq. (3.21) using the decomposition cross sections generated in step (1) with the coarse-group eigenvalue and scalar flux obtained in step (2).
4. Perform stabilizing scheme (*i.e.*, CS or AFC) using the decomposed flux spectrum obtained from step (3). The updated fine-group flux is used to update the coarse-group and decomposition cross sections.
5. Repeat steps (2) - (4) until the user defined successive iteration criteria for coarse-group flux and eigenvalue of Eq. (3.27) is met where the subscript "p" is the iteration number.

$$\left|\frac{\phi_{p+1}^{c}(\vec{r})-\phi_{p}^{c}(\vec{r})}{\phi_{p+1}^{c}(\vec{r})}\right|_{max}<(\varepsilon_{\phi})_{re-cond}$$
$$\left|\frac{k_{p+1}^{c}-k_{p}^{c}}{k_{p+1}^{c}}\right|_{max}<(\varepsilon_{k})_{re-cond} \tag{3.27}$$

3.3 Numerical Results

In this section, the new HSGD method is tested in the 1D BWR and HTTR benchmark problems described in Chapter 2 (Douglass and Rahnema, 2010). The reference solution is obtained by solving a 47-group transport problem with the flux and eigenvalue convergence criteria of 10^{-5} and 10^{-8} , respectively. The problem is solved using HSGD and TSGD methods (high-order diffusion equations in HSGD or transport in TSGD) in which a 2-group problem (6-group in HTTR) is solved iteratively with the coarse-group flux and eigenvalue convergence criteria set to 10^{-5} and 10^{-8} while the successive iteration criteria were chosen as $(\varepsilon_{\phi})_{re-cond} = 10^{-3}$ and $(\varepsilon_{k})_{re-cond} = 10^{-4}$. For consistent comparison, the spatial discretization is kept the same for the fine-group and coarse-group problems with a resolution of half mean free path (in thermal energy) in every mesh. Transport corrected cross sections are used for this problem. This would simplify the definition of Δ^c in Eq. (3.19) to Eq. (3.28).

$$\Delta^c(\vec{r}) = \frac{\sum_{h\in c}[\sigma_{tr}^c(\vec{r}) - \sigma_{tr}^h(\vec{r})]J^h(\vec{r})}{\sum_{h\in c}\phi^h(\vec{r})} + \frac{\sum_{h\in c}[\frac{1}{3}\nabla\phi^h(\vec{r}) - \nabla.\overleftrightarrow{\Pi}^h(\vec{r})]}{\sum_{h\in c}\phi^h(\vec{r})} \tag{3.28}$$

For the numerical results, the average, mean relative and maximum errors are defined as:

$$AVG^c = \frac{\int dx|e^c(x)|}{\int dx} \tag{3.29}$$

$$MRE^c = \frac{\int dx |e^c(x)| \phi^c_{re-cond}(x)}{\int dx \phi^c_{ref}(x)} \tag{3.30}$$

$$MAX^c = \max(|e^c(x)|) \tag{3.31}$$

where,

$$e^c(x) = 100\% \frac{\phi^c_{ref}(x) - \phi^c_{re-cond}(x)}{\phi^c_{ref}(x)} \tag{3.32}$$

and

$$\phi^c_{ref} = \sum_{g \in c} \phi^g_{ref} \tag{3.33}$$

3.3.1 1D BWR Problem

As seen in Table 3.1, the 2g HSGD and TSGD methods are able to predict the fine-group flux and eigenvalue with high accuracy in the ARO configuration. The relative flux error is comparable for both methods and this is a confirmation of replacing the TSGD method with the HSGD method while increasing its computational efficiency. Figures 3.2 and 3.3 demonstrate the relative fast and thermal flux errors for CS and AFC stabilizing schemes. Small error oscillations are noticed in Figure 3.3 for the HSGD method. This is due to rapid sign change of Δ^c for adjacent meshes in Eq. (3.19) since this term includes the first

moment of energy-angle coupling and the high-order angular effect. Nonetheless, the high-order diffusion equations are able to track the transport solution in a numerically stable pattern. Figure 3.1 shows the thermal and fast scalar flux in the ARO configuration.

Table 3.1. Relative flux error and eigenvalue error of 2g HSGD and TSGD using CS and AFC stabilizing schemes in ARO configuration

	$k_{47g-ref}$=1.066813		AVG(%)		MAX(%)		MRE(%)	
	k_{2g}	Δk^a (pcm)	Fast	Thermal	Fast	Thermal	Fast	Thermal
2g TSGD-CS[b]	1.066815	-0.2	0.02	0.03	0.04	0.11	0.02	0.02
2g HSGD-CS	1.066805	0.8	0.01	0.02	0.05	0.08	0.01	0.02
2g TSGD-AFC[c]	1.066821	-0.8	0.08	0.09	0.14	0.16	0.07	0.08
2g HSGD-AFC	1.066811	0.2	0.07	0.07	0.13	0.19	0.07	0.07

[a] $\Delta k = (k_{47g-ref} - k_{2g}) \times 10^5$
[b] Core Sweeping
[c] Assembly level Fixed-source Calculations

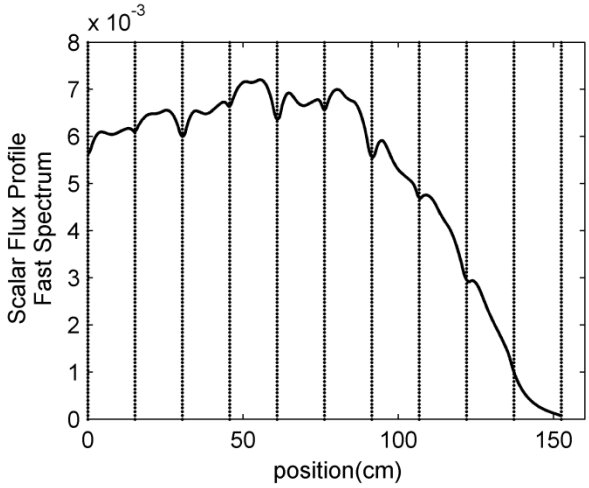

(a) Fast spectrum

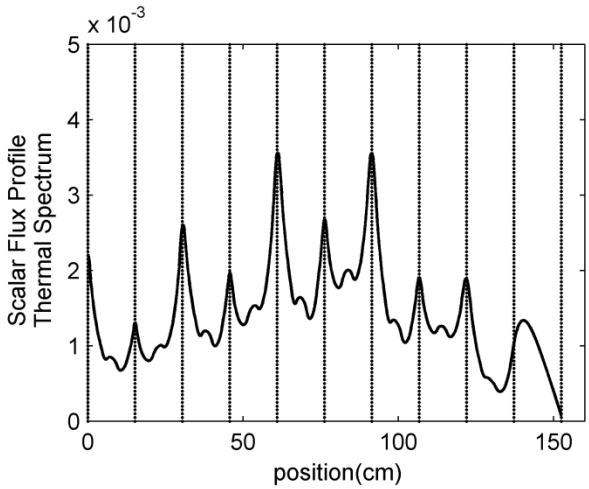

(b) Thermal spectrum

Figure 3.1. Scalar flux profile in ARO configuration of 1D BWR core. The vertical lines represent the interface of assemblies.

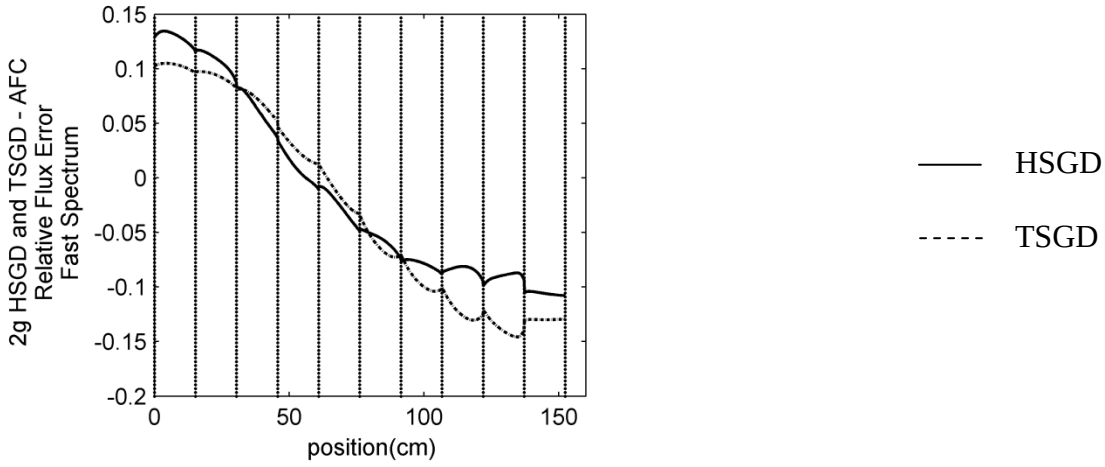

(a) Relative fast flux error

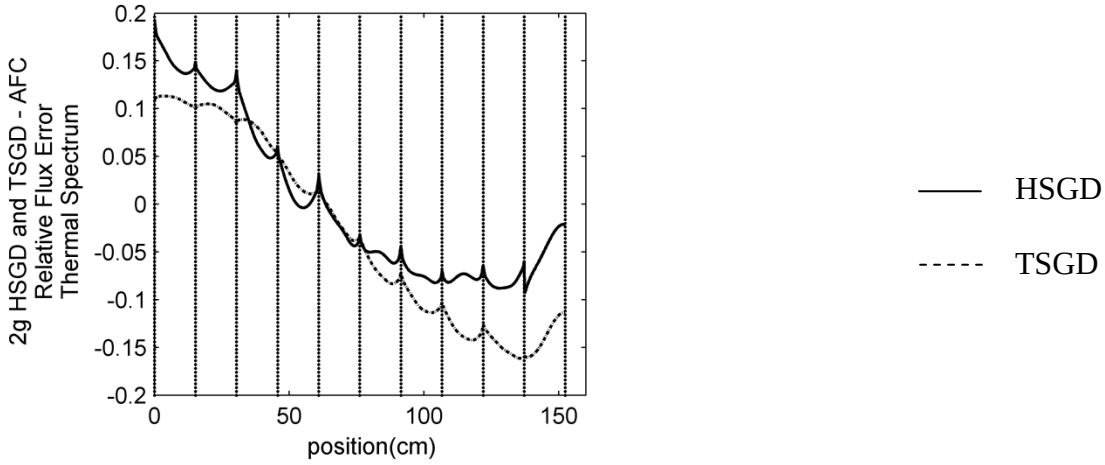

(b) Relative thermal flux error

Figure 3.2. Relative flux error of 2-group (in percent) HSGD and TSGD using AFC scheme in ARO configuration of 1D BWR core

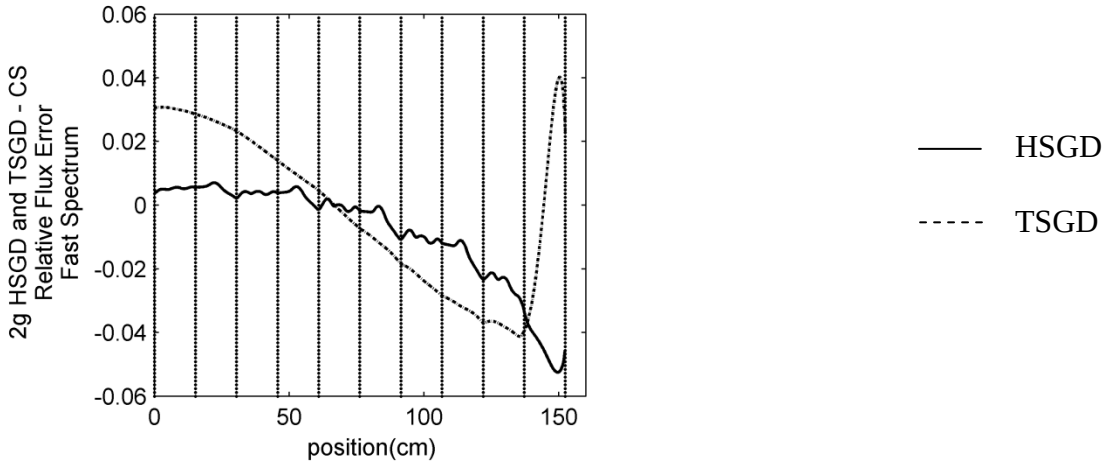

(a) Relative fast flux error

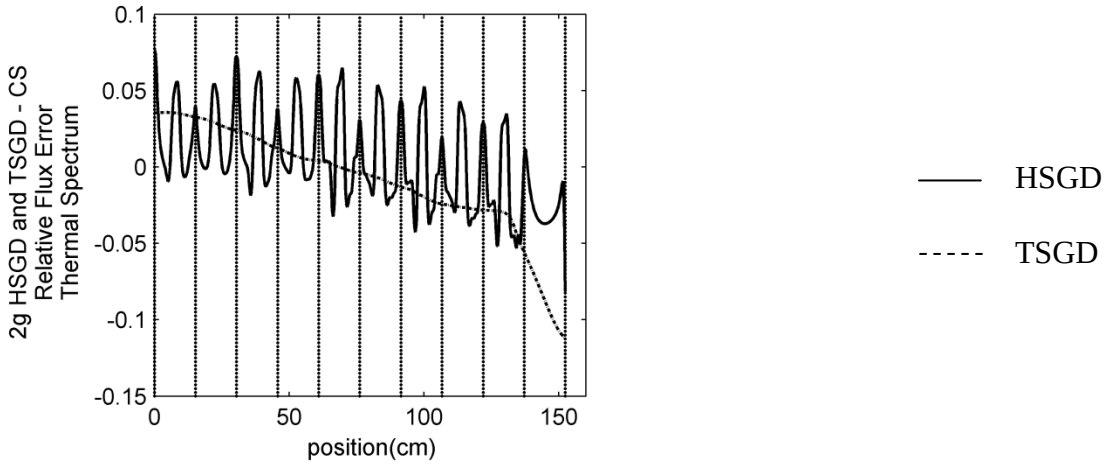

(b) Relative thermal flux error

Figure 3.3. Relative flux error of 2-group (in percent) HSGD and TSGD using CS scheme in ARO configuration of 1D BWR core

Table 3.2 compares the eigenvalue and relative flux errors for the HSGD and TSGD methods using two different stabilizing schemes in the SRI configuration. From the relative flux error it is noticed that the CS stabilizing scheme has superior performance compared to AFC. The HSGD method has reproduced the fine-group flux in SRI configuration with comparable accuracy to the TSGD method. Figure 3.4 demonstrates

the fast and thermal flux in SRI configuration while Figures 3.5 and 3.6 show the relative flux error for the HSGD and TSGD methods using CS and AFC schemes.

Table 3.2. Relative flux error and eigenvalue error of 2g HSGD and TSGD using CS and AFC stabilizing schemes in SRI configuration

	$k_{47g-ref}$=1.003437		AVG(%)		MAX(%)		MRE(%)	
	k_{2g}	$\Delta k\ (pcm)$	Fast	Thermal	Fast	Thermal	Fast	Thermal
2g TSGD-CS	1.003438	-0.1	0.01	0.01	0.03	0.02	0.01	0.01
2g HSGD- CS	1.003426	1.1	0.01	0.02	0.03	0.08	0.01	0.02
2g TSGD- AFC	1.003463	-2.6	0.22	0.23	0.41	0.50	0.19	0.23
2g HSGD-AFC	1.003434	0.3	0.17	0.18	0.34	0.37	0.14	0.18

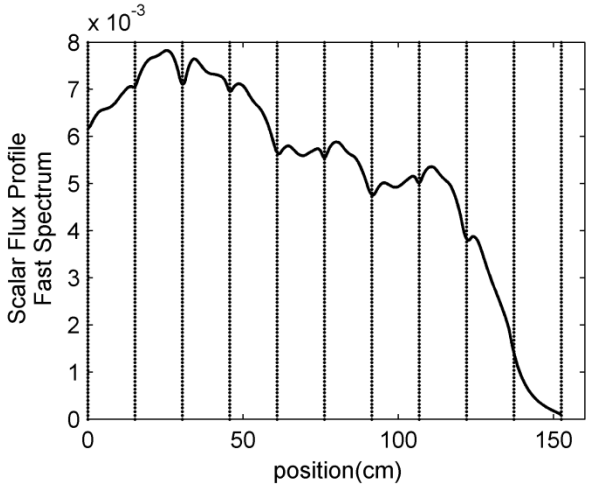

(a) Fast spectrum

Figure 3.4. Scalar flux profile in SRI configuration of 1D BWR core. The vertical lines represent the interface of assemblies.

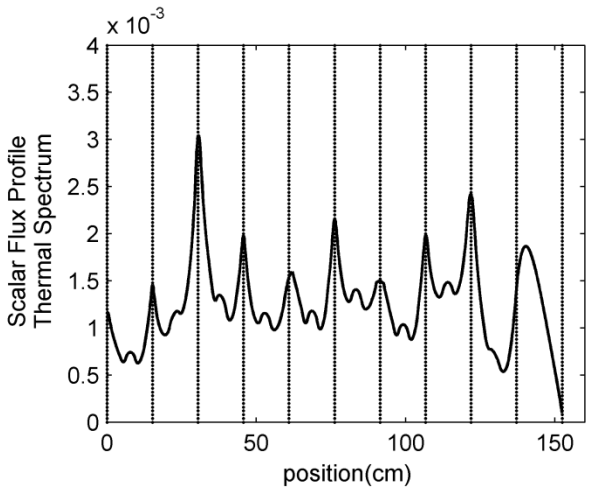

(b) Thermal spectrum

Figure 3.4 continued

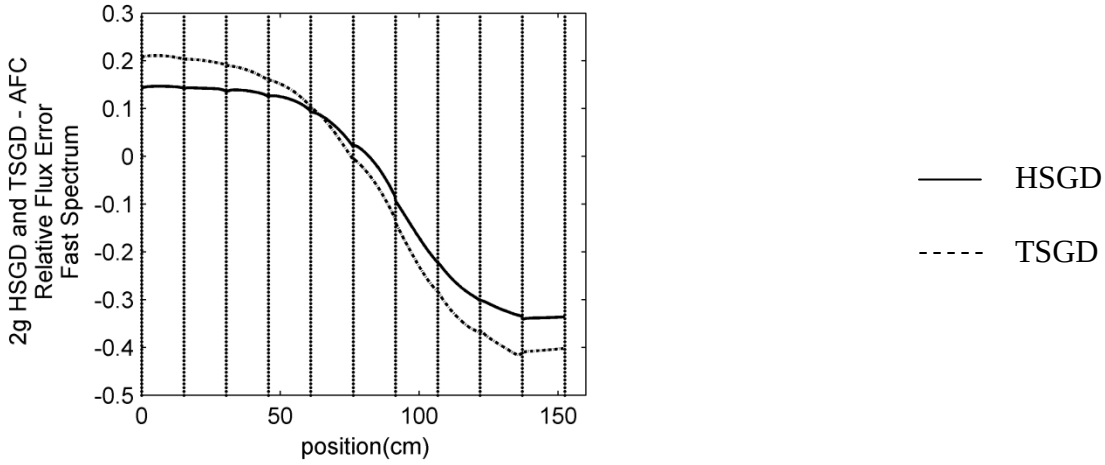

(a) Relative fast flux error

Figure 3.5. Relative flux error of 2-group (in percent) HSGD and TSGD using AFC scheme in SRI configuration of 1D BWR core

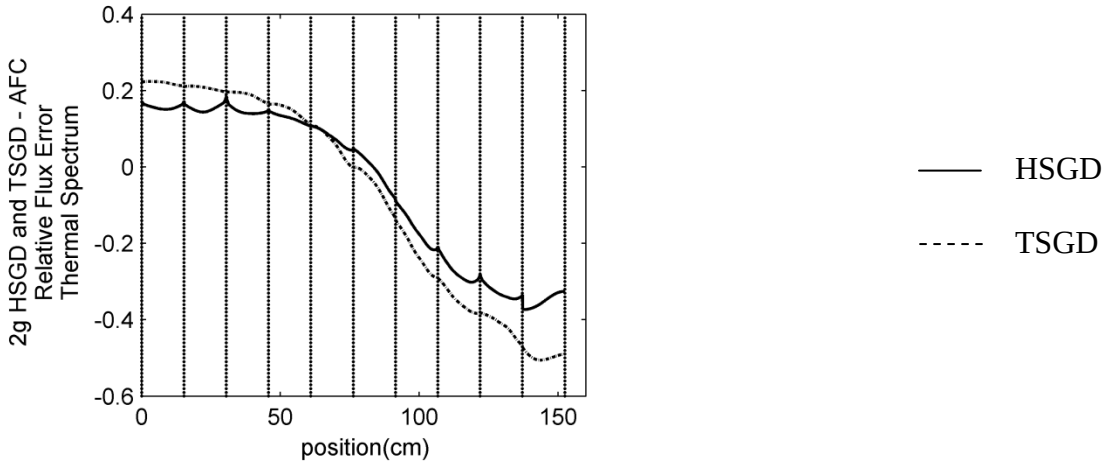

(b) Relative thermal flux error

Figure 3.5 continued

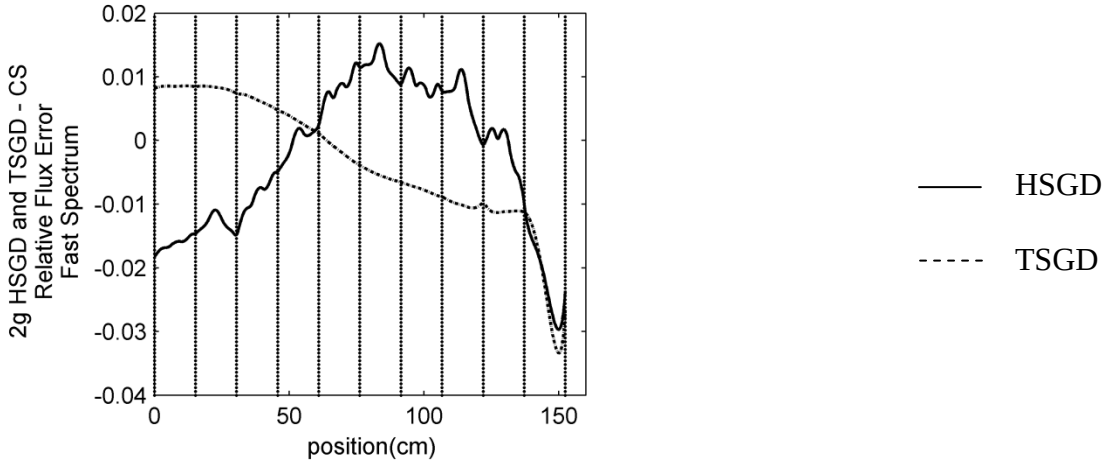

(a) Relative fast flux error

Figure 3.6. Relative flux error of 2-group (in percent) HSGD and TSGD using CS scheme in SRI configuration of 1D BWR core

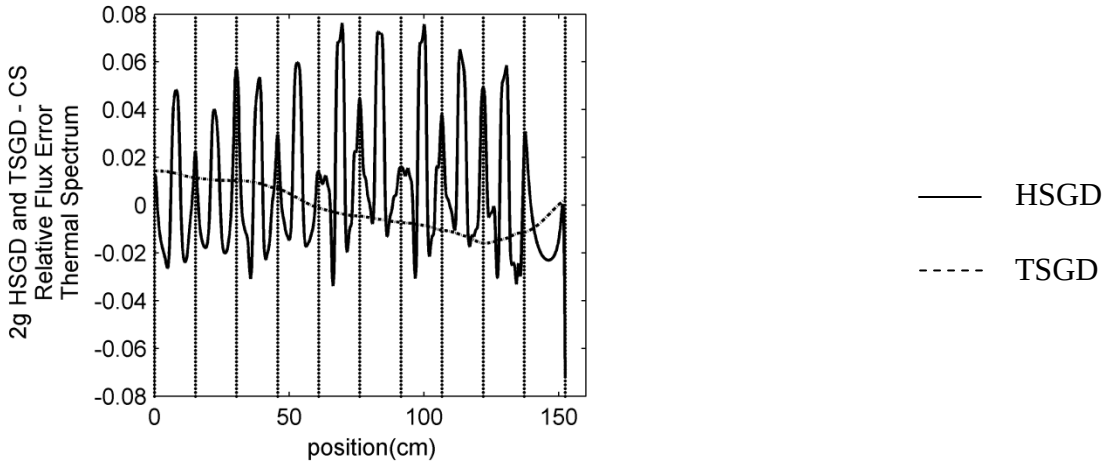

(b) Relative thermal flux error

Figure 3.6 continued

Computational efficiency of the HSGD and TSGD methods are shown in Table 3.3. The computation times are normalized to the transport reference (47-group) computation time to highlight the method. The *c*-iteration index refers to the number of iterations the coarse-group cross sections are updated. The *s*-iteration in CS scheme is the number of times the stabilizing scheme is applied which is equal to the *c*-iteration. However, the *l*-iteration for AFC scheme refers to the maximum cumulative local iterations per assembly to ensure convergence of the fixed-source problem during re-condensation. In addition, the *c*-iteration for the reference case specifies the number of source iterations without any acceleration scheme. It is seen that the HSGD method is 12 and 16 times faster using CS scheme in the ARO and SRI configurations, respectively. Although the TSGD method increases computational speed 5 times compared to the reference fine-group case, its efficiency is amplified 2-3 times using high-order diffusion equations for coarse-group calculations.

Table 3.3. Computational efficiency of HSGD and TSGD versus fine-group transport for two configurations of 1D BWR core

1D BWR		*NCT*[a]	*c-iteration*	*s-iteration*	*l-iteration*
ARO	*47g- Reference*	1	3267	-	-
	2g HSGD-CS	0.080	20	20	-
	2g HSGD-	0.279	6	-	2354
	2g TSGD-CS	0.195	17	17	-
	2g TSGD-AFC	0.352	6	-	2365
SRI	*47g- Reference*	1	5829	-	-
	2g HSGD- CS	0.059	20	20	-
	2g HSGD-	0.179	6	-	2515
	2g TSGD-CS	0.152	20	20	-
	2g TSGD-	0.242	6	-	2570

[a] Normalized Computation Time

3.3.1 1D HTTR Problem

In the HTTR benchmark problem, the coarse-group problem is solved in 6 coarse groups using HSGD and TSGD with the coarse-group flux and eigenvalue convergence criteria set to 10^{-5} and 10^{-8} while the successive iteration criteria were chosen as $(\varepsilon_{\phi})_{re-cond} = 10^{-3}$ and $(\varepsilon_{k})_{re-cond} = 10^{-4}$.

As seen from Table 3.4, the HSGD and TSGD reproduce the fine-group solution with comparable accuracy in ARO configuration. However, the magnitude of error for HSGD is larger in the HTTR core compared to the BWR core.

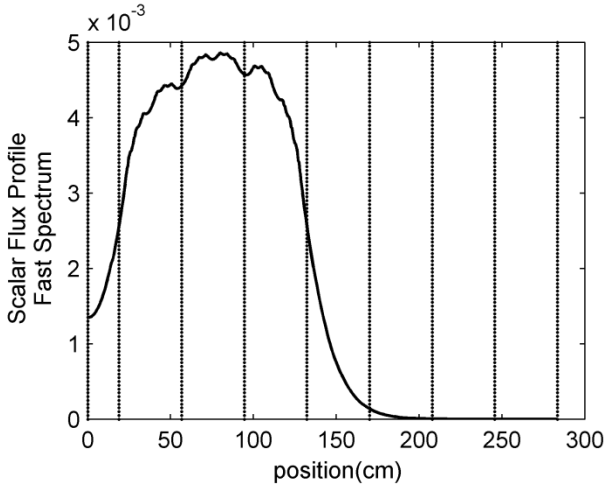

(a) Fast spectrum

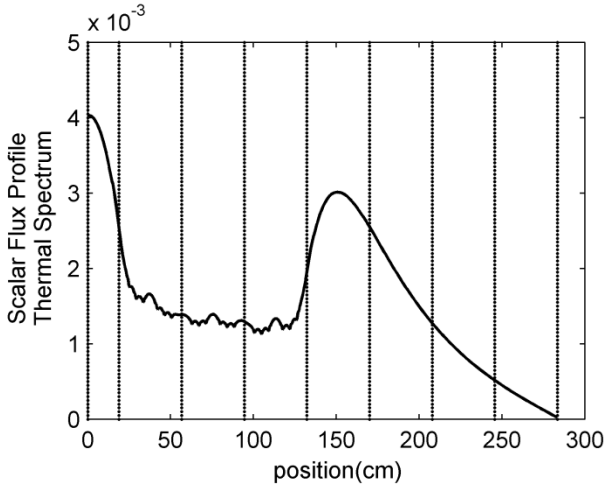

(b) Thermal spectrum

Figure 3.7**.** Scalar flux profile in ARO configuration of 1D HTTR core. The vertical lines represent the interface of assemblies.

As seen from Figures 3.8 and 3.9, larger error exhibits for the fast spectrum and the magnitude of the error increases away from the fissionable block toward the reflector, confirming that the error is pronounced in the reflector region in which no fission is present and hence the net current for each mesh mainly determines the magnitude of the scalar flux. This error is due the constant assumption of the Δ^c while in fact it is a

function of space in each mesh. By decreasing the mesh size in the reflector region, it is verified that the magnitude of error decreases and the spatial error in Δ^c is the main reason for the errors shown in Tables 3.4 and 3.5. However, since this error is more pronounced in the fast flux in ARO configuration, the eigenvalue error is negligible. Figure 3.8 shows the error for HSGD and TSGD using AFC scheme in ARO configuration while Figure 3.9 shows the error of CS scheme.

Table 3.4. Relative flux error and eigenvalue error of 6g HSGD and TSGD using CS and AFC stabilizing schemes in ARO configuration

	$k_{47g-ref}$=1.102972		AVG(%)		MAX(%)		MRE(%)	
	k_{6g}	Δk^a (pcm)	Fast	Thermal	Fast	Thermal	Fast	Thermal
6g TSGD-CS	1.102976	-0.4	0.03	0.01	0.15	0.05	0.01	0.01
6g HSGD-CS	1.102981	-0.9	0.14	0.01	0.43	0.34	0.02	0.01
6g TSGD-AFC	1.102971	0.1	0.01	0.01	0.03	0.04	0.01	0.01
6g HSGD-AFC	1.102980	-0.8	0.12	0.04	0.46	0.10	0.03	0.03

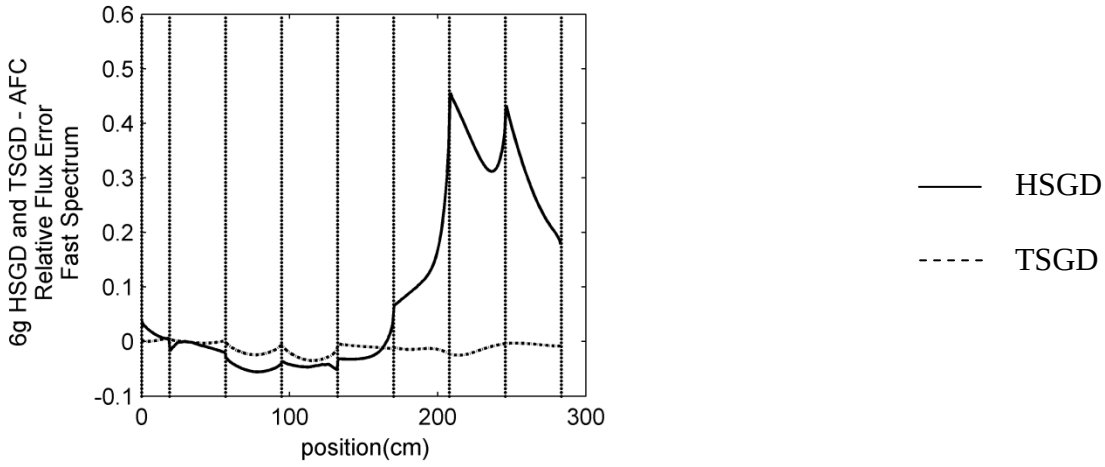

(a) Relative fast flux error

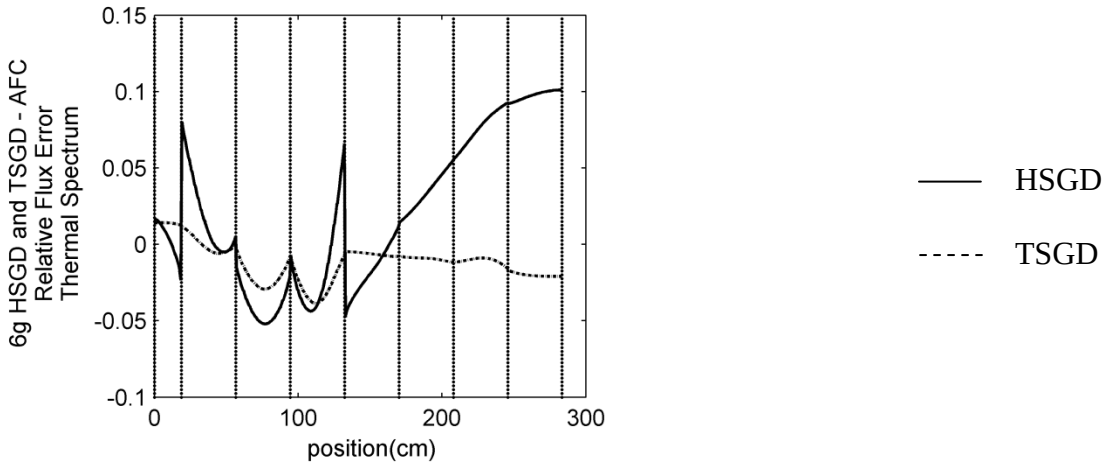

(b) Relative thermal flux error

Figure 3.8. Relative flux error (in percent) of 6-group HSGD and TSGD using AFC scheme in ARO configuration of 1D HTTR core

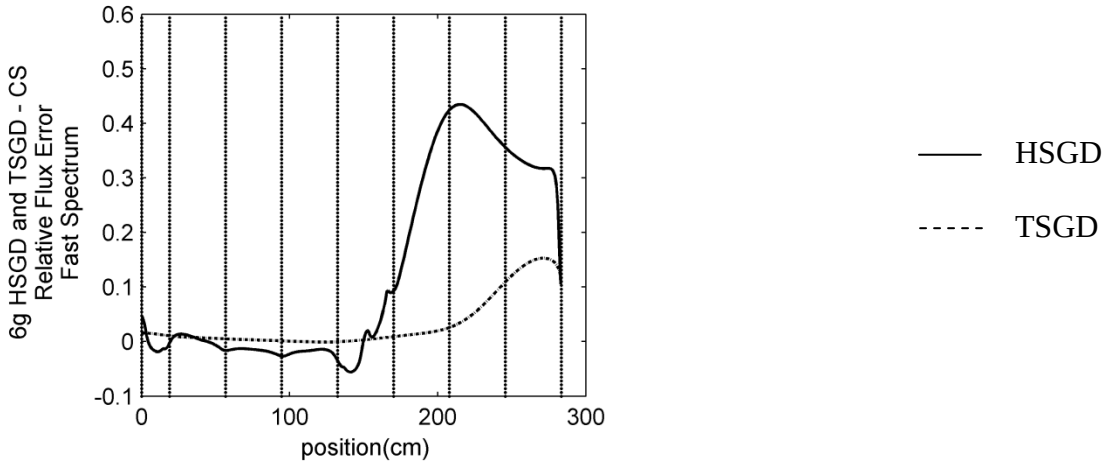

(a) Relative fast flux error

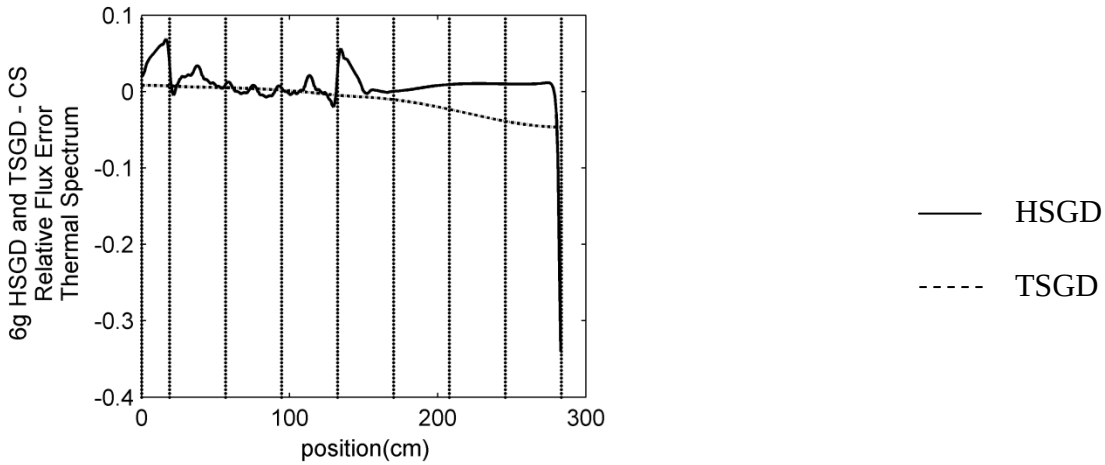

(b) Relative thermal flux error

Figure 3.9. Relative flux error (in percent) of 6-group HSGD and TSGD using CS scheme in ARO configuration of 1D HTTR core

In Table 3.5, the eigenvalue and flux error for HSGD and TSGD in ARI configuration is shown. Due to the presence of control rods, the magnitude of the thermal flux error is increased and the HSGD exhibits larger error in the eigenvalue compared to the ARO

configuration. Figure 3.11 demonstrates the fast and thermal flux error using AFC scheme in the ARI configuration while the flux error using CS scheme is shown in Figure 3.12.

Table 3.5. Relative flux error and eigenvalue error of 6g HSGD and TSGD using CS and AFC stabilizing schemes in ARI configuration

	$k_{47g-ref}$=0.829591		AVG(%)		MAX(%)		MRE(%)	
	k_{6g}	Δk^a (pcm)	Fast	Thermal	Fast	Thermal	Fast	Thermal
6g TSGD-CS	0.829591	0.0	0.01	0.08	0.10	0.36	0.00	0.00
6g HSGD-CS	0.829645	-5.4	0.09	0.09	0.30	0.52	0.01	0.03
6g TSGD-AFC	0.829598	-0.7	0.01	0.10	0.07	0.39	0.02	0.02
6g HSGD-AFC	0.829629	-3.8	0.10	0.08	0.40	0.36	0.02	0.03

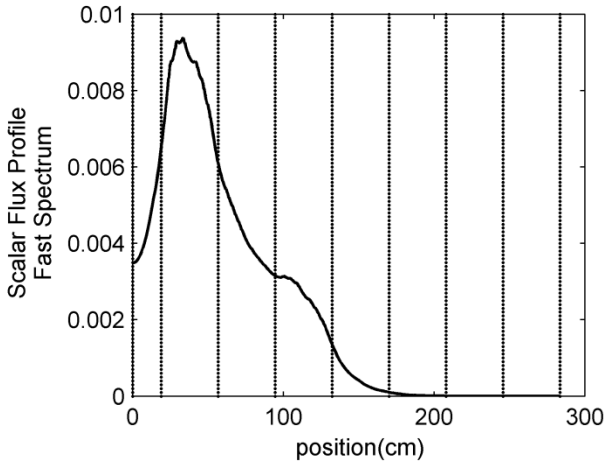

(a) Fast spectrum

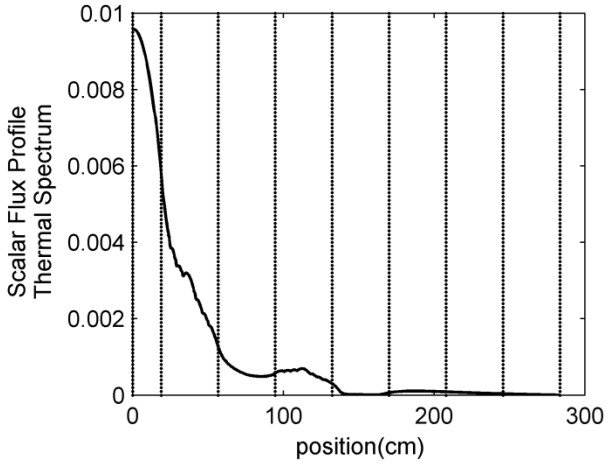

(b) Thermal spectrum

Figure 3.10. Scalar flux profile in ARI configuration of 1D HTTR core. The vertical lines represent the interface of assemblies.

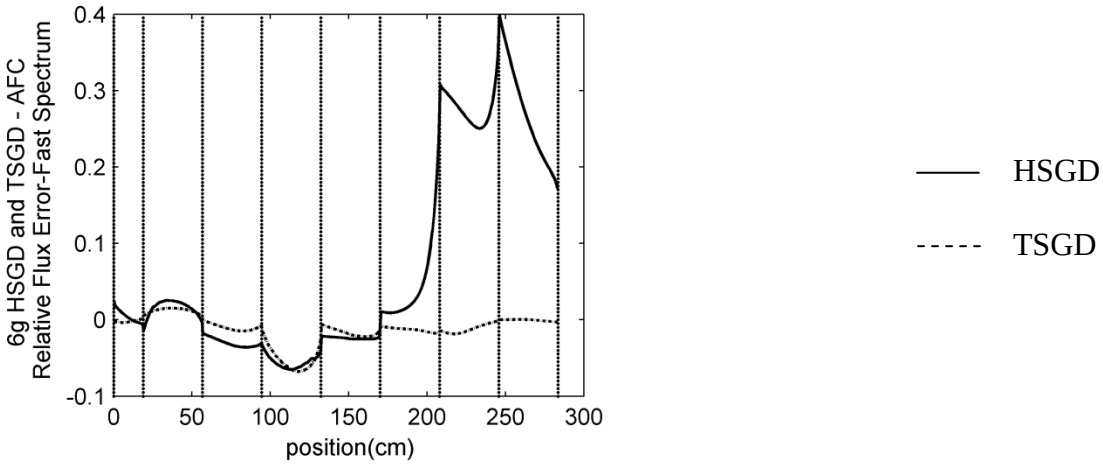

(a) Relative fast flux error

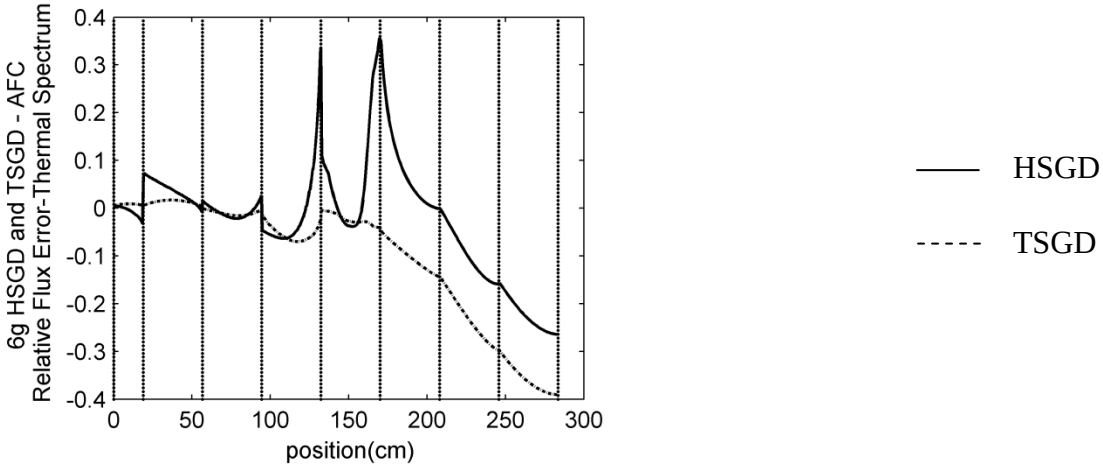

(b) Relative thermal flux error

Figure 3.11. Relative flux error (in percent) of 6-group HSGD and TSGD using AFC scheme in ARI configuration of 1D HTTR core

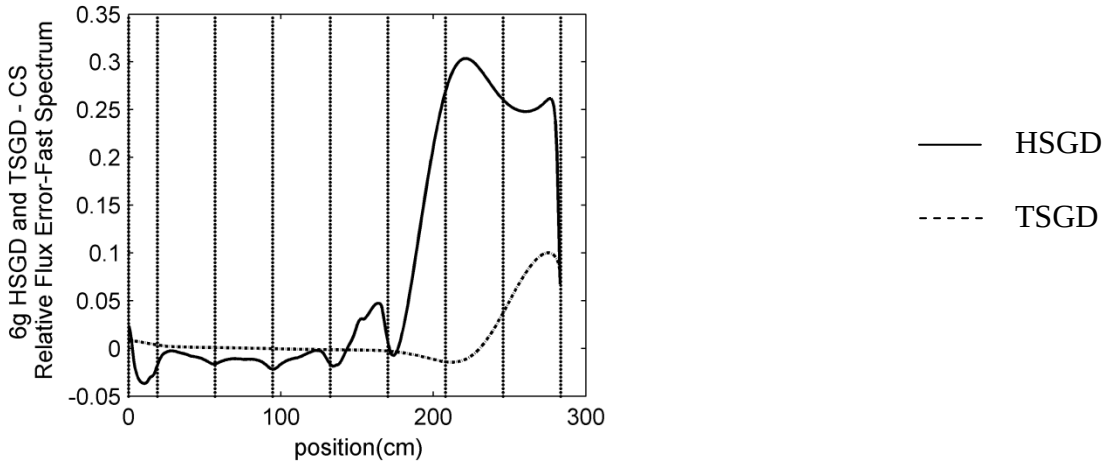

(a) Relative fast flux error

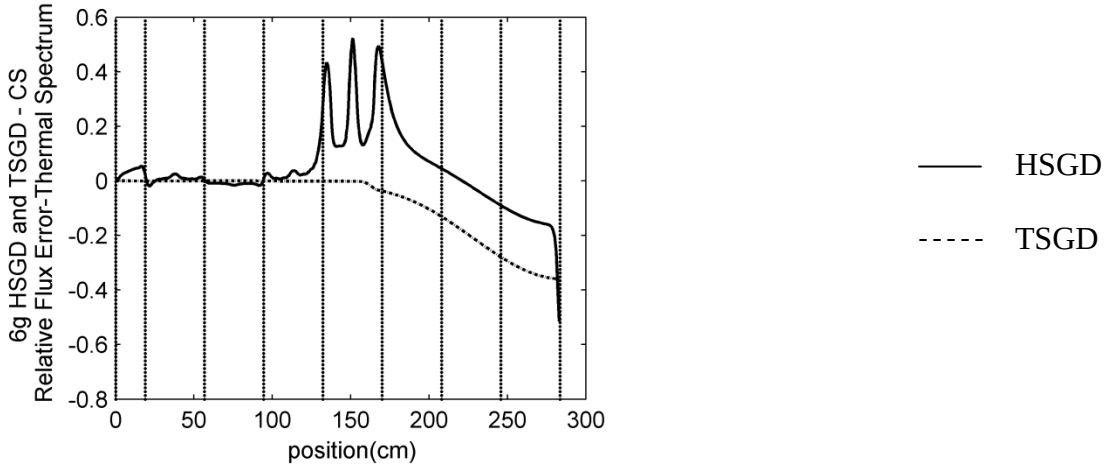

(b) Relative thermal flux error

Figure 3.12. Relative flux error (in percent) of 6-group HSGD and TSGD using CS scheme in ARI configuration of 1D HTTR core

Computational efficiency of the HSGD and TSGD methods are shown in Table 3.6. It is seen that TSGD increases the computational speed by a factor of 2 while HSGD amplifies this efficiency by a factor of 3. The AFC scheme is a preferred scheme for

TSGD method in the HTTR core. However, from Table 3.6, it can be inferred that CS scheme is a preferred stabilizing scheme for HSGD and it will be used for future work.

Table 3.6. Computational efficiency of HSGD and TSGD versus fine-group transport for two configurations of 1D HTTR core

1D HTTR		*NCT*	*c-iteration*	*s-iteration*	*l-iteration*
ARO	*47g- Reference*	1	5900	-	-
	6g HSGD-CS	0.302	40	40	-
	6g HSGD-AFC	0.291	9	-	2163
	6g TSGD-CS	0.714	40	40	-
	6g TSGD-AFC	0.498	9	-	2143
SRI	*47g- Reference*	1	5294	-	-
	6g HSGD- CS	0.291	39	39	-
	6g HSGD-AFC	0.303	9	-	2383
	6g TSGD-CS	0.685	40	40	-
	6g TSGD-	0.535	9	-	2261

3.4 Concluding Remarks and Future work

In this chapter, a new hybrid method (HSGD) for accelerating multi-group eigenvalue transport problems has been developed. This method in essence is an extension of the subgroup decomposition method which directly couples a consistent coarse-group criticality calculation with a set of fixed-source transport decomposition sweeps to obtain the fine-group spectrum. Here, a consistent high-order diffusion method is developed to more efficiently perform the coarse-group criticality calculation.

The new method's accuracy and computational efficiency were determined in 1D BWR and HTTR benchmark problems. It was found that the method is highly accurate and

efficient, producing results close to those obtained from a direct fine group transport calculation with 12-16 times faster speed in the BWR core (depending on the control rod configuration) and 3 times faster speed in the HTTR problem. It was also found that the core sweeping scheme is a more efficient stabilizing scheme than the assembly level fixed-source calculations for 4 configurations. Hence, core sweeping is recommended as the preferred stabilizing scheme.

It has been observed that the accuracy and computational efficiency of the subgroup decomposition method using core sweeping stabilizing scheme is highly dependent on the number of coarse groups due to the assumption of constant perturbation cross section. In the problems considered, increasing the number groups improves the accuracy of the results. This increases the impact of problem dependency and requires optimization. However, the subgroup decomposition method using the assembly fixed-source stabilizing scheme is almost independent of the number of coarse groups and thereby reducing the need for optimization for various reactor systems. Thus, in the extension of this method to 2D and 3D geometries, assembly level fixed-source calculation is believed to be a better choice as the stabilizing scheme is less problem dependent. Nonetheless, this stabilizing scheme requires detailed flux shape (space and angle) at the interface of each assembly which would increase the computational burden. The angular details can be omitted by incorporating the high-order diffusion theory for the fine-group fixed-source calculation and hence, accelerating the stabilizing scheme particularly for 3D geometries.

As future work, implementation of the method in 3D geometry is highly desirable for practical application in addition to increased computational efficiency. The hybrid subgroup decomposition method in its current form does not accommodate spatial homogenization. Therefore, a method that couples hybrid subgroup decomposition with spatial homogenization would be an interesting study.

3.5 References

Anistratov, D. Y., 2005. Consistent Spatial Approximation of the Low-Order Quasi-Diffusion Equations on Coarse Grids. Nuclear Science and Engineering, 149, 138-161.

Anistratov, D. Y., 2011. Multi-level Nonlinear Diffusion Acceleration method for multigroup transport k-eigenvalue problems. International Conference on Mathematics and Computational Methods Applied to Nuclear Science and Engineering, Rio de Janeiro, RJ, Brazil, May 8-12.

Anistratov, D. Y., Gol'din, V.Ya., 2011. Multilevel Quasidiffusion Methods for Solving Multigroup Neutron Transport *k*-Eigenvalue Problems in One-Dimensional Slab Geometry. Nuclear Science and Engineering, 169, 111-132.

Douglass, S., Rahnema, F., 2010. Development of a 1-D boiling water reactor benchmark specification. Transactions of the American Nuclear Society, San Diego, CA, June 13-17, Vol. 102, 543–545.

Douglass, S., Rahnema, F., 2012. Subgroup decomposition method. Annals of Nuclear Energy 48, 84-101.

Kelly, D. J., 1995. Depletion of a BWR lattice using the RACER continuous energy Monte Carlo code. In: Proceedings of the International Conference on Mathematics and Computations, Reactor Physics and Environmental Analyses, Portland, Oregon, April 30–May 4, Vol. 2, 1011.

Simeonov, T., 2003. Release Notes – Helios System Version 1.8. Studsvik Scandpower Report, SSP-03/221, November 26.

Yasseri, S., Rahnema, F., 2013. A High-order Diffusion Theory Subgroup Decomposition method for Accelerating Eigenvalue Transport Solutions. Journal of Computational Physics, Submitted (March).

CONSISTENT SPATIAL HOMOGENIZATION IN TRANPORT THEORY

4.1 Introduction

Current standard homogenization techniques are based on a two-level approach: heterogeneous transport calculations performed at the assembly level with approximate boundary conditions (*i.e.*, specular reflection) followed by a nodal (homogeneous) diffusion theory calculation at the core level. The accuracy of these methodologies deteriorates with increased core and assembly heterogeneities resulting from the desire to increase fuel utilization. Recent works (Aragones and Ahnert, 1986; Mondot and Sanchez, 2003; Nichita and Rahnema, 2003; Joo et al., 2002; Smith, 1994; Roberts et al., 2010) in the context of dynamic hybrid transport-diffusion homogenization have attempted to improve this methodology by iterating on the assembly interface (boundary) condition within the core calculations. In this framework, it is customary to use the modulation technique for recovering the detailed angular and spatial shapes of the incoming angular flux for assembly calculations. As described in Mondot and Sanchez (2003), this technique introduces large local flux errors (pronounced at the assembly interfaces) in full assembly homogenization. In most of these works in dynamic homogenization either the core or assembly averaged errors are reported (Joo et al., 2002; Roberts et al., 2010). These are generally not a good measure of local (e.g., flux or pin power) errors due to many factors including cancellation of errors resulting from simultaneous (Mondot and Sanchez, 2003; Roberts et al., 2010) energy condensation and

homogenization of assembly cross-sections. It is well known nodal diffusion theory at the core level lacks the spatial and angular resolution that is necessary for a robust dynamic transport homogenization. Although, both standard and dynamic homogenization methods predict the eigenvalue relatively accurately, especially in optically thick systems as a result of error cancelation, large local errors in the flux or pin power profile are inevitable due to the effect of core environment and inconsistent homogenization (*i.e.*, neglecting the effect of space and angle coupling).

A fully transport theory based homogenization method can be found in Dorning et al (1997). This work presents a multi-scales systematic theory for simultaneous homogenization of pin cells and fuel assemblies in addition to a self-consistent de-homogenization theory for the reconstruction of the heterogeneous transport solution. In this method an asymptotic expansion of the heterogeneous transport equation using spatial scales leads to a set of equations that involve the following main steps for implementation: "the homogenization of the heterogeneous lattice; the homogenization of the lattice-cell-homogenized fuel assembly; the fuel-assembly-homogenized coarse-mesh global nodal diffusion calculation; and the local heterogeneous flux reconstruction with the fuel assemblies and lattice cells."(Dorning et al, 1997) This work was developed for one-speed eigenvalue problems where the heterogeneous core is comprised of a 2D near-periodic array of fuel assemblies. The rigorous derivation of this work has not been extended to multi-group eigenvalue problems.

Homogenization via perturbation theory was initially introduced in the context diffusion theory by Rahnema, 1989. In this work, cross sections can be re-homogenized on-the-fly within the core calculation by using the coarse-mesh interface/boundary condition. This work was later extended to n^{th}-order in transport theory for eigenvalue problems (Mckinley and Rahnema, 2002). In particular, using an unperturbed (known) solution, formalisms are developed to determine the solution to the neutron transport equation when the boundary condition of the system is perturbed. Additionally, it was shown that high-order cross-section homogenization (Rahnema and Mckinley, 2002) based on boundary condition perturbation in diffusion theory (Mckinley and Rahnema, 2000) improves the accuracy of nodal methods for coarse-mesh eigenvalue calculations. The implementation of this method in three dimensional geometries can be cumbersome as it requires computation of adjoint Green's functions.

One major concern with hybrid (e.g., standard and dynamic) homogenization methods is the lack of adequate phase-space resolution in the low order transport approximation (e.g., homogenized diffusion theory) that leads to significant degradation in accuracy with increasing heterogeneity. To the author's knowledge, there is only one homogenization method in pure transport that overcomes the issues associated with dynamic hybrid homogenization. However, this method (Dorning et al., 1997) is limited to one-speed eigenvalue problems consisting near periodic arrays of assemblies.

In this chapter, by introducing an auxiliary cross-section, a new Consistent Spatial Homogenization (CSH) method in transport theory is developed that reproduces the

heterogeneous solution in its full phase-space resolution. The method is derived in general geometry and continuous energy. The new method is described in section 4.2 and its implementation in 1D slab geometry is found in section 4.3. In section 4.4, two 1D BWR assemblies, a 1D BWR core and an HTTR core are solved to test the method's accuracy and efficiency. Concluding remarks are given in section 4.5.

4.2 Method

For an eigenvalue problem, the fine-mesh heterogeneous angular flux within a homogenized region is governed by Eq. (4.1) shown below.

$$\begin{aligned} &\hat{\Omega}.\nabla\psi(\vec{r},E,\hat{\Omega}) + \sigma(\vec{r},E)\psi(\vec{r},E,\hat{\Omega}) \\ &= \int_{4\pi} d\hat{\Omega}' \int dE'\, \sigma_s(\vec{r},E'\to E,\hat{\Omega}.\hat{\Omega}')\psi(\vec{r},E',\hat{\Omega}') \\ &\quad + \frac{\chi(E)}{4\pi k}\int_{4\pi} d\hat{\Omega}' \int dE'\, \nu\sigma_f(\vec{r},E')\psi(\vec{r},E',\hat{\Omega}') \\ &\qquad \forall \vec{r} \in V^{hom} \end{aligned} \tag{4.1}$$

In this equation, V^{hom} is the volume of the homogenized region, the scattering kernel is assumed to depend on the scattering angle cosine $\mu_0 = \hat{\Omega}.\hat{\Omega}'$, and the fission term is assumed isotropic (not a necessary but common assumption). We postulate that the fine-mesh solution to the homogeneous transport equation with an auxiliary source term as presented in Eq. (4.2), yields the same solution as that of Eq. (4.1).

$$\begin{aligned}
&\hat{\Omega}.\nabla\psi^{hom}(\vec{r},E,\hat{\Omega})+\sigma^{hom}(E)\psi^{hom}(\vec{r},E,\hat{\Omega})\\
&=\int_{4\pi}d\hat{\Omega}'\int dE'\,\sigma_s^{hom}(E'\to E,\hat{\Omega}.\hat{\Omega}')\psi^{hom}(\vec{r},E',\hat{\Omega}')\\
&+\frac{\chi(E)}{4\pi k^{hom}}\int_{4\pi}d\hat{\Omega}'\int dE'\,\nu\sigma_f^{hom}(E')\psi^{hom}(\vec{r},E',\hat{\Omega}')\\
&+\sigma_{aux}(\vec{r},E,\hat{\Omega})\phi_{avg}^{hom}(E);\quad\forall\vec{r}\in V^{hom}
\end{aligned}\tag{4.2}$$

In this equation, the superscript "*hom*" refers to the homogeneous values, ϕ_{avg}^{hom} represents the average scalar flux in the homogenized region and the cross sections are constant in space. In order to calculate the last term in Eq. (4.2) *i.e.*, the auxiliary cross-section Eqs. (4.1) and (4.2) are subtracted from each other while forcing the fine-mesh homogeneous flux to be equal to its fine-mesh heterogeneous counterpart, *i.e.*, $\psi^{hom}(\vec{r},E,\hat{\Omega})=\psi(\vec{r},E,\hat{\Omega})$ and preserving the core/problem eigenvalue, $k=k^{hom}$. This leads to the following definition of $\sigma_{aux}(\vec{r},E,\hat{\Omega})$.

$$\begin{aligned}
\sigma_{aux}(\vec{r},E,\hat{\Omega})&=\frac{\int_{4\pi}d\hat{\Omega}'\int dE'\,\Delta\sigma_s(\vec{r},E'\to E,\hat{\Omega}.\hat{\Omega}')\psi(\vec{r},E',\hat{\Omega}')}{\phi_{avg}(E)}\\
&+\frac{1}{4\pi k}\frac{\int_{4\pi}d\hat{\Omega}'\int dE'\,\chi(E)\Delta\nu\sigma_f(\vec{r},E')\psi(\vec{r},E',\hat{\Omega}')}{\phi_{avg}(E)}\\
&-\frac{\Delta\sigma(\vec{r},E)\psi(\vec{r},E,\hat{\Omega})}{\phi_{avg}(E)}
\end{aligned}\tag{4.3}$$

where,

$$\Delta\sigma_{t,s,f}(\vec{r}) = \sigma_{t,s,f}(\vec{r}) - \sigma_{t,s,f}{}^{hom} \tag{4.4}$$

The subscripts *t,s,f* in Eq. (4.4) are for total (which is suppressed for simplicity), scattering and fission cross sections, respectively. In order to separate the angular and spatial discretization of the homogeneous problem from the heterogeneous one, the auxiliary cross-section should be expanded in a basis function for both angle and space. Applying spherical harmonics in the angular domain and a set of orthogonal basis function in the spatial domain defined as $G_p(\vec{r})$ with a weighting function $w(\vec{r})$ and a normalizing factor a_p, the auxiliary cross-section is simplified to:

$$\begin{aligned}\sigma_{aux}(\vec{r}, E, \hat{\Omega}) &= \sum_{l=0}^{L}\sum_{m=-l}^{l}\sum_{p=0}^{P}\frac{Y_{lm}(\hat{\Omega})}{4\pi}a_p G_p(\vec{r})\sigma_{aux}^{lm,p}(E) \\ &= \sum_{l=0}^{L}\sum_{m=-l}^{l}\sum_{p=0}^{P}\frac{Y_{lm}(\hat{\Omega})}{4\pi}a_p G_p(\vec{r})\{\alpha_{lm,p}(E) + \beta_{lm,p}(E) - \gamma_{lm,p}(E)\}\end{aligned} \tag{4.5}$$

Here, the expansion coefficients are defined as:

$$\alpha_{lm,p}(E) = \frac{\int_{4\pi} d\hat{\Omega}' \int_{4\pi} d\hat{\Omega} \int dE' \int_{V^h} d\vec{r}\, w(\vec{r}) G_p(\vec{r})\, Y_{lm}^*(\hat{\Omega}) \Delta\sigma_s(\vec{r}, E' \to E, \hat{\Omega}.\hat{\Omega}')\psi(\vec{r}, E', \hat{\Omega}')}{\phi_{avg}(E)} \tag{4.6}$$

$$\beta_{lm,p}(E) = \frac{1}{4\pi k}\frac{\int_{4\pi} d\hat{\Omega}' \int_{4\pi} d\hat{\Omega} \int dE' \int_{V^h} d\vec{r}\, w(\vec{r}) G_p(\vec{r})\, Y_{lm}^*(\hat{\Omega}) \chi(E) \Delta\nu\sigma_f(\vec{r}, E')\psi(\vec{r}, E', \hat{\Omega}')}{\phi_{avg}(E)} \tag{4.7}$$

$$\gamma_{lm,p}(E) = \frac{\int_{4\pi} d\hat{\Omega} \int_{V^h} d\vec{r}\, w(\vec{r}) G_p(\vec{r})\, Y_{lm}^*(\hat{\Omega}) \Delta\sigma(\vec{r}, E) \psi(\vec{r}, E, \hat{\Omega})}{\phi_{avg}(E)} \tag{4.8}$$

In order to be consistent with the spatial basis function, the denominator is defined as:

$$\phi_{avg}(E) = a_0 \int\limits_{V^h} d\vec{r} \int\limits_{4\pi} d\hat{\Omega}\, w(\vec{r}) G_0(\vec{r}) \psi(\vec{r}, E, \hat{\Omega}) \tag{4.9}$$

The extra degree of freedom gained by the introduction of the auxiliary term in Eq. (4.2) is used to ensure that the auxiliary reaction is zero in which the integral over the mesh, all energies and solid angle is zero. This choice is achieved by Eq. (4.10).

$$\int dE \int\limits_{4\pi} d\hat{\Omega} \int_{V^h} d\vec{r}\, w(\vec{r})\, \sigma_{aux}(\vec{r}, E, \hat{\Omega}) \phi_{avg}(E) = 0 \tag{4.10}$$

In order to define the three terms in σ_{aux} independently (not a necessary assumption but simplifies the definitions), Eq. (4.10) should be valid for each of them which leads to the following equations since $Y_{00}^*(\hat{\Omega}) = 1$ and $G_0(\vec{r}) = 1$.

$$\alpha_{00,0}(E) = 0 \Rightarrow$$

$$\int dE' \int\limits_{4\pi} d\hat{\Omega}' \int\limits_{4\pi} d\hat{\Omega} \int_{V^h} d\vec{r}\, w(\vec{r})\, \Delta\sigma_s(\vec{r}, E' \to E, \hat{\Omega}.\hat{\Omega}') \psi(\vec{r}, E', \hat{\Omega}') = 0 \tag{4.11}$$

$$\beta_{00,0}(E) = 0$$

$$\Rightarrow \int dE' \int_{4\pi} d\hat{\Omega}' \int_{4\pi} d\hat{\Omega} \int_{V^h} d\vec{r}\, w(\vec{r})\, \chi(E) \Delta\nu\sigma_f(\vec{r}, E')\psi\left(\vec{r}, E', \hat{\Omega}'\right) = 0 \tag{4.12}$$

$$\gamma_{00,0}(E) = 0 \Rightarrow \int_{4\pi} d\hat{\Omega} \int_{V^h} d\vec{r}\, w(\vec{r})\, \Delta\sigma\psi\left(\vec{r}, E, \hat{\Omega}\right) = 0 \tag{4.13}$$

Equations (4.11) - (4.13) lead to the following definitions for the homogenized cross sections.

$$\sigma^{hom}(E) = \frac{\int_{V^h} \sigma(\vec{r}, E)\phi(\vec{r}, E)w(\vec{r})d\vec{r}}{\int_{V^h} \phi(\vec{r}, E)w(\vec{r})d\vec{r}} \tag{4.14}$$

$$\chi(E)\nu\sigma_f{}^{hom}(E') = \frac{\int_{V^h} \chi(E)\nu\sigma_f(\vec{r}, E')\phi(\vec{r}, E')w(\vec{r})d\vec{r}}{\int_{V^h} \phi(\vec{r}, E')w(\vec{r})d\vec{r}} \tag{4.15}$$

$$\begin{aligned} \sigma_s{}^{hom}(E' \to E) &= \int_{-1}^{1} d\mu_0\, \sigma_s{}^{hom}(E' \to E, \mu_0) \\ &= \frac{\int_{V^h} \int_{-1}^{1} d\mu_0\, \sigma_s(\vec{r}, E' \to E, \mu_0)\phi(\vec{r}, E')w(\vec{r})d\vec{r}}{\int_{V^h} \phi(\vec{r}, E')w(\vec{r})d\vec{r}} \end{aligned} \tag{4.16}$$

As seen from Eq. (4.16), the above procedure only defines the homogenized total differential scattering cross-section. If the scattering cross sections of the heterogeneous and homogeneous problem are expanded in spherical harmonics, then the definitions of the angular moments of scattering become arbitrary. However, it is conventional from the numerical point of view to define the angular moments as below (Sanchez, 2009).

$$\sigma_{sl}{}^{hom}(E' \to E) = \frac{\int_{V^h} \sigma_{sl}(\vec{r}, E' \to E)\phi_{lm}(\vec{r}, E')w(\vec{r})d\vec{r}}{\int_{V^h} \phi(\vec{r}, E')w(\vec{r})d\vec{r}} \tag{4.17}$$

where,

$$\sigma_{sl}(\vec{r}, E' \to E) = 2\pi \int_{-1}^{1} P_l(\mu_0)\sigma_{sl}(\vec{r}, E' \to E, \mu_0)\mathrm{d}\mu_0 \tag{4.18}$$

$$P_l(\mu_0) = \frac{1}{2l+1} \sum_{m=-l}^{l} Y_{lm}(\widehat{\Omega})Y_{lm}^*(\widehat{\Omega}') \tag{4.19}$$

and

$$\phi_{lm}(\vec{r}, E') = \int_{4\pi} d\widehat{\Omega}' Y_{lm}^*(\widehat{\Omega}')\psi(\vec{r}, E', \widehat{\Omega}') \tag{4.20}$$

Recall that the CSH method assumes *a priori* knowledge of the heterogeneous flux. However, the heterogeneous flux can be approximated by performing single assembly transport calculations with specular reflective boundary condition as is done in standard homogenization methods. Since the CSH method is in pure transport theory, re-homogenization at the core level is expected to be robust and unlike the dynamic homogenization method the spatial and angular resolution is not an issue. The re-homogenization (*i.e.*, on-the-fly homogenization) produces the exact heterogeneous solution within the truncation errors. The homogenization procedure is described below.

1. Perform heterogeneous calculations at the single assembly level and generate initial homogenized and auxiliary cross sections for each assembly using Eqs. (4.5) – (4.8) and Eqs. (4.14) – (4.16). The initial eigenvalue in the auxiliary cross-section is set to 1.
2. Solve the homogeneous whole-core transport equation (inner iteration) using the homogenized cross sections generated in step (1).
3. Expand the core level incoming flux at the surface of each assembly in angle and space as show below. If basis functions are defined as $\varphi^{\rho}_{-,\alpha}$ where ρ is the order of expansion, α is the distinctive surface and the minus sign represents the incoming direction *i.e.*, $\hat{\Omega}.\hat{n} < 0$, then the incoming flux can be written as:

$$\psi_{-}\left(\overrightarrow{r_{\alpha}}, E, \hat{\Omega}\right) = \sum_{\rho} J^{\rho}_{-,\alpha}(E)\varphi^{\rho}_{-,\alpha}(\overrightarrow{r_{\alpha}}, \hat{\Omega}); \forall \overrightarrow{r_{\alpha}} \in S_{\alpha} \tag{4.21}$$

where,

$$J^{\rho}_{-,\alpha}(E) = \pi S_{\alpha} \int_{S_{\alpha}} dS \int_{\hat{\Omega}.\hat{n}<0} d\hat{\Omega}\left|\hat{\Omega}.\hat{n}\right|\varphi^{\rho}_{-,\alpha}(\overrightarrow{r_{\alpha}}, \hat{\Omega})\psi(\vec{r}, E, \hat{\Omega}) \tag{4.22}$$

The basis function should have the following property:

$$\int_{S_{\alpha}} dS \int_{\hat{\Omega}.\hat{n}<0} d\hat{\Omega}\left|\hat{\Omega}.\hat{n}\right|\varphi^{\rho}_{-,\alpha}(\overrightarrow{r_{\alpha}}, \hat{\Omega})\varphi^{\nu}_{-,\beta}(\overrightarrow{r_{\beta}}, \hat{\Omega}) = \frac{1}{\pi S_{\beta}}\delta_{\alpha\beta}\delta_{\rho\nu} \tag{4.23}$$

4. Perform heterogeneous fixed-source calculations at the assembly level with the core eigenvalue from step (2) and incoming flux computed in step (3) using expansion coefficients and the surface basis functions. The key point for expanding the incoming flux in a set of pre-defined basis functions is to separate the angle and spatial discretization at the core level from the assembly calculations. Using the flux distribution from the single assembly calculations and the core eigenvalue, the homogenized and auxiliary cross sections are updated. The updated values include the effect of the core environment due to the improved assembly boundary conditions.
5. Repeat steps (2) - (4) until the user defined successive iteration criteria for flux and eigenvalue of Eqs. (4.24) and (4.25) are met (outer iteration) where the subscript "*p*" is the iteration index.

$$\left|\frac{\phi^{hom}_{avg,(p+1)}(\vec{r},E)-\phi^{hom}_{avg,(p)}(\vec{r},E)}{\phi^{hom}_{avg,(p+1)}(\vec{r},E)}\right|_{max} < (\varepsilon_{\phi})_{re-hom} \tag{4.24}$$

$$\left|\frac{k^{hom}_{(p+1)}-k^{hom}_{(p)}}{k^{hom}_{(p+1)}}\right|_{max} < (\varepsilon_{k})_{re-hom} \tag{4.25}$$

4.3 Implementation in 1D Slab Geometry

The CSH method has been derived in general case. However for the purpose of initial verification and illustration, it is implemented in 1D. Thus it is instructive to highlight the derivation in 1D. For the sake of simplicity, the scattering kernel is treated as isotropic

and transports corrected cross sections are applied. Multi-group approximation is used for the rest of the chapter.

In 1D geometries, the Legendre polynomials are substituted for spherical harmonics. The auxiliary cross-section over a homogenized region $x\epsilon[0,a]$ is defined as:

$$\sigma_{aux}^{g}(x,\mu)=\left\{\frac{1}{2}\sum_{g'}\left[\sigma_{s0}^{g'\to g}(x)-\sigma_{s0}^{hom,g'\to g}\right]\phi^{g'}(x)\right.$$
$$+\frac{1}{2k}\sum_{g'}\left[\chi^{g}\upsilon\sigma_{f}^{g'}(x)-\chi^{g}\upsilon\sigma_{f}^{hom,g'}\right]\phi^{g'}(x) \tag{4.26}$$
$$\left.-\sum_{l'=0}^{L}\frac{2l'+1}{2}P_{l'}(\mu)\left[\sigma^{g}(x)-\sigma^{hom,g}\right]\phi_{l'}^{g}(x)\right\}\frac{1}{\phi_{avg}^{g}}$$

If $h_n(x)$ is an orthonormal basis function over a finite interval *i.e.*, $x\epsilon[0,a]$ with $w(x)=1$, the auxiliary cross-section can be simplified to:

$$\sigma_{aux}^{g}(x,\mu)=\sum_{l=0}^{L}\frac{2l+1}{2}P_{l}(\mu)\sum_{n=0}^{N}h_{n}(x)\left[\delta_{0,l}\alpha_{n}^{g}+\delta_{0,l}\beta_{n}^{g}-\gamma_{n,l}^{g}\right] \tag{4.27}$$

where

$$\alpha_n^g = \frac{\sum_{g'} \int_0^a h_n(x)\,[\Delta\sigma_{s0}^{g'\to g}(x)]\phi^{g'}(x)dx}{\int_o^a \phi^g(x)\,dx/a} \tag{4.28}$$

$$\beta_n^g = \frac{\frac{1}{k}\sum_{g'} \int_0^a h_n(x)\left[\chi^g \Delta\upsilon\sigma_f^{g'}(x)\right]\phi^{g'}(x)dx}{\int_o^a \phi^g(x)\,dx/a} \tag{4.29}$$

$$\gamma_{n,l}^g = \frac{\int_0^a h_n(x)\,[\Delta\sigma^g(x)]\phi_l^g(x)dx}{\int_o^a \phi^g(x)\,dx/a} \tag{4.30}$$

$$\Delta\sigma_{t,s,f}^g(x) = \sigma_{t,s,f}^g(x) - \sigma_{t,s,f}^{hom,g} \tag{4.31}$$

If the expansion has an infinite order, no truncation error is introduced into the auxiliary cross-section. However this is not practical and all expansions must have a cut off order. The truncation error can be minimized by the choice of basis function. For a square-integrable function, the Fourier series forms an orthonormal basis with respect to *l*2-norm and has the least root mean squared (RMS) error. Hence the Generalized Fourier series is used as the expansion function and $h_n(x) = \exp(j2\pi nx/a)$ where j refers to the imaginary number.

Expanding a non-periodic function with periodic basis function such as Fourier series requires further attention. Due to the discontinuity of the non-periodic function at the boundaries, spurious oscillations known as Gibbs phenomenon are inevitable. To this extent it is desirable to use either a modified Fourier spectral or a Fourier-Gegenbauer (F-G) method to expand the non-periodic function. The author has chosen the former technique which includes modifying the non-periodic function into a periodic function

and expanding the modified version in a periodic expansion basis. By applying Fourier series Eqs. (4.27) – (4.30) are reduced to:

$$\sigma_{aux}^{g}(x,\mu) = \sum_{l=0}^{L} \frac{2l+1}{2} P_l(\mu) \sum_{n=-M}^{M} \exp(j\frac{2\pi}{a}nx) \left[\delta_{0,l}\alpha_n^g + \delta_{0,l}\beta_n^g - \gamma_{n,l}^g\right] \tag{4.32}$$

where

$$\alpha_n^g = \frac{\sum_{g'} \int_0^a \exp(-j\frac{2\pi}{a}nx) \left[\Delta\sigma_{s0}^{g'\to g}(x)\right]\phi^{g'}(x)dx}{\int_o^a \phi^g(x)\,dx} \tag{4.33}$$

$$\beta_n^g = \frac{\frac{1}{k}\sum_{g'} \int_0^a \exp(-j\frac{2\pi}{a}nx) \left[\chi^g \Delta\upsilon\sigma_f^{g'}(x)\right]\phi^{g'}(x)dx}{\int_o^a \phi^g(x)\,dx} \tag{4.34}$$

$$\gamma_{n,l}^g = \frac{\int_0^a \exp(-j\frac{2\pi}{a}nx) \left[\Delta\sigma^g(x)\right]\phi_l^g(x)dx}{\int_o^a \phi^g(x)\,dx} \tag{4.35}$$

4.4 Numerical Results

The premise of the CSH method is to reproduce the heterogeneous solution from the homogenized transport equation by including an auxiliary cross-section that contains the deviation from the average (homogenized) cross sections. However, the dependence of the auxiliary source term on the flux shape within each assembly (homogenized region) necessitates iteration between the core and assembly solvers.

The auxiliary cross-section in 1D is expanded by using Legendre polynomial in angle and Generalized Fourier series in space. In the S_N approximation, the order of Legendre polynomials is limited to $(N-1)$ and in Generalized Fourier series the highest order due to Nyquist Theorem is limited to $M < \frac{a}{2(\Delta x)_{max}}$ where a is the length of the homogenized region and $(\Delta x)_{max}$ is the maximum spatial mesh size in the homogenized region.

In section 4.4.1 two 1D BWR assemblies will be compared against the heterogeneous solution with different expansion orders of the auxiliary cross-section. In section 4.4.2 with the choice of expansion orders obtained from the assembly result, the accuracy of a 1D BWR core and a 1D HTTR core (described in Chapter 2) will be presented using the CSH method. Section 4.4.3 demonstrates the computation time normalized to the reference solution for the benchmark problems. For the example problems, with the correct choice of spatial discretization, the critical value of $\sigma\Delta x/(2\mu_{min})$ was kept constant throughout the heterogeneous (reference) and homogeneous problems. This choice would keep the effect of numerical error for both heterogeneous and homogeneous problems consistent.

4.4.1 1D Single Assembly Test Problem

Two bundle types from a recently published 1D BWR benchmark (Douglass and Rahnema, 2011) are selected to test the new method. Each bundle is composed of 10 material regions (8 fuel-pin regions + moderator region on both sides). The fuel regions are each 1.6256 cm in width, and the outside moderator regions are 1.1176 cm in width,

leading to 15.24 cm total bundle width (typical of BWR bundles). The two bundle types are laid out in Figure 4.1. Bundle 1 is composed of low-enriched fuel pins (‘‘L’’), high-enriched fuel pins (‘‘H’’), and moderator (‘‘M’’). Bundle 2 is composed of both low-enriched fuel pins and gadded fuel pins (‘‘G’’). A 47-group cross-section library was generated with the lattice depletion transport code HELIOS (Simeonov, 2003) using a GE9 pin-cell model (Kelly, 1995), homogenized over the pin cells as described in Douglass and Rahnema (2011).

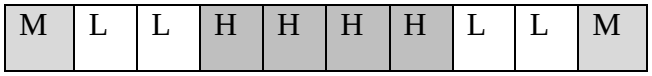

(a) Bundle 1

(b) Bundle 2

Figure 4.1. Bundle layout for bundles 1 and 2

Both bundles were modeled with vacuum boundary condition on both sides and the 47-group heterogeneous (reference) solution was calculated with S_{16} approximation using diamond differencing scheme. Although the vacuum boundary condition is not representative of the core environment, it was purposely used since the resulting sharp gradients and high anisotropy in the neutron flux challenges any method in general. This in particular would be a good test of the robustness of any expansion method. The reference eigenvalue and flux profile were used to homogenize cross sections over the assembly and to generate the auxiliary cross-section. In order to determine the error

between the solutions, the spatial discretization of both the homogeneous and heterogeneous problems should be the same. Two techniques can be used: discretize the homogeneous problem exactly the same as the heterogeneous problem; or discretize the homogeneous problem based on the homogenized cross-section and carryout fixed-source calculations based on the calculated eigenvalue and boundary conditions. Due to Gibbs phenomena in the auxiliary cross-section, the former technique is expected to have larger errors in the flux while the Gibbs phenomena are averaged out in the latter. Therefore, the effect of expansion order is more pronounced using the first technique and it is chosen to demonstrate the effect of expansion orders. However, in a realistic problem, assemblies are discretized based on the homogenized cross sections and the magnitude of the error is decreased.

For the remainder of this chapter, the average, mean and maximum relative error (difference) between the heterogeneous (reference) and homogeneous solutions are defined as:

$$AVG_g = \frac{\int dx|e^g(x)|}{\int dx} \tag{4.36}$$

$$MRE_g = \frac{\int dx|e^g(x)|\phi_{hom}^g(x)}{\int dx\phi_{ref}^g(x)} \tag{4.37}$$

$$MAX_g = \max(|e^g(x)|) \tag{4.38}$$

where

$$e^g(x) = 100\% \frac{\phi_{ref}^g(x) - \phi_{hom}^g(x)}{\phi_{ref}^g(x)} \tag{4.39}$$

In order to gain a feasible understanding of the difference between the homogeneous and heterogeneous flux distribution, the value of error is demonstrated for 2-group flux condensed from a 47-group flux spectrum.

In Tables 4.1- 4.3 the effect of spatial expansion order on the new method's error is demonstrated while the angular expansion order was kept at *L=15*. Note that the case *M=0, L=0* represents the homogeneous solution without the auxiliary cross-section. As expected, it is seen that the transport solution of the homogeneous problem without the use of auxiliary cross-section introduces large errors in the scalar flux and eigenvalue. As seen from Tables 4.1- 4.3, increasing the angular expansion order has negligible effect on the results when *M=0*, e.g., compare *M=0, L=0* and *M=0, L=15* results. That is, the space-angle effect resulting from the total cross-section term embedded in the auxiliary cross-section is insignificant when the spatial moments are neglected. Increasing the spatial expansion order will result in more accurate homogeneous solution. However, the magnitude of error decreases slowly after *M=20* which implies that the error is mainly due to Gibbs phenomena within the homogenized region and it is well known that this error decreases linearly with the expansion order.

Table 4.1. Flux error in bundle 1, *L=15*

	AVG(%)		MAX(%)		MRE(%)	
M	Fast	Thermal	Fast	Thermal	Fast	Thermal
0	3.42	18.61	8.25	42.24	3.52	15.81
5	0.41	2.20	1.39	9.99	0.35	1.67
10	0.14	0.89	0.55	4.81	0.10	0.69
15	0.09	0.47	0.37	2.77	0.06	0.37
20	0.06	0.29	0.27	1.90	0.04	0.23
25	0.04	0.20	0.20	1.39	0.03	0.16
30	0.03	0.15	0.16	1.06	0.02	0.12
35	0.02	0.12	0.13	0.84	0.02	0.10
40	0.02	0.09	0.12	0.68	0.01	0.07
45	0.02	0.08	0.09	0.57	0.01	0.06
M=0,L=0	3.42	18.60	8.26	42.21	3.52	15.80

Table 4.2. Flux error in bundle 2, *L=15*

	AVG(%)		MAX(%)		MRE(%)	
M	Fast	Thermal	Fast	Thermal	Fast	Thermal
0	9.39	76.84	18.70	160.18	7.31	91.93
5	1.05	6.76	2.67	20.44	1.02	6.06
10	0.39	2.57	1.02	9.07	0.37	2.33
15	0.21	1.34	0.58	5.35	0.19	1.22
20	0.13	0.84	0.37	3.74	0.12	0.76
25	0.09	0.58	0.26	2.77	0.08	0.53
30	0.06	0.43	0.19	2.29	0.06	0.39

Table 4.2 (continued)

	AVG(%)		MAX(%)		MRE(%)	
M	Fast	Thermal	Fast	Thermal	Fast	Thermal
35	0.05	0.33	0.16	1.94	0.04	0.30
40	0.04	0.27	0.13	1.66	0.04	0.25
45	0.03	0.22	0.11	1.45	0.03	0.21
M=0,L=0	9.38	76.87	18.69	160.19	7.31	91.94

Table 4.3. Eigenvalue error in bundles 1 and 2

k_{ref}	Bundle 1		Bundle 2	
	0.614213		0.265508	
	k_{hom}	$\Delta k^a\ (pcm)$	k_{hom}	$\Delta k\ (pcm)$
M=0,L=15	0.611434	277.9	0.288672	-2316.4
M=5,L=15	0.614898	-68.5	0.265578	-7.0
M=10,L=15	0.614281	-6.8	0.265514	-0.6
M=15,L=15	0.614228	-1.5	0.265509	-0.1
M=20,L=15	0.614216	-0.3	0.265507	0.1
M=25,L=15	0.614212	0.1	0.265508	0.0
M=30,L=15	0.614212	0.1	0.265508	0.0
M=35,L=15	0.614212	0.1	0.265508	0.0
M=40,L=15	0.614212	0.1	0.265508	0.0
M=45,L=15	0.614212	0.1	0.265508	0.0
M=0,L=0	0.611587	262.6	0.288715	-2320.7

[a] $\Delta k = (k_{ref} - k_{hom}) \times 10^5$

In Tables 4.4- 4.6, the effect of angular expansion order of the auxiliary cross-section are presented for the case when the spatial expansion order is kept constant at *M=35*. For both bundles, it is noticeable that including only the first term of the angular expansion decreases the error to 10 pcm. Also from Tables 4.4 and 4.5, it can be observed that increasing the angular expansion order beyond *L=1* does not improve the error indicating the accuracy is limited by the spatial expansion order kept constant at *M=35*. This is clearly seen when *L=15* which is the order at which the entire angular effect is captured. Further, it seems that a P_1 approximation captures the majority of the angular effect of the auxiliary cross-section.

Table 4.4. Flux error in bundle 1, *M=35*

L	AVG(%)		MAX(%)		MRE(%)	
	Fast	Thermal	Fast	Thermal	Fast	Thermal
0	2.27	3.50	3.69	10.37	2.72	3.02
1	0.05	0.09	0.28	0.59	0.04	0.08
2	0.05	0.16	0.16	1.04	0.05	0.12
4	0.03	0.12	0.18	0.86	0.02	0.09
6	0.02	0.12	0.17	0.84	0.02	0.09
8	0.02	0.12	0.16	0.84	0.02	0.09
10	0.02	0.12	0.15	0.84	0.02	0.09
12	0.02	0.12	0.14	0.84	0.02	0.09
14	0.02	0.12	0.13	0.84	0.02	0.09
15	0.02	0.12	0.13	0.84	0.02	0.09

Table 4.5. Flux error in bundle 2, *M=35*

L	AVG(%)		MAX(%)		MRE(%)	
	Fast	Thermal	Fast	Thermal	Fast	Thermal
0	1.64	4.61	2.86	7.83	1.82	4.12
1	0.06	0.40	0.33	1.53	0.04	0.36
2	0.05	0.41	0.25	1.85	0.05	0.37
4	0.04	0.34	0.22	1.92	0.04	0.31
6	0.05	0.34	0.19	1.93	0.04	0.31
8	0.05	0.33	0.17	1.94	0.04	0.31
10	0.05	0.33	0.15	1.94	0.04	0.31
12	0.05	0.33	0.15	1.94	0.04	0.31
14	0.05	0.33	0.15	1.94	0.04	0.30
15	0.05	0.33	0.16	1.94	0.04	0.30

Table 4.6. Eigenvalue error in bundles 1 and 2, *M=35*

k_{ref}	Bundle 1		Bundle 2	
	0.614213		0.265508	
	k_{hom}	$\Delta k\ (pcm)$	k_{hom}	$\Delta k\ (pcm)$
L=0	0.601153	1306.0	0.262515	299.3
L=1	0.614307	-9.4	0.265614	-10.6
L=2	0.614164	4.9	0.265577	-6.9
L=4	0.614211	0.2	0.265531	-2.3
L=6	0.614210	0.3	0.265516	-0.8
L=8	0.614210	0.3	0.265511	-0.3
L=10	0.614210	0.3	0.265509	-0.1

Table 4.6 (continued)

k_{ref}	Bundle 1		Bundle 2	
	0.614213		0.265508	
	k_{hom}	$\Delta k\ (pcm)$	k_{hom}	$\Delta k\ (pcm)$
L=12	0.614210	0.3	0.265508	0.0
L=14	0.614211	0.2	0.265508	0.0
L=15	0.614211	0.2	0.265508	0.0

From Table 4.6, it can be seen that the angular effect on the eigenvalue is very large in Bundle 1 as compared to Bundle 2 (*i.e.*, compare case *L=0* to *L=1*). This is expected because of the large angular anisotropy resulting from a much higher fast to thermal flux ratio in Bundle 1 as compared to Bundle 2. As seen in Table 4.3, this phenomenon is reversed in that spatial effects dominate because of the presence of gadolinium resulting in large flux gradient in Bundle 2.

From the above analysis, it is clear that the homogenized transport solution agrees very well with the heterogeneous solution using a low order (*L=1*) expansion in angle and high order (*M=35)* expansion in space.

4.4.2 1D Core Problems

In this section two 1D core problems (described in Chapter 2) are used to test the CSH method. The only difference between the process carried out for the example problems and the procedure described at the end of the method section (section 4.2) is that step (3) is skipped for the example problems because both assembly calculations and core

calculations are done using same S_N approximation and the use of surface expansion function is redundant. Therefore, the flux from the core calculation is used to update the incoming angular flux at the surface of each homogenized region for on-the-fly assembly calculations. The iteration flux error is the difference between the reference solution and the flux resulting from assembly calculations. The successive iteration criteria for the CSH method were chosen as $(\varepsilon_\phi)_{re-hom} = 10^{-3}$ and $(\varepsilon_k)_{re-hom} = 10^{-4}$. The 1D core problems (homogeneous and heterogeneous) are solved using S_8 , 47-group approximation and diamond differencing scheme with the flux and eigenvalue convergence criteria of 10^{-5} and 10^{-8} , respectively. Furthermore, a fine-mesh transport homogenization using the standard homogenization method (*i.e.*, assembly calculation with specular reflective boundary condition without the auxiliary cross-section, designated as FMTHIM) and a highly accurate nodal diffusion (ANOD) method (Rahnema and Mckinley, 2002) are added to the tables for comparison. The ANOD model uses fine-mesh inside each assembly with standard Generalized Equivalence Theory (GET) homogenized cross sections (Smith, 1986) and infinite medium discontinuity factor at the assembly interfaces. The FMTHIM model is obtained by homogenizing every assembly with the infinite medium flux and solving the core problem using fine-mesh within each assembly.

4.4.2.1 1D BWR Core Problem

In Table 4.7, the eigenvalue and flux error for FMTHIM, ANOD and CSH methods are demonstrated. It is seen that the CSH method without iteration is capable of reducing the

eigenvalue error to less than 30 pcm mainly by decreasing the thermal flux error. By increasing the iteration order, the core environment effect on the homogenized cross-section is corrected and after 3 iterations the homogeneous solution is converged to the heterogeneous one. Additionally, the ANOD method has lower thermal flux error compared to FMTHIM and it predicts the heterogeneous eigenvalue more accurately.

Table 4.7. Eigenvalue and flux error in ARO configuration for CSH method

	k_{ref}=1.066815		AVG(%)		MAX(%)		MRE(%)	
iteration	k_{hom}	$\Delta k\ (pcm)$	Fast	Th.	Fast	Th.	Fast	Th.
0^{th}	1.067086	-27.1	4.70	4.76	11.78	11.41	3.22	3.81
1^{st}	1.067011	-19.6	0.41	0.40	1.27	1.01	0.28	0.33
2^{nd}	1.066780	3.5	0.04	0.12	0.13	0.58	0.04	0.13
3^{rd}	1.066816	-0.1	0.04	0.12	0.11	0.58	0.03	0.12
$FMTHIM^{a}$	1.065385	143.0	3.47	21.62	12.38	62.66	2.79	21.78
$ANOD^{b}$	1.066426	38.9	4.09	20.88	13.27	59.97	3.63	21.36

^{a} Fine-Mesh Transport Homogenization using Infinite Medium flux
^{b} Accurate Nodal Diffusion method

Table 4.7 demonstrates the eigenvalue and flux error for SRI configuration. The FMTHIM and ANOD methods exhibit higher flux errors due to presence of control rods and the core environment effect is more pronounced. However, the CSH method is capable of correcting for core environment consistently and converges after 3 iterations. Nonetheless, the CSH method without iteration has less error in flux and eigenvalue compared to ANOD and FMTHIM methods.

Table 4.8. Eigenvalue and flux error in SRI configuration for CSH method

	k_{ref}= 1.003437		AVG(%)		MAX(%)		MRE(%)	
iteration	k_{hom}	$\Delta k\ (pcm)$	Fast	Th.	Fast	Th.	Fast	Th.
0^{th}	1.002972	46.5	4.46	4.47	10.81	11.37	3.45	4.17
1^{st}	1.003474	-3.7	0.38	0.38	1.19	0.92	0.28	0.37
2^{nd}	1.003389	4.8	0.08	0.14	0.23	0.65	0.07	0.14
3^{rd}	1.003409	2.8	0.08	0.14	0.21	0.64	0.06	0.14
$FMTHIM$	1.000689	274.8	3.21	17.00	11.71	56.35	3.05	16.86
$ANOD$	1.002047	139.0	3.94	16.77	12.98	56.21	3.49	16.80

Figures 4.3(a) and 4.5(a) demonstrate the flux error for the CSH method after the 3rd iteration. As expected, the error peaks are located at the assembly interfaces. This is due to the flux discontinuity at the boundaries resulting from the Gibbs phenomena at assembly interfaces. By using higher spatial expansion order (M=2×35) it has been verified that the maximum error seen at the boundaries, decreases to less than half of its value. It is noted that the outer iteration convergence criterion (10^{-3}) is looser than then inner iteration convergence criterion (10^{-5}). It has been verified using an inconsistent set of criteria (e.g., 10^{-3} versus 10^{-5}) does not affect the magnitude of the maximum error.

As seen from Figures 4.3(b), 4.3(c) , 4.5(b) and 4.5(c) the maximum error in scalar flux using FMTHIM and ANOD methods can be as large as 50 percent while the error in eigenvalue is small (e.g., a few hundred pcm). The low error in the eigenvalues in these cases is common due to error cancelation. In particular, the leakage is not a big contributor to the neutron balance in this problem; however, the infinite medium

(standard) homogenized cross sections result in underestimated reactions (*i.e.* absorption and fission) for the interior assemblies and overestimated reactions for the exterior assemblies. Because of the alternating signs (errors) the net error in the neutron balance is small. It is noted that local over and underestimation in the local reaction rates lead to the observed large errors in the local flux estimated by the FMTHIM and ANOD methods.

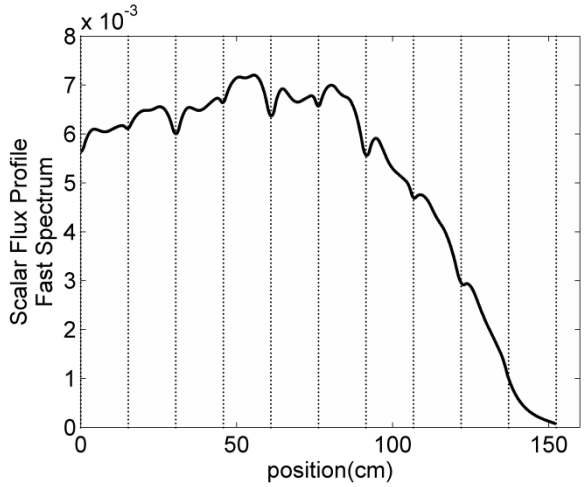

(a) Fast spectrum

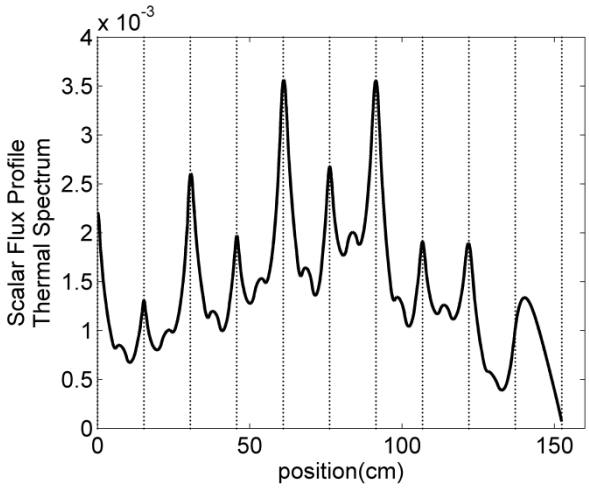

(b) Thermal spectrum

Figure 4.2. Scalar flux profile in ARO configuration of 1D BWR core. The vertical lines represent the interface of assemblies.

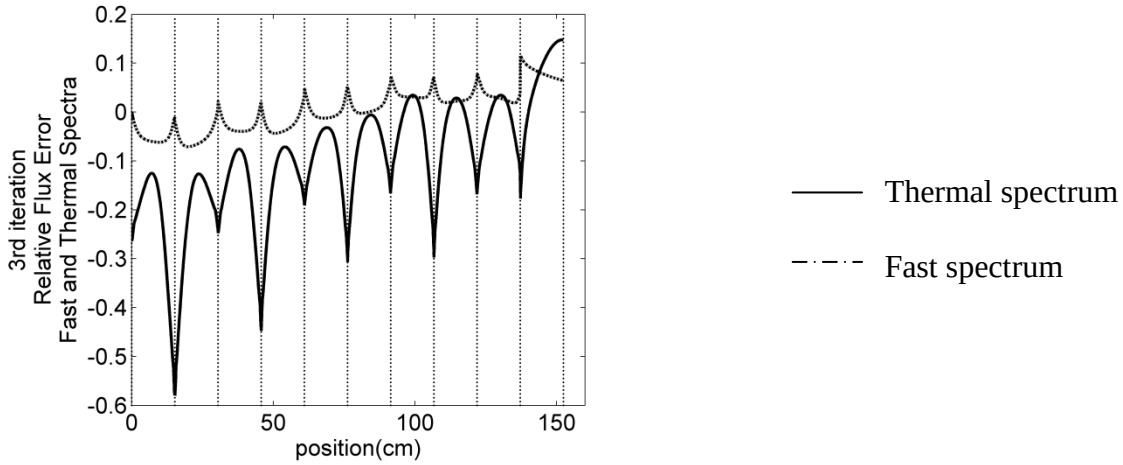

(a) Relative fast and thermal flux error after 3rd iteration in CSH method

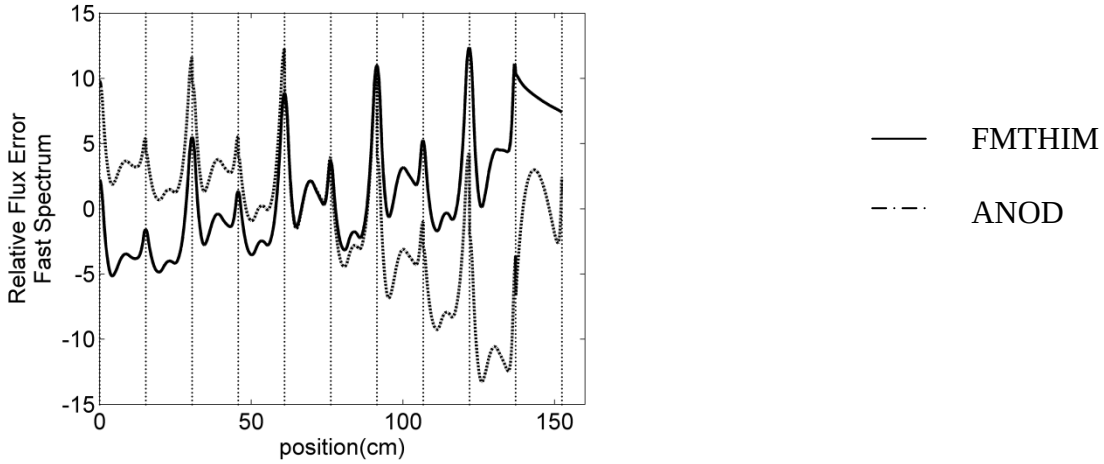

(b) Relative fast flux error in ANOD and FMTHIM methods

Figure 4.3. Relative flux error profile (in percent) in ARO configuration of 1D BWR core

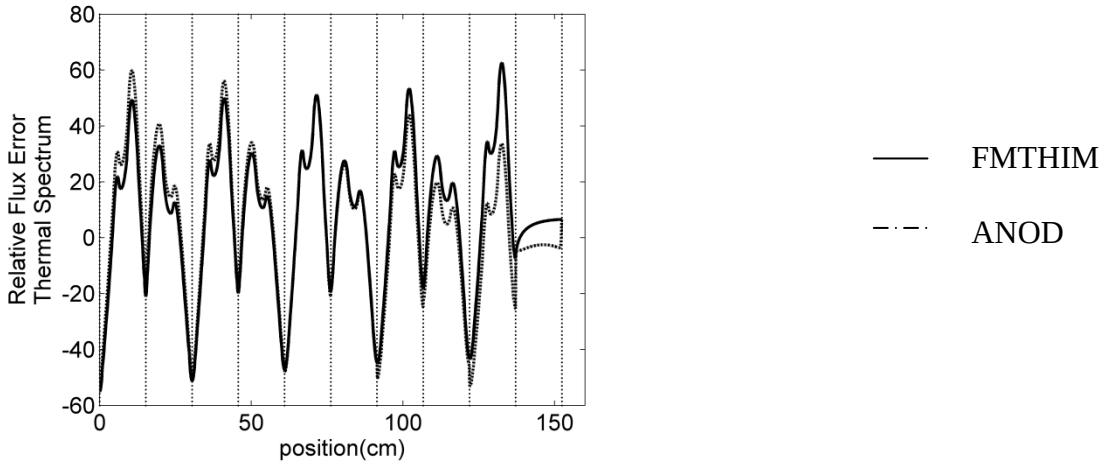

(c) Relative thermal flux error in ANOD and FMTHIM methods

Figure 4.3 continued

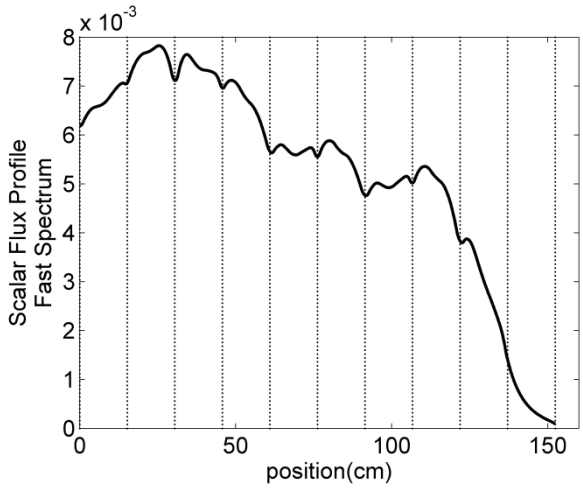

(a) Fast spectrum

Figure 4.4. Scalar flux profile in SRI configuration of 1D BWR core. The vertical lines represent the interface of assemblies.

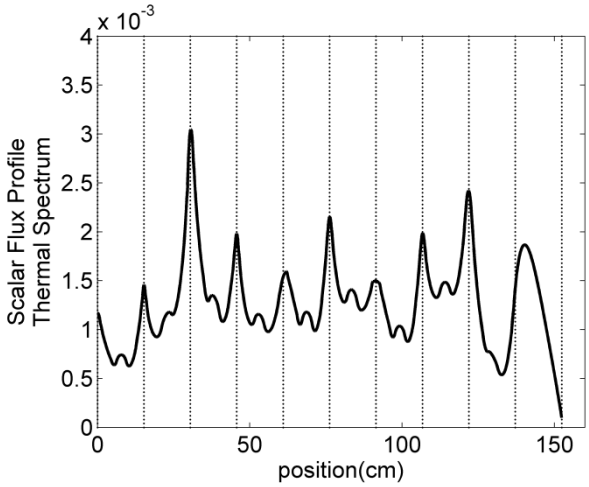

(b) Thermal spectrum

Figure 4.4 continued

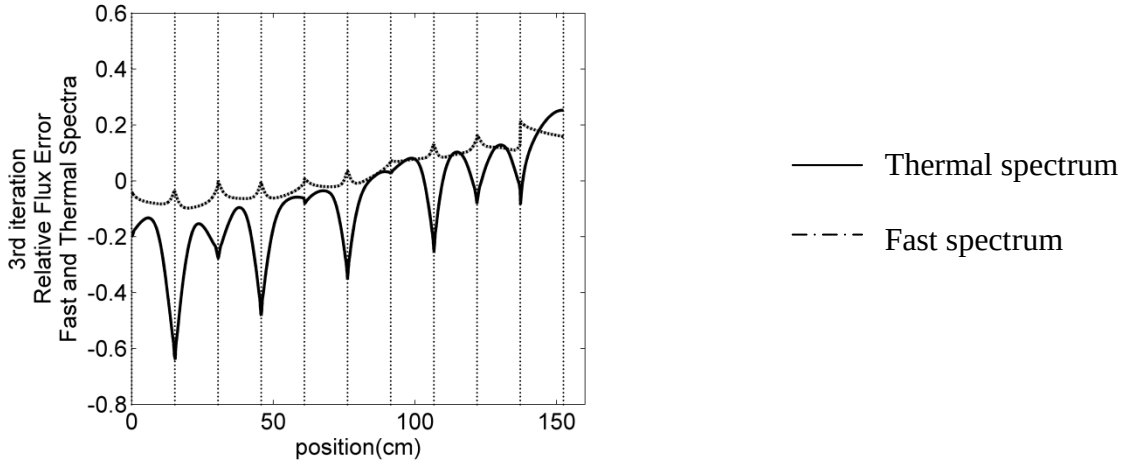

(a) Relative fast and thermal flux error after 3rd iteration in CSH method

Figure 4.5. Relative flux error profile (in percent) in SRI configuration of 1D BWR core

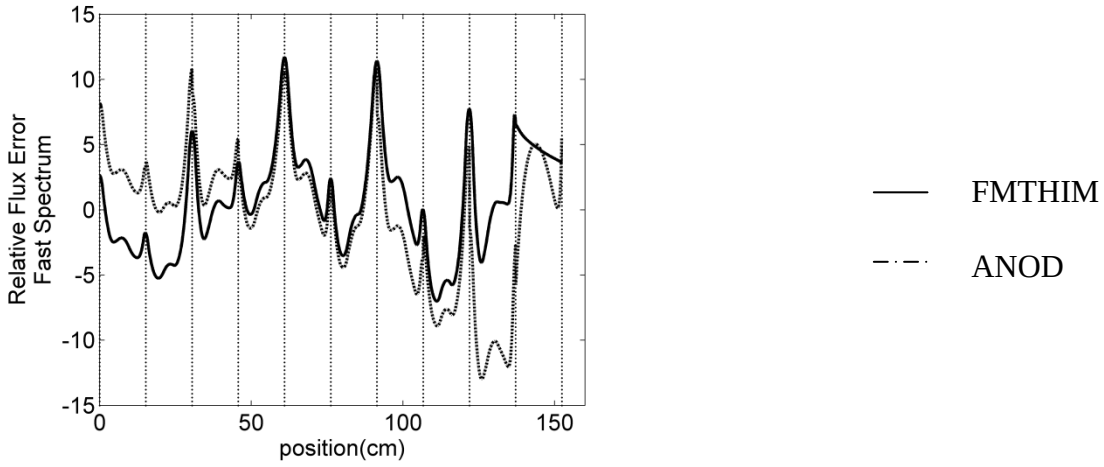

(b) Relative fast flux error in ANOD and FMTHIM methods

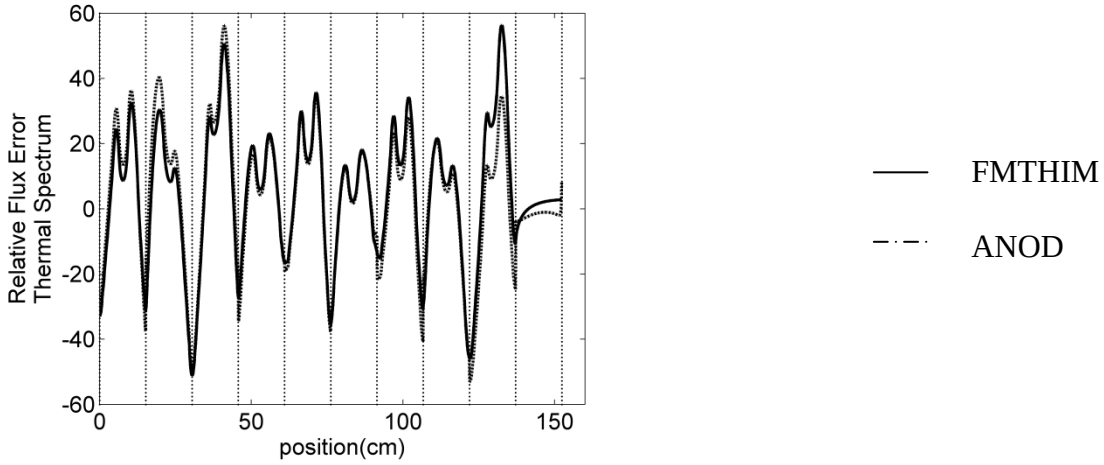

(c) Relative fast flux error in ANOD and FMTHIM methods

Figure 4.5 continued

4.4.2.2 1D HTTR Core Problem

From Tables 4.9 and 4.10 it is seen that the 0^{th} iteration flux profile and eigenvalue exhibit larger error when compared to BWR core results. This is expected since unlike the BWR core the spatial and energy spectrum in each block is driven by its neighboring blocks because of the larger neutron mean free path. This implies that core environmental effect on cross-section homogenization is even more pronounced in these cores. The effect becomes even more pronounced when the control rods are inserted as a result of harder spectrum. Additionally, as seen from Figures 4.7(b), 4.7(c), 4.9(b) and 4.9(c) the ANOD and FMTHIM methods result in similar solutions confirming the higher sensitivity of the homogeneous solution on homogenized cross sections and the necessity to correct for core environment.

Table 4.9. Eigenvalue and flux error in ARO configuration for CSH method

	k_{ref}=1.102972		AVG(%)		MAX(%)		MRE(%)	
iteration	k_{hom}	$\Delta k\ (pcm)$	Fast	Th.	Fast	Th.	Fast	Th.
0^{th}	1.141348	-3837.6	5.68	3.51	14.24	9.30	5.69	3.66
1^{st}	1.100438	253.4	0.50	0.35	1.83	0.99	0.59	0.37
2^{nd}	1.103150	-17.8	0.05	0.04	0.25	0.12	0.05	0.04
3^{rd}	1.102971	0.1	0.03	0.02	0.08	0.06	0.01	0.01
4^{th}	1.102978	-0.6	0.03	0.02	0.08	0.06	0.01	0.01
$FMTHIM$	1.141116	-3814.4	10.33	5.53	22.72	17.17	7.18	6.19
$ANOD$	1.141342	-3837.0	15.94	4.33	62.36	18.81	6.19	4.94

Table 4.10. Eigenvalue and flux error in ARI configuration for CSH method

iteration	k_{ref} = 0.829591		AVG(%)		MAX(%)		MRE(%)	
	k_{hom}	$\Delta k\ (pcm)$	Fast	Th.	Fast	Th.	Fast	Th.
0^{th}	0.895213	-6562.2	31.92	33.04	48.25	61.81	12.87	17.13
1^{st}	0.822762	682.9	5.60	5.68	10.74	10.08	1.55	1.59
2^{nd}	0.830297	-70.6	0.36	0.27	0.58	0.93	0.13	0.10
3^{rd}	0.829510	8.1	0.03	0.14	0.08	0.48	0.03	0.04
4^{th}	0.829613	-2.2	0.05	0.17	0.10	0.46	0.03	0.04
5^{th}	0.829601	-1.0	0.05	0.17	0.09	0.46	0.03	0.04
$FMTHIM$	0.889602	-6001.1	29.13	36.98	44.76	84.42	13.28	18.49
$ANOD$	0.889329	-5973.8	38.88	39.01	78.77	85.14	12.20	15.59

Figures 4.6 and 4.8 demonstrate the fast and thermal flux profile of the reference case in ARO and SRI configurations. In Figures 4.7(a) and 4.9(a) the relative flux error using the CSH method in ARO and ARI configurations are shown, respectively. It is noted that the magnitude of thermal flux error in the CSH method is smaller in the ARO configuration as compared to that in the ARI configuration because of the sharp gradients introduced by the control rods. In order to achieve higher accuracy if necessary, higher spatial expansion order for the auxiliary cross-section and tighter flux convergence criteria in the homogeneous solution should be used.

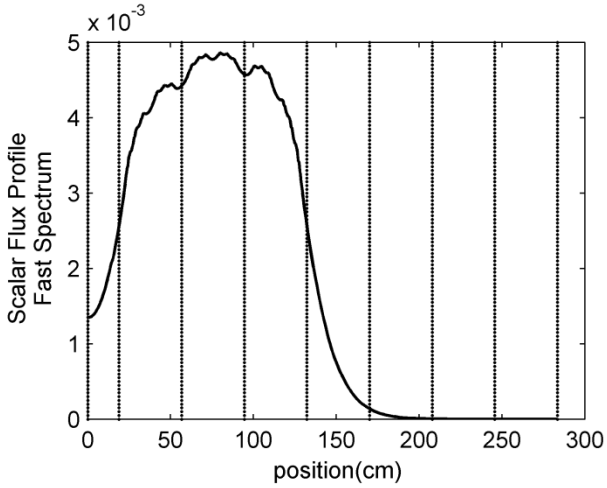

(a) Fast spectrum

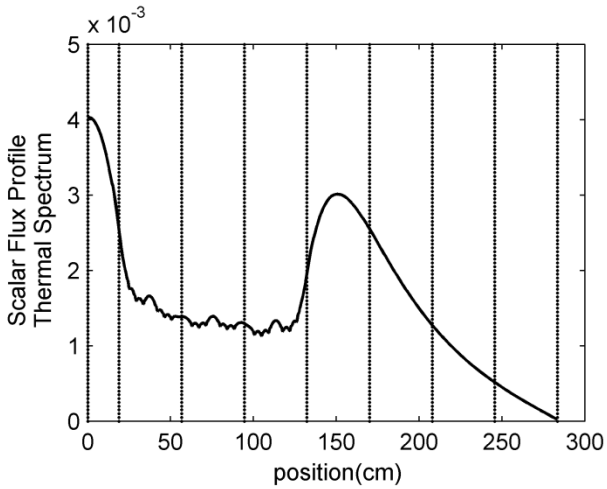

(b) Thermal spectrum

Figure 4.6. Scalar flux profile in ARO configuration of 1D HTTR core. The vertical lines represent the interface of assemblies

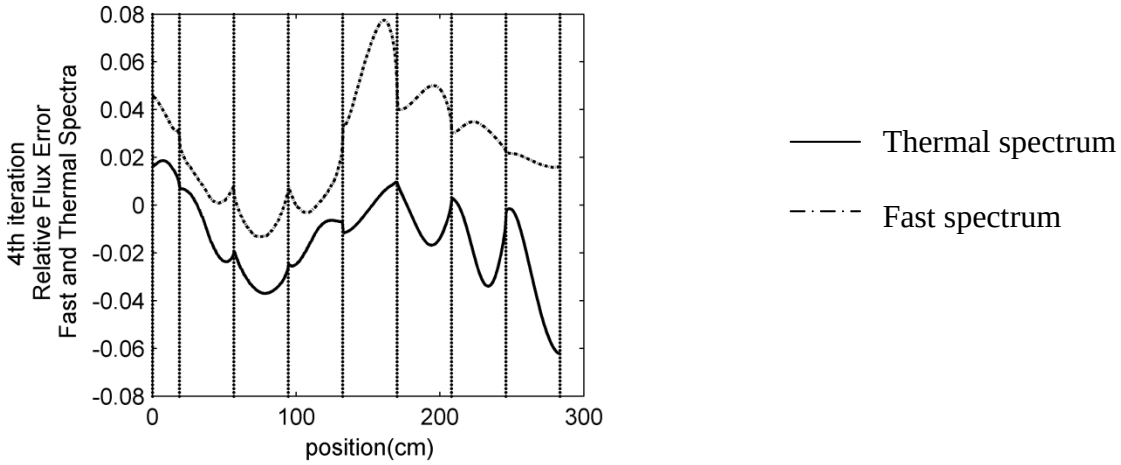

(a) Relative fast and thermal flux error after 4th iteration in CSH method

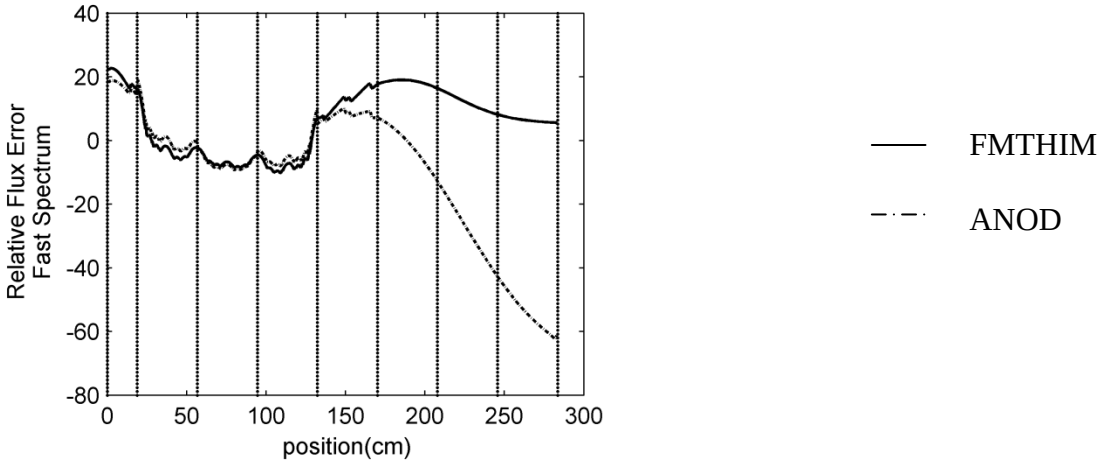

(b) Relative fast flux error in ANOD and FMTHIM methods

Figure 4.7. Relative flux error profile (in percent) in ARO configuration of 1D HTTR core

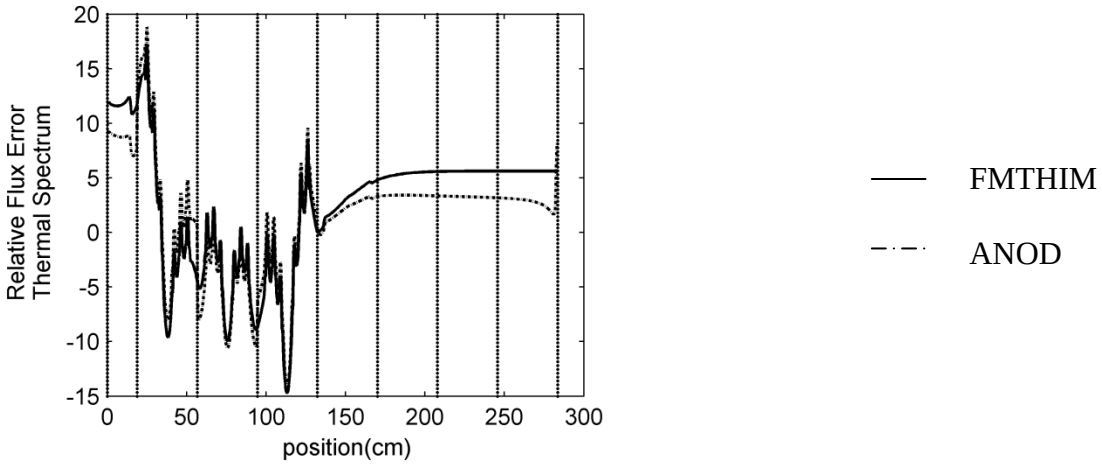

(c) Relative thermal flux error in ANOD and FMTHIM methods

Figure 4.7 continued

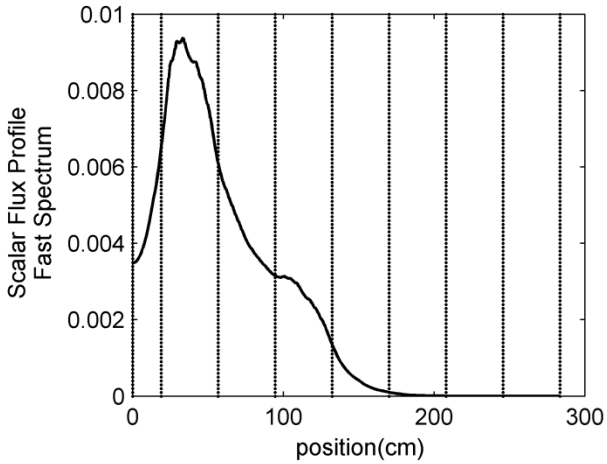

(a) Fast spectrum

Figure 4.8. Scalar flux profile in ARI configuration of 1D HTTR core. The vertical lines represent the interface of assemblies

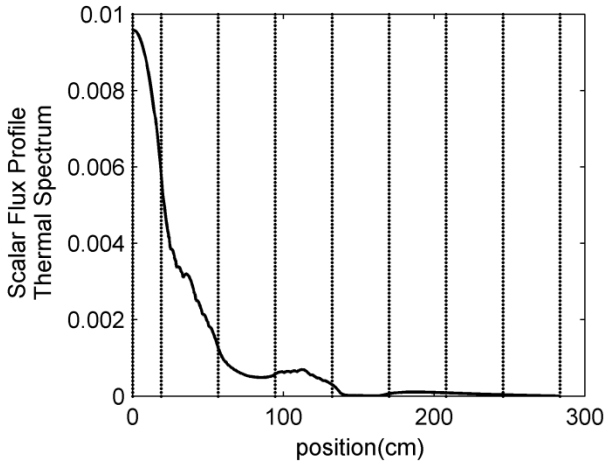

(b) Thermal spectrum

Figure 4.8 continued

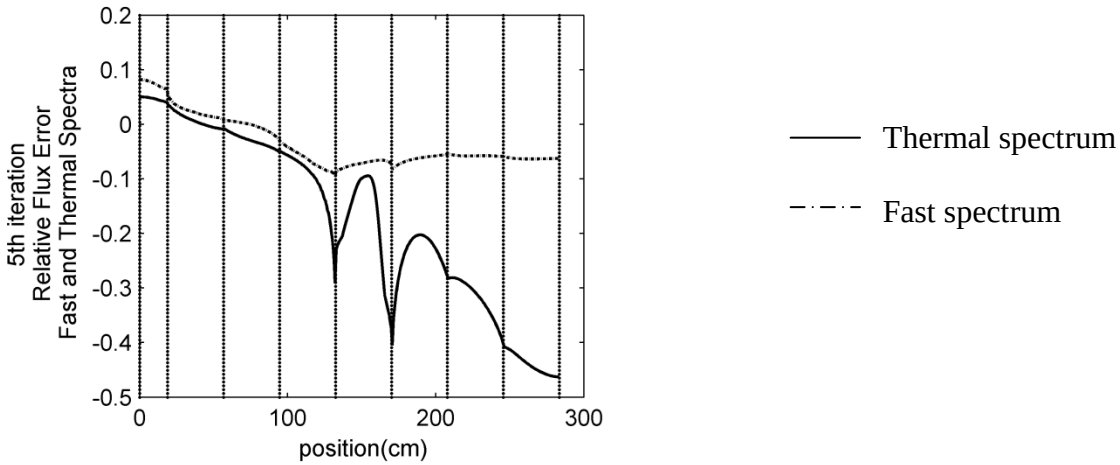

(a) Relative fast and thermal flux error after 5^{th} iteration in CSH method

Figure 4.9. Relative flux error profile (in percent) in ARI configuration of 1D HTTR core

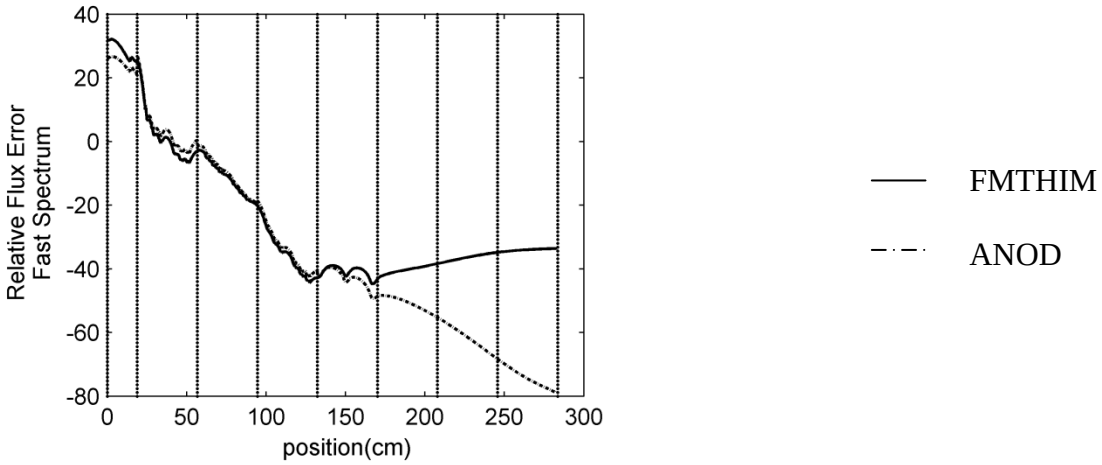

(b) Relative fast flux error in ANOD and FMTHIM methods

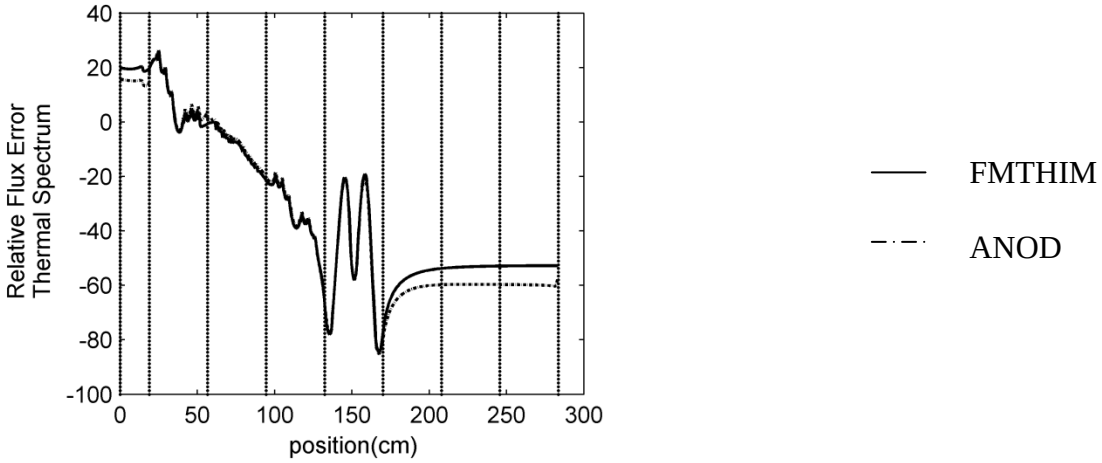

(c) Relative thermal flux error in ANOD and FMTHIM methods

Figure 4.9 continued

4.4.3 Computational Efficiency Analysis

This section briefly discusses the computational efficiency of the new CSH method. In this method, the heterogeneous transport equation (4.40) is homogenized by embedding the material heterogeneities in an auxiliary cross-section that is representative of variation of the cross sections from the average (homogenized value) as seen in Eq. (4.41).

$$H\psi = S\psi + \frac{1}{k}F\psi \tag{4.40}$$

$$H^{hom}\psi = S^{hom}\psi + \frac{1}{k^{hom}}F^{hom}\psi + A^{hom}\psi \tag{4.41}$$

Since the last term in Eq. (4.41) depends on the solution itself, it is computationally beneficial to relax the convergence criteria initially and tighten as the iteration progresses. In the progressive convergence scheme, in the HTTR core, the convergence criteria are initially set to $\varepsilon_k = 10^{-5}$ and $\varepsilon_\phi = 10^{-2}$ and then decreased an order after each iteration, up to the 3rd iteration. Given that the neutron MFP in the BWR problem is smaller than in the HTTR problem, the initial convergence criteria were set to $\varepsilon_k = 10^{-6}$ and $\varepsilon_\phi = 10^{-3}$. Note that no attempt was made to optimize the progressive convergence scheme in this chapter but an extension to adaptive convergence scheme would be an interesting future work.

Tables 4.11 and 4.12 demonstrate computation times in two configurations of BWR and HTTR cores. In each configuration, two cases are reported: One is associated with the progressive convergence scheme and the other corresponds to a fixed convergence scheme. In the latter, the eigenvalue and flux convergence criteria in each iteration are set to $\varepsilon_k = 10^{-8}$ and $\varepsilon_\phi = 10^{-5}$. Computation times are normalized to computation time of the reference problem.

Table 4.11. Computation time comparison of homogeneous and heterogeneous 1D BWR

				AVG(%)		MAX(%)		MRE(%)	
		NCT^a	$\Delta k\ (pcm)$	Fast	Th.	Fast	Th.	Fast	Th.
ARO	FCS^b	0.721	-0.1	0.04	0.12	0.11	0.58	0.03	0.12
	PCS^c	0.603	-0.5	0.04	0.12	0.10	0.62	0.04	0.12
SRI	FCS	0.596	2.8	0.08	0.14	0.21	0.64	0.06	0.14
	PCS	0.539	3.0	0.06	0.13	0.21	0.63	0.05	0.13

[a] Normalized Computation Time
[b] Fixed Convergence Scheme
[c] Progressive Convergence Scheme

Table 4.12. Computation time comparison of homogeneous and heterogeneous 1D HTTR

				AVG(%)		MAX(%)		MRE(%)	
		NCT	$\Delta k\ (pcm)$	Fast	Th.	Fast	Th.	Fast	Th.
ARO	FCS	0.817	-0.6	0.03	0.02	0.08	0.06	0.01	0.01
	PCS	0.677	-1.5	0.02	0.02	0.06	0.05	0.01	0.02
SRI	FCS	1.654	-1.0	0.05	0.17	0.09	0.46	0.03	0.04
	PCS	0.846	-0.3	0.05	0.16	0.09	0.38	0.03	0.04

4.5 Concluding Remarks and Future work

In this chapter, a new consistent spatial homogenization method in transport theory has been developed that utilizes the conventional flux weighted cross sections and reproduces the heterogeneous transport solution with 1.8 to 1.2 times faster computational speed. By introducing an auxiliary source term that corrects the homogenized cross sections for deviation from the heterogeneous counterparts, the resulting solution is consistent with the heterogeneous solution both in phase space resolution and accuracy. The new consistent spatial homogenization method automatically corrects for the core environment effect with on-the-fly local re-homogenization.

The method's accuracy was verified for stylized BWR and GCR benchmark problems in1D slab configurations. The effect of spatial and angular expansion orders was investigated and it was shown that the effect of angular expansion order without adequate spatial expansion order is negligible especially for cases with control rods and high absorbing material. Further, it was shown that the number of iterations required for solution convergence is higher for optically thin reactors (GCR) than thick systems (BWR).

The fine-mesh fine-group heterogeneous fixed-source transport calculations can be expensive in 3D geometries. The need for angular details for the fixed-source problem can be relaxed by incorporating high-order diffusion theory derived in Chapter 3. Additionally, the whole-core problem can be solved in coarse groups and the subgroup

decomposition method can be utilized to unfold the fine-group flux spectrum for acceleration of the homogenized problem. This would require coupling of the hybrid subgroup decomposition method with the consistent spatial homogenization to increase the computational efficiency especially for 3D geometries.

In this chapter, only the homogenization of cross sections was considered. It would be interesting and necessary, as future work, to extend the method to include simultaneous collapsing of the energy and space for efficient and practical core calculation. This can be achieved by coupling the consistent spatial homogenization method with the hybrid subgroup decomposition method (Chapter 3), to accelerate the eigenvalue transport problem while homogenizing the heterogeneous problem without loss in accuracy.

4.6 References

Aragones, J. M., Ahnert, C., 1986. A linear discontinuous finite difference formulation for synthetic coarse-mesh few-group diffusion calculations. Nuclear Science and Engineering 94, 309-322.

Douglass, S., Rahnema, F., 2010a. Development of a 1-D boiling water reactor benchmark specification. Transactions of the American Nuclear Society, San Diego, CA, June 13-17, Vol. 102, 543–545.

Douglass, S., Rahnema, F., 2010b. Specification for a 1-dimensional gas-cooled reactor benchmark problem for neutron transport. Transactions of the American Nuclear Society, Hollywood, FL, May 9–14, Vol. 102, 74-78.

Douglass, S., Rahnema, F., 2011. Cross section recondensation method via generalized energy condensation theory. Annals of Nuclear Energy 38, 2105-2110.

Joo, H. G., Cho, J. Y., Kim, H. Y., Zee, S. Q., Chang, M. H., 2002. Dynamic implementation of the equivalence theory in the heterogeneous whole core transport calculation. Proceedings of ANS Top. Mtg, Int. Conference on the New Frontiers of Nuclear Technology, Reactor Physics, Safety and High-Performance Computing, PHYSOR, Seoul, Korea, October 10-17.

Kelly, D. J., 1995. Depletion of a BWR lattice using the RACER continuous energy Monte Carlo code. In: Proceedings of Int. Conference on Mathematics and Computations, Reactor Physics and Environmental Analyses, Portland, Oregon, April 30–May 4, Vol. 2, 1011.

Mckinley, M. S., Rahnema, F., 2000. High-order boundary condition perturbation theory for the diffusion approximation. Nuclear Science and Engineering 136, 15-33.

Mckinley, M. S., Rahnema, F., 2002. High-order boundary condition perturbation theory for the neutron transport equation. Nuclear Science and Engineering 140, 285-294.

Mondot, P., Sanchez, R., 2003. An iterative homogenization technique that preserves assembly core exchanges. Proceedings of Int. Conference on Supercomputing in Nuclear Applications, SNA, Paris, France, September 22-24.

Nichita, L., Rahnema, F., 2003. A heterogeneous finite element method in diffusion theory. Annals of Nuclear Energy 30 (3), 317-347.

Rahnema, F., 1989. Boundary condition perturbation theory for use in spatial homogenization methods. Nuclear Science and Engineering 102, 183-190.

Rahnema, F., Mckinley, M. S., 2002. High-order cross-section homogenization method. Annals of Nuclear Energy 29, 875-899.

Roberts, D. R., Ouisloumen, M., Kucukboyaci, V. N., Ivanov, K. N., 2010. Development of iterative transport-diffusion methodology for LWR analysis. Advances in Reactor Physics to Power Nuclear Renaissance, PHYSOR, Pittsburgh, Pennsylvania, May 9-14.

Sanchez, R., 2009. Assembly homogenization techniques for core calculations. Progress in Nuclear Energy 51, 14-31.

Simeonov, T., 2003. Release Notes – Helios System Version 1.8. Studsvik Scandpower Report, SSP-03/221, November 26.

Smith, K. S., 1994. Practical and efficient iterative method for LWR fuel assembly homogenization. Transactions of American Nuclear Society 71, 238-241.

Smith, K. S., 1986. Assembly homogenization technique for light water reactor analysis. Progress in Nuclear Energy 17, 303-335.

Zhang, H., Uddin, R., Dorning, J. J., 1997. A multiple-scales systematic theory for the simultaneous homogenization of lattice cells and fuel assemblies. Transport Theory and Statistical Physics 26 (7), 765-811.

Yasseri, S., Rahnema, F., 2013. Consistent Spatial Homogenization in Transport Theory. Nuclear Science and Engineering, Submitted (February).

APPENDIX A

A 1D S_N code was developed to demonstrate the numerical results for Chapters 2, 3 and 4. The S_N code has been benchmarked against MCNP. Two benchmark problems shown in Figure A.1 are included for comparison. The first configuration is an eigenvalue calculation for a 1D HTTR assembly with specular reflective boundary conditions. The second configuration is also an eigenvalue problem comprised of a 1D HTTR assembly and a graphite block with specular boundary condition on the left side and vacuum boundary condition on the right side. The same 47-group cross-section library that was discussed in Chapter 2 is used for benchmarking.

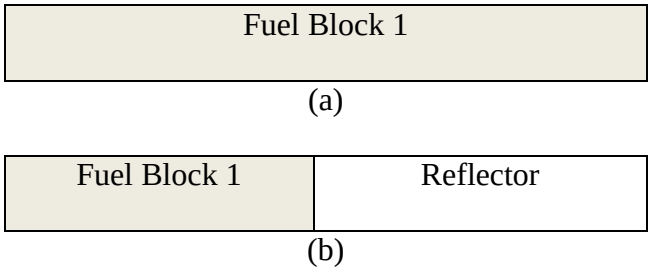

Figure A.1. (a) 1D HTTR assembly with specular boundary conditions on both sides, (b) 1D HTTR assembly with a graphite block, specular and vacuum boundary conditions on the left and right side, respectively.

The S_N results are calculated using S_{16} approximation with diamond differencing scheme and the discretization was chosen to be half mean free path (thermal energy) for all materials. The MCNP solution is obtained using 100,000 particle histories per cycle and 3000 active cycles after the initial 300 cycles were skipped.

The average, maximum, mean and root mean square relative errors for pin fission densities are presented in Table A.1 and eigenvalues are show in Table A.2. The uncertainties in pin fission density for the MCNP run are 0.01%.

Table A.1. Pin Fission Density (PFD) relative error of MCNP and SN

		AVG(%)	MAX(%)	MRE(%)	RMS(%)
PFD	FB1	0.01	0.01	0.00	0.01
	FB1+graphite	0.01	0.03	0.00	0.02

Table A.2. Eigenvalue results for MCNP and SN

	$k_{MCNP}(\pm\sigma)$	k_{SN}
FB1	1.18165(±0.00004)	1.18143
FB1+graphite	0.99954(±0.00004)	0.99934